Ultrafast multi-terahertz nano-spectroscopy with sub-cycle temporal resolution

Dissertation

zur Erlangung des Doktorgrades der Naturwissenschaften

(Dr. rer. nat.)

der Fakultät für Physik der Universität Regensburg

vorgelegt von

Max Eisele

aus Schwäbisch Hall

im Jahr 2015

Das Promotionsgesuch wurde eingereicht am 17.12.2014
Die Arbeit wurde angeleitet von: Prof. Dr. Rupert Huber

Prüfungsausschuss:	Vorsitzender:	Prof. Dr. Vladimir M. Braun
	1. Gutachter:	Prof. Dr. Rupert Huber
	2. Gutachter:	Prof. Dr. Jascha Repp
	weiterer Prüfer:	Prof. Dr. Christoph Strunk

Contents

Chapter 1

Introduction

When we go to the very, very small world - say circuits of seven atoms - we have a lot of new things that would happen that represent completely new opportunities for design. Atoms on a small scale behave like nothing on a large scale, for they satisfy the laws of quantum mechanics.

Richard P. Feynman,
There's plenty of room at the bottom, 1959

Our visual perception of the world surrounding us is determined by the interaction of light and matter. The precise interplay of electromagnetic fields with the ions and electrons in solids forms the fabric for an incredibly diverse array of optical phenomena, ranging from the metallic luster of gold to the birefringence of anisotropic crystals. Just like pushing a ball attached to a spring, the electrons in a solid are driven by external electromagnetic fields and oscillate around their equilibrium positions with oscillation characteristics given by the crystal structure, the atoms and the neighboring electrons. Hence, by using optical spectroscopy a straightforward and profound understanding of the underlying physical driving forces between electrons and ions can be established, which determine the optical properties of solids that we experience in day-to-day life. The application of conventional spectroscopy, which works well on macroscopic length scales, unfortunately, becomes increasingly challenging when the physical dimensions of solids are reduced to the nanometer scale ($1\,\mathrm{nm} = 10^{-9}\,\mathrm{m}$). Here, novel quantum effects start to dominate, significantly influencing the physical properties of condensed matter systems. Optical microscopy, which could have potentially been used to investigate these peculiar characteristics on the single nanoparticle scale, however, is hindered in its spatial resolution by the fundamental diffraction limit of light [Abb73]. The desire to visualize, to understand and to take advantage of the size-dependent properties of such nano-materials has sparked ingenious ideas and inventions helping to grasp what is hidden from the bare eye.

In 1928, Edward H. Synge started to challenge the ubiquitous diffraction limit by suggesting an experiment using light transmitted through a 10-nm wide aperture to locally illuminate a sample. By scanning the aperture over the sample surface, this microscope would record images of the transmitted light with a spatial resolution given by the diameter of the aperture [Syn28]. Unfortunately, the lack of suitable technology for positioning and illumination of the aperture hampered the realization of his ideas. Nevertheless, the principle of coupling propagating far-field radiation to the strongly-localized evanescent near field of nanometer-sized objects, turned out to be the key ingredient for sub-diffraction-limited imaging. With the development of intense coherent optical light sources in 1960 by Theodore H. Maiman [Mai60] and the invention of scanning tunneling microscopy [Bin83] as well as atomic force microscopy [Bin86], the technological framework was established and Dieter W. Pohl realized the first optical near-field microscope [Poh84]. Today, two main techniques have emerged: (i) Aperture-type near-field scanning optical microscopy (a-NSOM), where the light, transmitted through a small nanometer-sized aperture, is used to extract the local dielectric function of the sample [Bet91]; (ii) scattering-type near-field scanning optical microscopy (s-NSOM), in which a sharp metallic or semiconducting tip is brought close to the sample surface, acting as a light-scattering object. Here, the tip is coupled to the sample via their interpenetrative near fields and the scattered radiation depends on the local dielectric properties of the sample below the tip [Zen94, Ino94, Kaw95, Nov98].

The nearly one-century-old idea of coupling light to the evanescent near field has revolutionized optical microscopy, granting access to the local dielectric properties of nanomaterials from the far-infrared up to the visible spectral range [Zen94, Kno99, Che03, Rot14]. Due to its relatively poor, diffraction-limited spatial resolution of 10 to 1000 µm, the infrared wavelength region is here of particular interest. These frequencies are home to a plethora of low-energy elementary excitations, e.g. phonons, plasmons, magnons or intra-excitonic transitions, which determine the optical and electronic properties of many materials [Ulb11]. Using s-NSOM, these fundamental excitations can now directly be studied with unprecedented spatial resolution, leading to the observation of fascinating phenomena like interfering phonon-polaritons in boron nitride [Dai14] or plasmon-polaritons on the surface of single layer graphene [Che12, Fei12, Ger14, Woe15]. Besides single layer materials, s-NSOM has been successfully employed to study the carrier density and mobility in nanoscale transistors [Hub08] and indium phosphide nanowires [Sti10]. By virtue of the exceptional sensitivity of this technique, an image contrast corresponding to only a few 10 electrons within the near-field probing volume could be achieved. Finally, polymorphism in pentacene films [Wes14] and even nanometer-sized metallic puddles in

the strongly correlated material vanadium dioxide have been resolved, the latter proving unequivocally that metallic domains form and grow as the material is driven through the insulator-to-metal phase transition [Qaz07, Fre09, Liu13, Liu14, Cal15]. The examples highlighted here, clearly indicate the broad application range and the fundamentally new approach to solid-state physics attainable by infrared s-NSOM. Despite its great success over the last few years, time-resolved measurements in infrared s-NSOM are practically non-existent. This comes as a surprise considering that steady-state microscopy fails to catch the very nature of the precise interplay of electrons and ions, which happens on the femtosecond timescale ($1\,\mathrm{fs} = 10^{-15}\,\mathrm{s}$). Studying the effects of strain, defects or local doping on the ultrafast dynamics of electrons and ions as a function of space *and* time would complement femtosecond far-field experiments and significantly increase our understanding of condensed matter systems.

Phase-locked, few-cycle light pulses in the few-terahertz ($0.1 - 10\,\mathrm{THz}$, far-infrared) to multi-terahertz ($10 - 100\,\mathrm{THz}$, mid-infrared) frequency range provide the means to resolve this shortcoming. Field-resolved detection of terahertz (THz, $1\,\mathrm{THz} = 10^{12}\,\mathrm{Hz}$) waveforms by electro-optic sampling has turned time-resolved THz spectroscopy into one of the most powerful tools for studying and controlling the dynamics of low-energy elementary excitations in solids [Fer02, Ton07, Jep10, Ulb11, Kam13]. Direct access to the oscillating electric field upon ultrafast photoexcitation, a property which is exclusive for THz spectroscopy, provides a temporal resolution faster than a single oscillation cycle of the THz pulse and enables the extraction of the complex-valued dielectric function on a sub-cycle timescale [Kin99, Hub01, Něm02, Něm05]. The resonant coupling of THz radiation to low-energy elementary excitations enabled the direct observation of the ultrafast build-up of screening in photoexcited gallium arsenide crystals [Hub01] and the sub-cycle control of magnons in nickel oxide [Kam11]. Even the observation and control of dynamical Bloch oscillations performed by electrons accelerated through the Brillouin zone of a bulk gallium selenide crystal by the electric field of intense THz pulses has been achieved [Sch14]. In addition, ultrabroadband THz spectroscopy has been employed to simultaneously trace the ultrafast evolution of different coexisting order parameters in strongly correlated materials, yielding detailed information about the intricate interplay of electron-electron, electron-phonon and magnetic correlations [Küb07, Pas10, Pas11, Por14a]. Although THz spectroscopy in the few-THz range has been successfully combined with s-NSOM, yielding a spatial resolution down to 150 nm [Hun98, Che03, Che04, Zha07, Rib08, Moo12], no time-resolved studies of single nanoparticles have been reported. Conversely, intensity-based detection schemes have been employed in the multi-THz regime to probe the photoexcited carrier dynamics of single layer graphene [Wag14a] and epitaxially grown indium arsenide [Wag14b].

In this work the first combination of time-resolved multi-THz spectroscopy and scattering-type near-field scanning optical microscopy is introduced. Going beyond intensity-resolved detection, the microscope enables a sub-cycle temporal resolution of 10 fs by field-resolved detection of the scattered radiation while simultaneously achieving a spatial resolution of 10 nm [Eis14]. This fundamentally new approach to time-resolved near-field microscopy has been achieved by combining cutting-edge, custom-tailored erbium-doped fiber laser technology with a state-of-the-art near-field microscope. The ultrafast microscope is employed to study the pump-induced carrier dynamics in indium arsenide nanowires, providing detailed insights into surface effects and carrier density dynamics. Tracing the oscillating electric near field at a distinct position on the nanowire surface as a function of pump-probe delay time reveals the appearance of a plasma resonance within the multi-THz probe pulse spectrum. A thorough theoretical description of the experimental observations is performed within an extended framework of the established point-dipole model. The simulations provide direct access to the time-dependent complex-valued dielectric function and thus the local carrier density in the indium arsenide nanowire, which, on average, corresponds to only a few electrons within the near-field probing volume of $(10\,\mathrm{nm})^3$. Following photoinjection, the carrier density features a bi-exponential decay with an ultrafast decay time < 40 fs and a slower decay time of approximately 2 ps, which is attributed to trapping into surface states. The novel technique of femtosecond tomography [Eis14], which is developed here, is used to record a time-dependent depth profile of the carrier density, identifying the initial ultrafast decay (< 40 fs) as the formation of a depletion layer at the surface of the doped indium arsenide nanowires.

Ultrafast field-resolved near-field microscopy provides direct access to the sub-cycle dynamics of low-energy elementary excitations on the nanoscale, far beyond the fundamental diffraction limit of light. Hence, it paves the way towards a new class of time-resolved experiments in the mid-infrared, where the influence of local confinement or structural irregularities in virtually any physical, chemical and biological process can be studied and imaged in unprecedented detail.

The first part of this thesis describes the technological platform that has been developed to perform ultrafast near-field microscopy (**Chapter 2**). Based on ultrastable erbium-doped fiber laser technology, the optical part of the experimental setup is entirely custom tailored to guarantee ultimate performance. The generation of tunable multi-THz pulses with high average power, 10-fs gate pulses for electro-optic sampling as well as pump pulses in the near-infrared and visible spectral range are discussed. In addition the working principle of near-field microscopy and the implementation of the atomic force microscope in the optical setup is introduced. Intensity-based and field-resolved detection of the scattered near field is explained in the context of the tapping mode operation scheme, which is used for efficient background suppression. The chapter concludes with a first demonstration of field-resolved detection of multi-THz waveforms scattered off a gold sample yielding absolute phase and amplitude information out of the near field.

In **Chapter 3** the microscope is employed to study the pump-induced carrier dynamics of bulk indium arsenide. The scattered radiation is found to be highly susceptible to the photoinjected carrier density, giving rise to strong modulations of the near-field signal as a function of pump-probe delay time. The influence of the carrier density on the scattered spectrum stems from the appearance of a plasmonic resonance within the multi-THz probe pulse spectrum, which is confirmed by spectrally resolved measurements. Furthermore, this chapter introduces the theoretical background to derive the scattering response in the framework of the point-dipole model. Using the Drude formalism to describe the dielectric properties of indium arsenide as a function of carrier density, an excellent agreement between the experiment and the theory is achieved and important parameters like the Drude scattering rate and carrier density as well as recombination times are extracted. Finally, field-resolved detection of the multi-THz radiation scattered off a $(10\,\mathrm{nm})^3$ volume on a single indium arsenide nanowire is employed to investigate the electron dynamics on the sub-nanoparticle scale. In combination with the technique of femtosecond tomography, which is developed here, a depth profile of the carrier dynamics at the surface is recorded and the formation of a surface depletion layer is identified. The experiments performed on the indium arsenide nanowire highlight the full potential of the novel microscope, visualizing photoinduced dynamics with 10 fs temporal resolution and 10 nm spatial resolution.

First time-resolved experiments performed on vanadium dioxide nanowires are presented in **Chapter 4**. This material features a first-order insulator-to-metal phase transition which can be induced either optically or thermally. The origin of this phase transition is the center of a controversial discussion. Near-field imaging of the nanowire heated across the phase-transition temperature reveals a strong influence of surface strain on the

phase transition leading to a periodic formation of insulating and metallic domains. Interestingly, pump-probe scans measured below the phase-transition temperature at various locations on the nanowire exhibit a lower photo-conductivity at positions that develop an insulating character at elevated temperatures than positions with metallic character. The chapter closes with a first interpretation of the observed dynamics.

Chapter 5 gives a brief summary of the experimental and technological achievements of this thesis as well as the results obtained on indium arsenide and vanadium dioxide. An outlook on first ultrafast dynamics observed in single layer graphene and tungsten diselenide flakes highlights the broad application range of the novel microscope.

Chapter 2

Ultrafast multi-terahertz nano-spectroscopy

The novel, femtosecond multi-THz microscope introduced in this work establishes a new paradigm in ultrafast science. For the first time it is possible to observe local low-energy dynamics on the surface of solid-state systems with a temporal resolution on the few-femtosecond scale [Eis14]. This microscope is based on a unique combination of ultrafast, mid-infrared laser technology, tracing the oscillating electric field of light directly in the time domain, with scattering-type near-field scanning optical microscopy (s-NSOM). Phase-stable multi-THz pulses are focused onto the tip of an atomic force microscope which imprints the local optical properties of the sample below the tip on the scattered radiation. Thus, this technique allows one to retrieve nanoscale information from a probe volume as small as $(10\,\mathrm{nm})^3$, approximately nine orders of magnitude smaller than the fundamental diffraction volume. Far-field multi-THz spectroscopy and steady-state near-field microscopy are by themselves well established methods in modern optics. However, the combination of both techniques imposes new challenges on both the laser system and the design of the s-NSOM:

Multi-THz power: S-NSOM is based on scattering light off a nanometer-sized metal tip in an atomic force microscope. The scattering efficiency out of the near field is thereby as low as 10^{-4} as compared to the input intensity. To reasonably perform near-field microscopy, the minimal average power of the multi-THz laser source has to be in the mW range.

Stability: Tentatively, near-field imaging with high spatial resolution and a high signal-to-noise ratio leads to acquisition times ranging from a few minutes to several days. High stability and a low noise characteristic of both the laser source and the atomic force microscope are therefore vital to perform such experiments.

Custom-tailored femtosecond pulses: Efficient multi-THz generation, field-resolved detection and pump-probe measurements require femtosecond laser pulses with precisely tunable spectral and temporal properties to guarantee ultimate performance.

Non-dispersive optics: State-of-the-art near-field microscopes mostly employ highly dispersive object lenses, which strongly distort the temporal shape of femtosecond laser pulses. To achieve the highest possible temporal resolution an alternative scheme based on reflective optical elements has to be chosen.

While the technology for non-dispersive near-field microscopy is nowadays commercially available, the requirements imposed on the optical part of the experimental setup call for an entirely custom tailored laser system. Erbium-doped fiber (Er:fiber) laser technology is most suited in this respect. The large gain bandwidth of Er:fibers together with the tunability of the dispersion characteristics of optical fibers have lead towards all-fiber-based femtosecond laser systems with nJ pulse energies at a wavelength of 1560 nm [Tau03b, Tau04, Bri14]. Since the light pulses are guided in optical fibers these laser systems are completely maintenance-free and have superior characteristics with respect to compactness, spatial and temporal long-term stability [Sel09] and photon noise [Adl07], when compared to conventional titanium-sapphire lasers. With the help of custom-tailored highly-nonlinear germano-silica fibers (HNLF) it is further possible to exploit strong nonlinear processes to generate octave spanning spectra. This development has enabled continuously tunable light pulses with frequency components ranging from 900 to 2600 nm [Tau04, Sel09, Kra10, Bri14] and pulse durations as low as 4.3 fs [Kra10]. These unique properties make Er:fiber lasers an ideal candidate for ultrastable and ultrasensitive multi-THz spectroscopy [Sel08]. Carefully designed supercontinua in HNLF allow for an efficient generation of phase-stable multi-THz pulses by difference frequency generation up to the near-infrared [Ern07, Gam08, Sel08, Kra11]. Furthermore, custom-tailored, ultrashort gate pulses can be generated [Sel09], which are crucial for field-resolved detection of the scattered multi-THz waveforms.

As part of this work a new pump-probe multi-THz spectroscopy setup has been developed. This laser system provides multi-THz pulses via difference frequency generation with pulse durations as low as 60 fs, pulse energies up to 28 pJ and center frequencies ranging from 27 to 55 THz. Field-resolved detection of the multi-THz waveforms by electro-optic sampling (EOS) is achieved by using 10-fs gate pulses that are generated in a HNLF. To investigate non-equilibrium dynamics, the laser system further provides femtosecond excitation pulses both in the near-infrared as well as in the visible spectral range. The spectroscopy setup is combined with a room temperature near-field microscope that is solely based on non-dispersive optics. This way ultrafast multi-THz nano-spectroscopy is achieved with 10 nm spatial resolution and sub-cycle, 10 fs temporal resolution [Eis14].

This chapter will first introduce the basic building blocks of the optical laser system employed for near-field microscopy (**Section 2.1**). The overview is followed by a detailed discussion of multi-THz generation and detection (**Section 2.2**) as well as the generation of ultrafast pump pulses for two-time multi-THz spectroscopy (**Section 2.3**). Finally, the operating principle of s-NSOM and our novel approach of field-resolved detection of the scattered near-field radiation is presented (**Section 2.4**).

2.1 Erbium-doped fiber laser for ultrafast near-field microscopy

The commercially available Er:fiber laser system[1] employed in this experiment is based on an Er:fiber oscillator operating at a fundamental repetition rate of 40 MHz (Fig. 2.1). The oscillator output is divided into three inherently coherent pulse trains which subsequently seed Amplifiers I - III. The amplifiers enhance the pulse energy of the oscillator pulses in the range of 9 to 15 nJ with pulse durations below 100 fs. The near-infrared pulses from Amplifiers I and II are used to generate multi-THz waveforms via difference frequency generation (DFG) in a gallium selenide (GaSe) crystal. To this end, the pulses from both amplifiers are spectrally shaped by nonlinear pulse propagation in a HNLF and/or a NLF and spatially overlapped via a dichroic mirror. To match the temporal offset between the pulse trains in the GaSe crystal, a delay line (t_{DFG}) is inserted in the beam path of Amplifier I. The generated phase-stable multi-THz probe pulses are then sent into the s-NSOM where they are scattered off a sharp metal tip. Detection of the scattered multi-THz radiation is achieved either intensity-resolved using a mercury cadmium telluride (MCT) photodiode or field-resolved employing EOS. To eliminate spurious background radiation in the detection schemes, the tip is operated in tapping mode, oscillating above the sample surface with a frequency Ω_{tip} and an adjustable tapping amplitude of 40 to 250 nm. The near field scattered off the tip thereby depends nonlinearly on the tip-sample distance. Thus, measuring the scattered radiation at higher harmonics of Ω_{tip} efficiently isolates the pure near-field signal and enables a spatial resolution on the nanometer scale, far below the diffraction limit (see Section 2.4).

The ultrashort gate pulses, crucial for field-resolved detection by EOS, are custom-tailored with the help of a NLF and HNLF from the output pulses from Amplifier III. A high-precision fast-scan delay stage (t_{EOS}) is used to adjust the temporal overlap between the multi-THz waveform and the gate pulses. With acquisition times of less than 1 s, a stroboscopic time trace of the transient electric field of the multi-THz pulses can be recorded, which will be explained in detail in Section 2.2.2. To reduce the noise floor in the detection scheme of EOS the repetition rate of the seed of Amplifier I is down-sampled

[1] FemtoFiber pro IR, TOPTICA Photonics AG, 82166 Gräfelfing, Germany

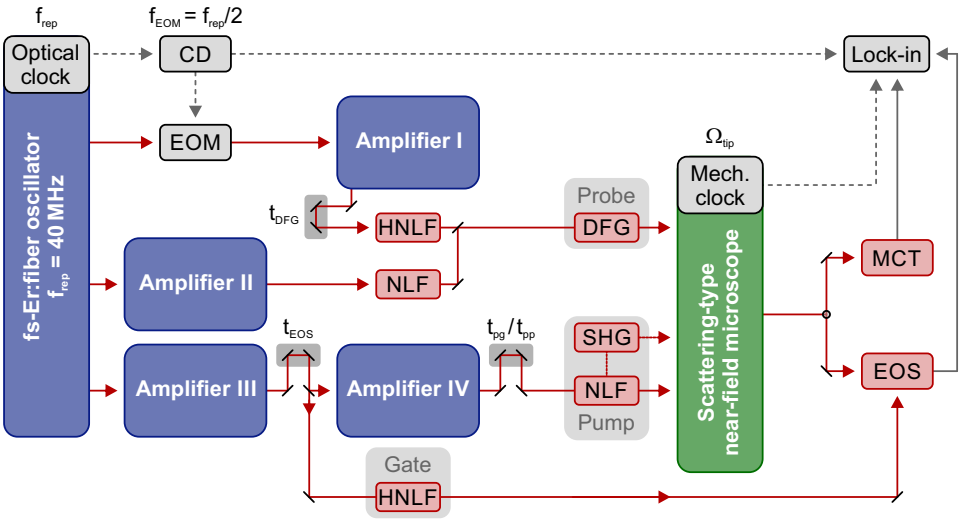

Figure 2.1 | Schematic of the ultrafast erbium-doped fiber laser system. A femtosecond erbium-doped fiber (Er:fiber) oscillator with a repetition rate $f_{\mathrm{rep}} = 40\,\mathrm{MHz}$ directly seeds Amplifiers I - III. The repetition rate of Amplifier I is down-sampled to 20 MHz using an electro-optic modulator (EOM) synchronized to $f_{\mathrm{rep}}/2$ by a clock divider (CD). The pulses from Amplifier III pass a high-precision fast-scan delay stage t_{EOS} followed by a beam sampler that provides the seed pulses for Amplifier IV. The pulses from each amplifier are custom-tailored using nonlinear (NLF) and/or highly-nonlinear fibers (HNLF). Difference frequency generation (DFG) of the pulses from Amplifiers I and II provides phase-stable multi-THz pulses in the mid-infrared spectral range (wavelength $5-11\,\mu\mathrm{m}$). The temporal overlap of the generating near-infrared pulse trains is established by a delay line (t_{DFG}) after Amplifier I. The multi-THz probe pulses are then used to perform ultrafast near-field microscopy. Near-infrared pump pulses are provided by Amplifier IV. These pulses can optionally be frequency doubled by second harmonic generation (SHG) to generate pump pulses in the visible spectral range ($\approx 790\,\mathrm{nm}$). A delay line after Amplifier IV is used to adjust the pump-probe delay time t_{pp} or the pump-gate delay time t_{pg}. The pulses from the near-field microscope are detected using an intensity resolving mercury cadmium telluride (MCT) photodiode or by electro-optic sampling (EOS) using ultrashort pulses (10 fs) from Amplifier III. All signals are recorded using lock-in detection: MCT signals are referenced to a higher harmonic of the mechanical tip oscillation frequency ($n \cdot \Omega_{\mathrm{tip}}$). Near-field signals measured by EOS are detected at a sideband frequency $f_{\mathrm{EOM}} + n \cdot \Omega_{\mathrm{tip}}$.

by an electro-optic modulator to $f_{\mathrm{EOM}} = 20\,\mathrm{MHz}$, allowing for low-noise lock-in detection at the Nyquist frequency of the laser system [Sel09]. Consequently, the scattered radiation recorded by EOS is measured at a sideband frequency $f_{\mathrm{EOM}} + n \cdot \Omega_{\mathrm{tip}}$ with $n \in \mathbb{N}$. This way, the pure near field can be isolated from the background radiation while simultaneously performing low-noise EOS.

To enable the observation of non-equilibrium dynamics Amplifier IV is designed to generate 22-fs pump pulses in the near-infrared using a NLF. These pulses can optionally be frequency doubled in a periodically-poled lithium niobate (PPLN) crystal to generate ultrafast pump pulses in the visible wavelength region ($\approx 790\,\mathrm{nm}$) (see Section 2.3.2). To seed Amplifier IV, a fraction of the power output from Amplifier III is picked off behind the EOS delay line with a beam sampler (Reflectivity $\approx 10\,\%$)[2]. This concept allows for an intrinsic synchronization of the pump and gate pulses with respect to the multi-THz probe pulses, which is a prerequisite to perform two-time multi-THz spectroscopy with ultimate temporal resolution (see Section 2.3). To adjust the delay of the pump with respect to the probe or gate pulses an additional delay line (pump-probe delay t_{pp}, pump-gate delay t_{pg}) is implemented in the beam path after Amplifier IV.

2.1.1 Nonlinear pulse propagation in optical fibers

One of the key properties of Er:fiber laser technology, which is exploited in the optical setup presented here, is the possibility to custom-tailor the temporal and spectral properties of the near-infrared light pulses in a wide range by nonlinear pulse propagation in optical fibers. However, to efficiently exploit the high tunability of the Er:fiber laser pulses, a quantitative understanding of the underlying propagation effects inside the NLF and HNLF fibers is invaluable. For a comprehensive description, both the wavelength dispersion as well as nonlinear processes have to be considered. In a simplified picture, the pulse propagation can be expressed using the following nonlinear Schrödinger equation [Agr07]

$$\partial_z A(z,\tau) = -i\frac{\beta_2}{2}\partial_\tau^2 A(z,\tau) + i\gamma|A(z,\tau)|^2 A(z,\tau)\ . \tag{2.1}$$

$A(z,\tau)$ is the pulse envelope as a function of propagation distance z in the fiber and the retarded time $\tau = t - \beta_1 z$ relative to the input pulse. Here, β_1 is the group velocity of the pulses inside the fiber. The first part on the right accounts for the group velocity dispersion using the Taylor expansion coefficient $\beta_2 = \frac{d^2}{d\omega^2}\frac{\omega}{c}n(\omega)$ of the effective refractive index $n(\omega)$ of the glass fiber. The second term on the right describes the nonlinear

[2] The beam sampler is followed by a spectral filter that narrows the broad seed spectrum from Amplifier III to a bandwidth of 12 nm at a center wavelength of 1560 nm. This is necessary since the direct use of broadband seed pulses from Amplifier III could lead to a strong temporal distortion of the output pulses after amplification in Amplifier IV.

propagation inside the fiber due to self-phase modulation [Agr07]. The strength of the nonlinearity is thereby characterized by the parameter $\gamma = \frac{2\pi n_2}{\lambda A_{\text{eff}}}$, with the effective mode field diameter A_{eff} and the second order nonlinear refractive index n_2.

In the context of solving this differential equation it is helpful to introduce the following effective length scales [Agr07]

$$L_{\text{GVD}} = \frac{T_0^2}{|\beta_2|} \ , \quad L_{\text{NL}} = \frac{1}{P_0 \gamma} \ , \quad N = \frac{L_{\text{GVD}}}{L_{\text{NL}}} \ ,$$

with T_0 and P_0 being the pulse duration and the peak power of the laser pulses, respectively. L_{GVD} is the length scale on which the group velocity dispersion (GVD) becomes significant, whereas L_{NL} is the length scale where nonlinear (NL) effects, like self-phase modulation, have to be considered. The solitonic order N is an indicator of whether nonlinear processes ($N \gg 1$) or dispersive effects ($N \ll 1$) dominate the propagation of the laser pulses inside the fiber. For $N = 1$ and negative GVD, dispersive and nonlinear effects exactly balance and a stable solution of Equation 2.1 is found. This solution corresponds to a so called solitonic pulse that propagates through the fiber with a preserved field envelope $A(z, \tau)$

$$A(z, \tau) = \sqrt{P_0} \ \text{sech}\left(\frac{\tau}{T_0}\right) \exp\left(\frac{iz}{2L_{\text{GVD}}}\right) \ . \tag{2.2}$$

For $N > 1$ the temporal shape of the solitonic field envelope is not stable anymore but evolves periodically during propagation. After a certain propagation distance, the pulse duration of the soliton can thereby be reduced substantially, which is known as solitonic pulse compression.

In order to achieve a quantitative agreement between the theory and the experiment, Equation 2.1 has to be extended to incorporate absorption, higher-order dispersion terms and additional nonlinear effects like Raman scattering. The nonlinear Schrödinger equation then reads [Sel09]

$$\begin{aligned} \partial_z A(z, \tau) = &\left[-\frac{\alpha}{2} - i \sum_{j=2}^{n} (-1)^j \frac{\beta_j}{j!} \partial_\tau^j \right] A(z, \tau) \\ &+ \gamma \left(i - \frac{\partial_\tau}{\omega_0} \right) \left[A(z, \tau) \int_{-\infty}^{+\infty} |A(z, \tau_1)|^2 R(\tau - \tau_1) d\tau_1 \right] \ . \end{aligned} \tag{2.3}$$

The first part on the right accounts for the linear effects within the fiber, such as damping (damping coefficient α) and dispersion (Taylor expansion coefficients $\beta_j = \left(\frac{d}{d\omega}\right)^j \frac{\omega}{c} n(\omega)$). Nonlinear propagation effects are represented by the second term with the nonlinear

response function $R(\tau)$ that describes the temporal evolution of the $\chi^{(3)}$ nonlinearity

$$R(\tau) = (1 - f_\mathrm{R})\delta(\tau) + f_\mathrm{R} h_\mathrm{R}(\tau)\Theta(\tau) \ . \tag{2.4}$$

The response function is composed of a δ-distribution which accounts for the quasi-instantaneous electronic Kerr effect, and a temporally retarded response $h_\mathrm{R}(\tau)\Theta(\tau)$ that incorporates the Raman contributions. Both effects are weighted with an empirical factor f_R. The Raman response $h_\mathrm{R}(\tau)$ is derived from a measured Raman amplification spectrum [Sto89, Sel09].

Experimental verification of the derived model

To model the propagation of the laser pulses in our experiment, a simulation software developed by A. Sell [Sel09] is employed, which is based on an optimized split-step algorithm [Agr07]. Except for the parameters of the input pulses, the simulation is entirely parameter free. Dispersion and absorption are determined by measuring the fiber transmission in a broadband, white-light Fourier transform spectrometer, whereas the nonlinear coefficient γ is calculated from the effective mode field diameter A_eff supplied by the manufacturer.

The good agreement between the experiment and the simulations can be seen by comparison with a broadband supercontinuum (Fig. 2.2a (black curve)) that is generated by nonlinear pulse propagation. Laser pulses from an Er:fiber amplifier with a pulse energy of $E_\mathrm{pulse} = 4.2\,\mathrm{nJ}$ and a pulse duration of $\tau_\mathrm{pulse} < 100\,\mathrm{fs}$ are focused into a 9-cm long NLF[3] prechirp-fiber. Within the prechirp-fiber, the propagation is determined by anomalous dispersion in combination with self-phase modulation. A soliton with $N > 1$ forms, leading to a strong reduction of the pulse duration due to solitonic pulse compression. The prechirp-fiber is then followed by a 7-mm long HNLF[4] in which the pulses are spectrally broadened by self-phase modulation. The HNLF features a highly red-shifted zero-dispersion wavelength as compared to the NLF. Thus, spectral components above 1400 nm experience anomalous dispersion leading to the formation of a stable long-wavelength soliton. The short-wavelength contributions, however, experience normal dispersion and form a dispersive pulse which suffers from temporal broadening. The two pulses interact via four-wave mixing, leading to the generation of an ultrabroadband supercontinuum ranging from 900 to 2000 nm. The results from the simulation can be seen in Fig. 2.2b (black curve). The measured spectrum of the Er:fiber amplifier (Fig. 2.2a, red curve) is here used as an input pulse, whereby the phase is adjusted for best agreement. The general shapes of the dispersive and solitonic wavelength contributions are nicely reproduced, as are the

[3] LPC-04-1550-8/125-P-1.2-6.2AS-60-X-1-1, OZ Optics, K0A 1L0 Ottawa, Canada
[4] GF4A, Thorlabs, 85221 Dachau, Germany

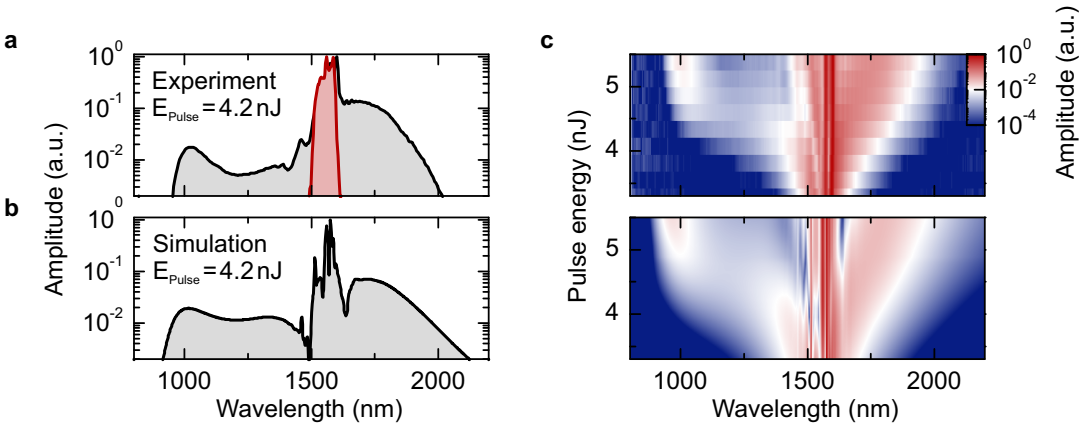

Figure 2.2 | Ultrabroadband continuum generation in highly nonlinear fibers. **a**, Broadband supercontinuum (black curve) generated by nonlinear pulse propagation in a 9-cm long NLF followed by a 7-mm long HNLF. Laser pulses from an Er:fiber amplifier with a pulse duration of less than 100 fs and a pulse energy of 4.2 nJ are used as input pulses. The spectrum of the input pulses is depicted as a red curve. **b**, Simulated spectrum using the same fiber combination and pulse energy as in **a**. **c**, Experimental (upper panel) and theoretical (lower panel) comparison of the generated continua after nonlinear pulse propagation as a function of output pulse energy.

high and low wavelength cut-offs. The agreement is even more pronounced in Fig. 2.2c, where the continua generated in the experiment and the simulation are color-coded as a function of the output pulse energy. With increasing pulse energy, self-phase modulation leads to a broadening of the spectrum. For pulse energies exceeding 4 nJ, efficient four wave mixing starts to generate a broadband continuum that is highly tunable with the help of the pulse energy and the dispersion of the input pulses.

In summary, modeling the nonlinear pulse propagation in glass fibers allows for a good estimate of the pulse duration and spectral shape and is used to custom-tailor the pulses from each amplifier in our setup, as can be seen in the following sections.

2.2 Generation and detection of ultrabroadband, phase-stable multi-terahertz waveforms

To perform femtosecond near-field microscopy in the mid-infrared, broadband multi-THz radiation is generated by exploiting the nonlinear polarization response of solids subjected to intense laser fields. Unlike the linear, low-field regime, where the electron and ion movement is directly proportional to the external driving field, the polarization response of the charged particles becomes highly anharmonic in the nonlinear case. For solids featuring a non-centrosymmetric crystal lattice, the anharmonic motion can thereby lead

to effects like optical rectification and difference frequency generation (DFG), where the visible or near-infrared driving frequencies are down-converted to the far or mid-infrared. The approach of optical rectification has been shown to produce THz and multi-THz pulses [Ric94, Bon95, Kai99, Liu04] with frequencies exceeding 40 THz [Hub00]. Since optical rectification can be regarded as DFG between the different frequency components within a laser-pulse spectrum, the highest attainable multi-THz frequencies are directly related to the spectral bandwidth of the generating pulses. This concept therefore becomes strongly inefficient with increasing multi-THz frequencies, since only the spectral wings, which have relatively low intensities, contribute to the generation of multi-THz radiation [Sel08]. An approach to overcome this limitation is the use of DFG [Pet01] between two spectrally detuned laser pulses, which are coherent with respect to each other. The detuning is chosen such that the spectral weight of the generating visible or near-infrared laser pulses is maximized with a frequency separation corresponding to the desired multi-THz frequency.

Importantly, optical rectification and DFG are driven by mutually coherent laser pulses. Thus, the unstable carrier envelope phase cancels [Bal02, Zim04, Sel08] and the THz and multi-THz waveforms are intrinsically phase stable, i.e. they feature a defined relationship between their oscillating electric field and their pulse envelope. This unique property is crucial for the direct observation of the electric field of the multi-THz pulses in the time domain (see Section 2.2.2) and is the foundation of the success of THz spectroscopy.

2.2.1 Multi-terahertz generation by difference frequency generation

The high spectral tunability of femtosecond Er:fiber lasers combined with DFG provides a versatile basis to generate multi-THz pulses [Gam08, Sel08] with frequencies up to the near-infrared [Kra11] and conversion efficiencies up to 30 % [Ern07]. The nonlinear generation of multi-THz radiation can thereby be described by an optical parametric amplification process (see Fig. 2.3). A pump pulse with a center frequency ν_1 (black pulse in Fig. 2.3a) and a signal pulse with a center frequency ν_2 (green pulse) are focused into a non-centrosymmetric gallium selenide (GaSe) crystal. By difference frequency generation, a new laser pulse, the idler, is generated at the difference frequency $\nu_3 = \nu_1 - \nu_2$ (red pulse). The intensity I_3 of the generated multi-THz radiation at the frequency ν_3 is given by [Boy08]

$$I_3 \propto I_1 I_2 L^2 \cdot \mathrm{sinc}^2\left(\frac{L}{L_{\mathrm{coh}}}\right) , \tag{2.5}$$

with the input intensity of the pump (I_1) and the signal (I_2), the length L of the nonlinear medium and the phase-matching factor $\mathrm{sinc}^2(\frac{L}{L_{\mathrm{coh}}})$. The coherence length $L_{\mathrm{coh}} = 2/\Delta k$ determines the propagation length of the pulses within the nonlinear medium where co-

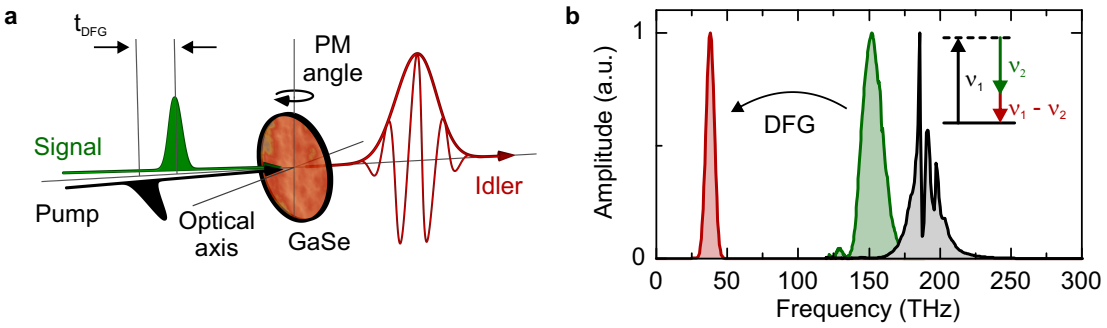

Figure 2.3 | Process of difference frequency generation. **a**, Schematic of the difference frequency generation (DFG) process. The ordinary polarized signal pulse (green) and the extraordinary polarized pump pulse (black) are focused into a nonlinear, birefringent gallium selenide (GaSe) crystal by a non-collinear focusing geometry. The temporal delay between the pulses can be adjusted with a delay line t_{DFG}. Phase-matching is achieved by rotation of the crystal (PM angle) perpendicular to the optical axis. By DFG, phase-stable, few-cycle multi-THz pulses are generated (red, idler). **b**, Experimentally measured frequency components of the pulses illustrated in **a**. Pump and signal are centered at 191 THz (corresponding wavelength 1.56 µm) and 152 THz (1.96 µm), respectively. The generated idler pulses are centered at 38 THz (7.87 µm). The inset depicts the energy level description for DFG. A pump photon excites an electron into virtual energy state (dashed line), which is depleted by stimulated emission, generating a new signal and idler photon.

herent build-up of the generated multi-THz radiation is possible. Difference frequency generation at a given crystal length is therefore most efficient when the momentum mismatch Δk between the participating frequencies of the pump, signal and idler pulses vanish, a condition known as phase matching [Boy08]

$$\Delta k = k_1 - k_2 - k_3 = \frac{n_1\omega_1}{c} - \frac{n_2\omega_2}{c} - \frac{n_3\omega_3}{c} \stackrel{!}{=} 0 \; . \tag{2.6}$$

Here, $n_i = n(\omega_i)$ are the refractive indices at the frequency $\omega_i = 2\pi \cdot \nu_i$ with $i = 1, 2, 3$. For birefringent crystals like GaSe, this condition can be fulfilled by tuning the crystal's phase-matching (PM) angle and the polarization of the laser pulses. The PM angle thereby describes the angle between the signal pulse with ordinary polarization and the optical axis of the GaSe crystal. However, when dealing with broadband laser pulses, phase-matching can not be established for all frequencies simultaneously, due to the different dispersion of the ordinary and extraordinary refractive indices. In this case, the wavevectors $k_i(\omega_i)$ can be expanded in a Taylor series around their respective center frequencies yielding

$$k(\omega_i) \approx \frac{n_i\omega_i}{c}\Big|_{\tilde{\omega}_i} + \frac{\partial k_i}{\partial \omega}\Big|_{\tilde{\omega}_i} \cdot \Delta\omega_i + \frac{1}{2}\frac{\partial^2 k_i}{\partial \omega^2}\Big|_{\tilde{\omega}_i} \cdot (\Delta\omega_i)^2 + \dots \; , \tag{2.7}$$

with $\Delta\omega_i = \tilde{\omega}_i - \omega_i$. The wavevector mismatch can than be written as follows

$$\Delta k = \Delta k^0 + \Delta k^1 + \dots \ . \tag{2.8}$$

Here, the zeroth order of the expansion $\Delta k^0 = n_1\tilde{\omega}_1/c - n_2\tilde{\omega}_2/c - n_3\tilde{\omega}_3/c$ corresponds to the phase matching condition shown in Equation 2.6. The spectral bandwidth of the laser pulses results in a non-zero first order expansion coefficient

$$\begin{aligned}\Delta k^1 &= \frac{\partial k_1}{\partial\omega}\Big|_{\tilde{\omega}_1} \cdot \Delta\omega_1 - \frac{\partial k_2}{\partial\omega}\Big|_{\tilde{\omega}_2} \cdot \Delta\omega_2 - \frac{\partial k_3}{\partial\omega}\Big|_{\tilde{\omega}_3} \cdot \Delta\omega_3 \\ &= \Big(\frac{\partial k_1}{\partial\omega}\Big|_{\tilde{\omega}_1} - \frac{\partial k_3}{\partial\omega}\Big|_{\tilde{\omega}_3}\Big) \cdot \Delta\omega_1 - \Big(\frac{\partial k_2}{\partial\omega}\Big|_{\tilde{\omega}_2} - \frac{\partial k_3}{\partial\omega}\Big|_{\tilde{\omega}_3}\Big) \cdot \Delta\omega_2 \ . \end{aligned} \tag{2.9}$$

The second line has been calculated by using the energy conservation of the difference frequency generation process $\hbar\omega_3 = \hbar\omega_1 - \hbar\omega_2$. By assuming the phase matching condition in zeroth order to be fulfilled ($\Delta k^0 \approx 0$) and by using a fixed pump frequency ($\Delta\omega_1 \approx 0$), the phase mismatch is approximated by [Bri10]

$$\Delta k \approx \Big(\frac{1}{v_{g3}} - \frac{1}{v_{g2}}\Big) \cdot \Delta\omega_2 = \delta^{si}_{\mathrm{GVM}} \cdot \Delta\omega_2 \ , \tag{2.10}$$

where the definition of the group velocity $1/v_{gi} = \partial k_i/\partial\omega$ is used. Here, $\delta^{si}_{\mathrm{GVM}}$ is defined as the group velocity mismatch of the signal and the idler pulses which leads to a temporal walk-off between the different laser pulses during propagation in the crystal.

To produce the signal and the pump for the DFG process, the pulses from Amplifier I and II are spectrally shaped by nonlinear pulse propagation in a HNLF and/or NLF (see Fig. 2.1). The pulses from Amplifier I (repetition rate $f_{\mathrm{rep}} = 20\,\mathrm{MHz}$, pulse energy $E_{\mathrm{pulse}} = 16\,\mathrm{nJ}$) are focused into a 5.5-cm long NLF prechirp-fiber. As discussed in Section 2.1.1, nonlinear pulse propagation leads to a reduction of the pulse duration due to solitonic pulse compression. The prechirp-fiber is followed by 10 mm of HNLF in which a solitonic pulse forms and is subsequently red-shifted by four-wave mixing. Since solitonic pulse propagation preserves the temporal pulse shape, the transmitted soliton is intrinsically compressed close to its bandwidth limit. The solitonic part (calculated pulse duration $= 30\,\mathrm{fs}$, $E_{\mathrm{pulse}} = 1.5\,\mathrm{nJ}$ and $\lambda_{\mathrm{signal}} = 1960\,\mathrm{nm}$) is then used as the ordinary polarized signal (Fig. 2.3b, green curve) in the DFG process. The extraordinary polarized pump pulse (black curve) is provided by Amplifier II ($f_{\mathrm{rep}} = 40\,\mathrm{MHz}$, $E_{\mathrm{pulse}} = 9\,\mathrm{nJ}$). Here, the pulse duration is reduced by solitonic pulse compression in a 4.7-cm long NLF (pulse duration $= 30\,\mathrm{fs}$, $E_{\mathrm{pulse}} = 5\,\mathrm{nJ}$, $\lambda_{\mathrm{pump}} = 1560\,\mathrm{nm}$) to match the pulse duration of the signal pulses. Both the pump and signal pulses are temporally overlapped with the help of a delay line (t_{DFG}) and focused into a 1-mm thick GaSe crystal to a focal spot-size of $\omega_0 = 15\,\mu\mathrm{m}$.

The focal radius results in an effective nonlinear interaction length given by twice the Rayleigh range $2z_R = 2\pi\omega_0^2/\lambda_{pump} \approx 0.8\,\text{mm}$, optimally exploiting the crystal thickness. The group velocity mismatches are calculated to be $\delta_{GVM}^{sp} = 1/v_{gs} - 1/v_{gp} \approx -53\,\text{fs/mm}$, $\delta_{GVM}^{si} = 1/v_{gs} - 1/v_{gi} \approx 131\,\text{fs/mm}$ and $\delta_{GVM}^{pi} = 1/v_{gp} - 1/v_{gi} \approx 185\,\text{fs/mm}$, resulting in a decent temporal overlap of the pulses over the entire crystal length. Here, v_{gp}, v_{gs} and v_{gi} are the group velocities of the pump, signal and idler pulses, respectively, calculated at the corresponding center frequencies of $\lambda_{pump} = 1560\,\text{nm}$, $\lambda_{signal} = 1960\,\text{nm}$ and $\lambda_{idler} = 7650\,\text{nm}$. Due to the birefringence of GaSe, the extraordinary pump pulses experience a significant spatial walk-off with a walk-off angle of 4 ° [Gam08]. This effect is partially compensated by a non-collinear focusing geometry of the signal and pump pulses, with a relative external angle of approximately 1 °. The generated DFG spectrum with the highest pulse energy is shown by the red curve in Fig. 2.3b, featuring a Gaussian shape with center frequency of 38 THz ($\lambda_{idler} = 7.87\,\mu\text{m}$).

Spectral tunability of the multi-terahertz radiation

The birefringence of the GaSe crystal can be used to spectrally tune the center frequency of the generated multi-THz radiation via the PM angle. Since both signal and pump feature a broad frequency spectrum, the resulting multi-THz pulses can be adjusted to cover frequencies in the range between 20 and 60 THz. Selected multi-THz spectra for different external PM angles are depicted in Fig. 2.4a. The spectra exhibit a Gaussian shape with an average bandwidth of 10 THz (full-width at half-maximum, FWHM). The peaks visible in the spectra at PM angles of 37° and 39° originate from the strongly structured pump spectrum as can be seen in Fig. 2.3b (black curve). Fig. 2.4b shows the multi-THz output power as a function of the DFG delay (t_{DFG}). At $t_{DFG} = 0\,\text{fs}$ the signal and pump pulses are temporally overlapped. By tuning t_{DFG} the generated power decreases to 50 % within ±25 fs, indicating that the pulse duration of the signal and pump pulses inside the GaSe crystal is approximately 35 fs. Fig. 2.4c summarizes the properties of the generated multi-THz radiation. Both pulse energy (red) and center frequency (black) are displayed as a function of the PM angle. The gray shaded area indicates the FWHM bandwidth of the multi-THz spectrum. Center frequencies between 27 and 52 THz are attainable with pulse energies ranging from 4 to 28 pJ ($80 - 560\,\mu\text{W}$), measured after filtering the remaining radiation of the generation pulses[5]. The DFG setup developed here exhibits an increase of the multi-THz pulse energy by at least 25 % compared to previously reported DFG systems based on Er:fiber laser technology [Gam08, Sel08, Kei12, Gam13].

[5] Longpass Filter IR 4.5 µm, 68655, Edmund Optics GmbH, 76227 Karlsruhe, Germany

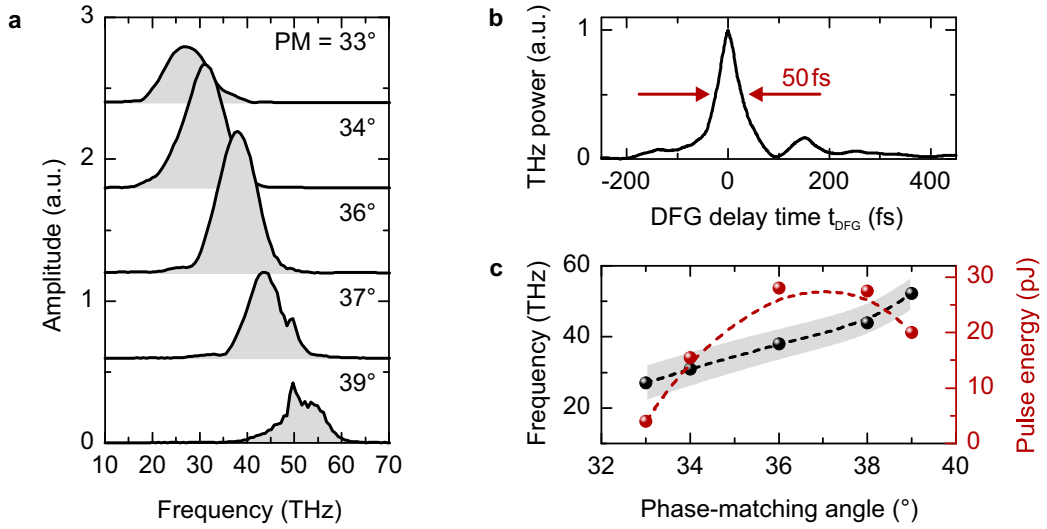

Figure 2.4 | Spectral tunability of the multi-THz pulses. **a**, Multi-THz spectrum for selected external phase-matching (PM) angles. The spectra are Gaussian shaped with an average spectral bandwidth of approximately 10 THz (FWHM). The distinct spectral peaks in the amplitude spectrum for PM angles larger than 37° originate from the strongly structured pump spectrum, as can be seen in Fig. 2.3b. **b**, Dependence of the multi-THz output power on the relative delay time t_{DFG} between the signal and pump pulses. At full temporal overlap ($t_{\mathrm{DFG}} = 0$), the generated output power exhibits a peak with a width of 50 fs (FWHM). **c**, Multi-THz pulse energy (red) and center frequency (black) as a function of the phase-matching angle. The frequency bandwidth (FWHM) is visualized by the gray shaded area. The dots correspond to the spectra shown in **a**.

Carrier envelope phase-stability of the multi-THz waveforms

An important feature of multi-THz generation by DFG or optical rectification is the inherent phase-stability of the generated pulses, i.e. the electric field is identical for each pulse. This property can not be overestimated since it enables the precise control the electric field of a light pulse on the femtosecond scale [Sch14] and is key to field-resolved THz spectroscopy. In contrast, typical laser sources that are used to generate THz or multi-THz radiation are not phase-stable. Hence, these lasers emit a pulse train of femtosecond light pulses at a repetition rate f_{rep} with a varying carrier envelope phase Φ_{CE}. Φ_{CE} thereby describes the offset of the electric-field maximum relative to the field envelope, as seen in Fig. 2.5a. The pulse-to-pulse variation of Φ_{CE} stems from a phase and group velocity mismatch of the propagating pulses inside the laser oscillator. In the frequency domain the pulse train corresponds to a frequency comb with a spectral line spacing of f_{rep}, which is shifted by the offset f_{CEO} (Fig. 2.5b). Thus, each comb line can

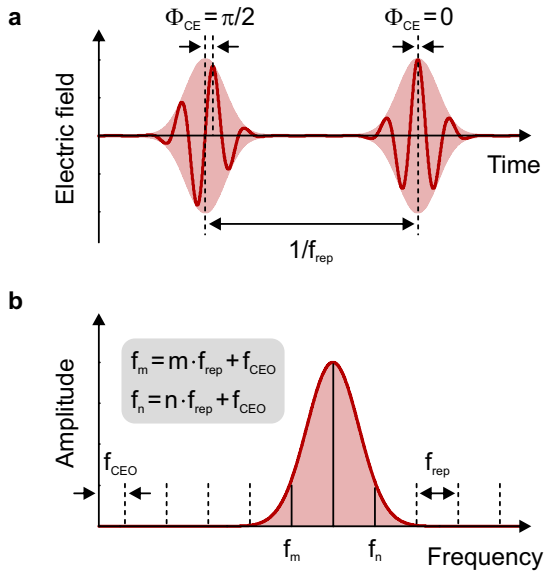

Figure 2.5 | The carrier envelope phase of a light pulse. a, Pulse train emitted from a femtosecond laser source with a repetition rate f_{rep}. The red-shaded area depicts the field envelope and the red curve the electric field of the pulses. The offset of the electric field maximum with respect to the field envelope describes the carrier envelope phase Φ_{CE}. **b**, Frequency comb generated by the pulse train in **a**. The red-shaded area displays the frequency spectrum of a single laser pulse. The comb lines have a equidistant spacing of f_{rep} and the complete frequency comb is shifted by the carrier envelope offset frequency f_{CEO}. For vanishing f_{CEO} the light pulses are phase stable with a constant Φ_{CE}. Note, that the frequencies of the comb lines (e.g. f_m) in the optical laser frequency spectrum are on the order of a few 100 THz, while the spacing between neighboring frequency comb lines is typically in the kHz to MHz range, given by f_{rep}.

be written as

$$f_l = l \cdot f_{\mathrm{rep}} + f_{\mathrm{CEO}} \quad (l \in \mathbb{N}) \ , \tag{2.11}$$

where f_{CEO} is the carrier envelope offset frequency that is determined by the change of Φ_{CE} between successive laser pulses[6]. By generating the difference frequency f_{THz} between two comb modes, f_{CEO} exactly cancels, which in turn results in a constant Φ_{CE}

$$f_{\mathrm{THz}} = f_m - f_n = m \cdot f_{\mathrm{rep}} - n \cdot f_{\mathrm{rep}} \quad (m, n \in \mathbb{N}) \ . \tag{2.12}$$

In the case of DFG the simple illustration of Fig. 2.5 has to be extended to two laser pulse trains that are spectrally detuned with respect to each other (see Fig. 2.3b). Importantly, these pulse trains have to share the exact same frequency comb with an identical f_{CEO}. For the laser system employed in this work, this is guaranteed by the use of a common seed laser (Er:fiber oscillator) for all Er:fiber amplifiers (see Fig. 2.1). Hence, DFG between Amplifier I and II leads to the generation of phase-stable multi-THz pulses, whose oscillating electric fields can be measured in a stroboscopic fashion using ultrashort gate pulses, which is discussed in the next section. An additional feature of multi-THz gen-

[6] $f_{\mathrm{CEO}} = f_{\mathrm{rep}} \cdot (\Delta\Phi_{\mathrm{CE}} \mod 2\pi)/2\pi$, where $\Delta\Phi_{\mathrm{CE}}$ is the pulse-to-pulse change of the carrier envelope phase Φ_{CE}.

eration by DFG is the influence of the delay time t_{DFG} on the absolute carrier envelope phase Φ_{CE}

$$\Phi_{\mathrm{CE}} = 2\pi \cdot f_{\mathrm{THz}} \cdot t_{\mathrm{DFG}} \ . \tag{2.13}$$

Hence, by tuning t_{DFG} the carrier envelope phase Φ_{CE} can be adjusted. However, for long acquisition times, as it is often the case in near-field microscopy, thermal drift between the two pulse trains leads to a variation of Φ_{CE} in time. Nevertheless, for the experiments presented here, the thermal drift can be accounted for, as shown in Appendix A.

2.2.2 Field-resolved detection of multi-terahertz waveforms

The ultimate way of detecting optical pulses is to resolve their oscillating electric field directly in the time domain. The main challenge, however, is the bandwidth of the detector. The electric field of light oscillates with frequencies much higher than 10^{12} Hz, setting the bandwidth requirements of the detector to the same order of magnitude. Conventional electronic detectors are currently limited to frequency bandwidths below 1 THz [Nov12], making it impossible for them to directly trace the oscillating electric field of light. An approach to overcome this limitation is the use of ultrafast gating techniques like streaking spectroscopy [Kra14, Wim14] or electro-optic sampling (EOS) [Wu95, Hub00, Sel08].

In the field of THz and multi-THz spectroscopy, EOS has been established as the method of choice since it enables low-noise data acquisition at the shot-noise limit of the employed gate pulses [Hub00, Por14b]. The working principle of EOS can be seen in Fig. 2.6a. A phase-stable multi-THz pulse (red, ordinary polarized) is focused into a 180-µm thick GaSe crystal. An ultrafast gate pulse (green, extraordinary polarized) is overlapped with the multi-THz pulse in the crystal and their relative arrival time is adjusted using a delay stage (t_{EOS}). In the GaSe crystal, nonlinear sum and difference frequency mixing between the gate and the multi-THz pulses occurs, leading to the creation of new photons at the frequency $f_{\mathrm{gate}} \pm f_{\mathrm{THz}}$ [Gal99]. These photons are ordinary polarized, resulting in an elliptical polarization of the formerly linearly polarized gate beam. Like with the multi-THz generation, phase matching is achieved by adjusting the PM angle of the GaSe crystal [Liu04, Küb04].

In a more intuitive picture, the process of EOS can also be explained by the Pockels effect. The electric field of the multi-THz pulse induces a transient birefringence in the nonlinear crystal, which is sampled by the gate pulse on a sub-THz-cycle timescale. The birefringence thereby introduces a phase retardation between the linear polarization components of the gate pulse, resulting in an elliptical polarization. The retardation can be recorded using an ellipsometer consisting of a quarter-wave plate and a Wollaston

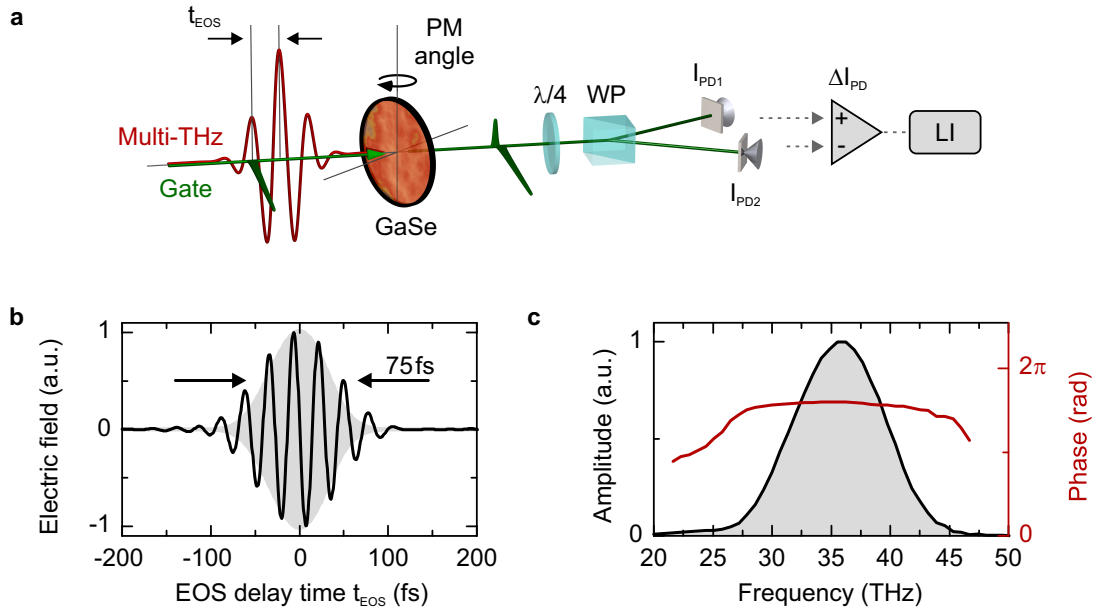

Figure 2.6 | Field-resolved detection by electro-optic sampling. **a**, Illustration of the electro-optic sampling (EOS) process. A multi-THz pulse (red) is focused into a GaSe crystal. The instantaneous electric field induces a birefringence, which introduces a phase retardation between the linear polarization components of a collinear propagating gate pulse. The retardation is measured by an ellipsometer consisting of a quarter-wave plate ($\lambda/4$) and a Wollaston prism (PM). The prism distributes the horizontal and vertical wavelength contributions on two photodiodes and the respective intensities are measured via the induced photocurrent (I_{PD1} and I_{PD2}). By employing differential ($\Delta I_{\mathrm{PD}} = I_{\mathrm{PD1}} - I_{\mathrm{PD2}}$) lock-in (LI) technique, the momentary electric field is recorded as a function of the relative delay t_{EOS} between the gate and the multi-THz pulses. **b**, Electric field (black curve) and intensity envelope (gray area) of the multi-THz waveform detected by EOS with 10 fs temporal resolution, given by the gate pulse duration. **c**, Fourier transform of the multi-THz pulse in **b**. The absolute phase (red curve) and amplitude spectrum (black curve) are shown. The bandwidth-limited pulse duration in the time domain results in a flat spectral phase.

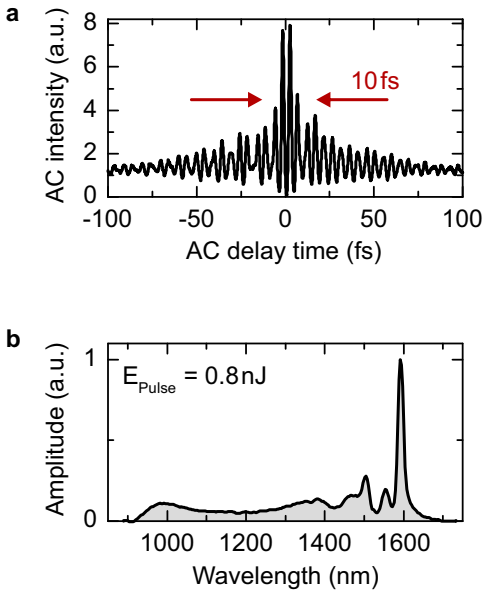

Figure 2.7 | Ultrashort gate pulses for electro-optic sampling. **a**, Interferometric, nonlinear autocorrelation trace of the gate pulses, custom-tailored from the output pulses from Amplifier III with the help of a NLF-HNLF hybrid fiber. As inferred from the autocorrelation trace, the dispersive part of the supercontinuum is re-compressed to a pulse duration below 10 fs using a prism compressor. **b**, Spectrum of the gate pulses spanning a wavelength range from 900 to 1700 nm, with a pulse energy of $E_{\mathrm{pulse}} = 0.8\,\mathrm{nJ}$.

prism. The prism distributes the horizontal and vertical polarization components equally on two photodiodes as long as no electric field is applied to the crystal. In contrast, field-induced birefringence causes an imbalance of the photocurrent of the photodiodes $\Delta I_{\mathrm{PD}} = I_{\mathrm{PD1}} - I_{\mathrm{PD2}}$. Using differential lock-in detection, ΔI_{PD} can be measured at the fundamental shot-noise limit of the gate pulses [Hub00, Por14b] and the retrieved signal is, to first approximation, linear with the applied electric field ($\Delta I_{\mathrm{PD}} \propto E_{\mathrm{THz}}$).

An example waveform measured by electro-optic sampling can be seen in Fig. 2.6b. The oscillation period of the electric field is approximately 28 fs corresponding to 2.7 oscillation cycles within the multi-THz pulse intensity envelope of 75 fs. The excellent signal-to-noise ratio of $10000 \cdot \sqrt{\mathrm{Hz}}$ stems from the high pulse energy of the multi-THz pulses and from the low background noise of $12\,\mathrm{nV}/\sqrt{\mathrm{Hz}}$ in the balanced detection, which is close to the fundamental shot-noise limit of the gate photon flux ($10\,\mathrm{nV}/\sqrt{\mathrm{Hz}}$). By Fourier transformation of the measured waveform, the absolute phase (Fig. 2.6c, red curve) and amplitude spectrum (black curve) can directly be extracted. The spectrum is centered at a frequency of 36 THz and is Gaussian shaped, while its phase features minimal dispersion, a consequence of the bandwidth-limited pulse duration in the time domain. In the example waveform in Fig. 2.6b, the carrier envelope phase offset between the oscillating electric field and the intensity envelope is $\Phi_{\mathrm{CE}} \approx 3\pi/2$. The temporal resolution of EOS is given by the bandwidth of the nonlinear detector crystal and is ultimately limited by the gate pulse duration.

The gate pulses are custom-tailored from the output pulses from Amplifier III ($f_{\mathrm{rep}} = 40\,\mathrm{MHz}$, $E_{\mathrm{pulse}} = 9\,\mathrm{nJ}$). Again nonlinear pulse propagation inside a custom-tailored

7.8-cm long NLF prechirp-fiber followed by 6 mm of HNLF is used. The dispersive part ($E_{\mathrm{pulse}} = 0.8\,\mathrm{nJ}$, $\lambda_{\mathrm{gate}} = 1300\,\mathrm{nm}$) of the generated supercontinuum is re-compressed to a pulse duration below 10 fs using a prism compressor [Sel09, Kra10], setting the ultimate temporal resolution achievable by EOS in our setup to 10 fs. An interferometric, nonlinear autocorrelation trace is shown in Fig. 2.7a, verifying the gate pulse duration, and the corresponding gate-pulse spectrum is shown in Fig. 2.7b.

2.3 Two-time terahertz spectroscopy

Measuring the dielectric response of systems driven to a non-equilibrium state by femtosecond photoexcitation is a key challenge in ultrafast science. Commonly, pump-probe experiments are employed, where a pump pulse prepares an excited state which is subsequently sampled by an ultrafast probe pulse. By tuning the relative arrival time (t_{pp}) between the pulses, the relaxation of the sample into the equilibrium state is monitored. Typically, conventional low-bandwidth photodiodes are used to measure the pump-induced change of the probe pulse. Due to their limited bandwidth, these photodetectors integrate over the intensity envelope of the probe pulse, which sets an intrinsic limit to the highest achievable temporal resolution. For systems evolving on timescales comparable to the probe-pulse duration a rigorous determination of the sample response is thus no longer attainable. In contrast, the combination of EOS with conventional pump-probe studies can be used to go beyond intensity-resolved measurements by performing two-time THz spectroscopy. This way the evolution of the complex-valued dielectric function following photoexcitation can be studied on sub-cycle timescales [Hub01, Něm05, Por14b, Eis14].

2.3.1 Sub-cycle time resolution in ultrafast pump-probe studies

An equilibrium system that is perturbed by an electromagnetic waveform features a time-dependent polarization response $P(t)$. The polarization response is determined by the convolution of the electric probe field $E(t')$ with the dielectric function $\epsilon(t-t')$ of the sample

$$P(t) = \epsilon_0 \int_{-\infty}^{t} E(t') \left(\epsilon(t-t') - 1\right) dt' \ . \tag{2.14}$$

Due to causality, the polarization response at a given time t therefore has to be calculated by integrating over all times prior to the time of observation. This situation is depicted in Fig. 2.8a for a delta-function-like probe pulse (red). At time t' the probe pulse excites a polarization response in the sample (gray dashed curve) that is subsequently measured by EOS using a delta-function-like gate pulse (green) at time t. If the probe field $E(t')$ is known exactly, it is sufficient to measure the polarization response $P(t)$ to calculate the

complex-valued dielectric function $\epsilon(t-t')$, without the need for Kramers-Kronig relations [Jep10, Ulb11]. Applying the convolution theorem the dielectric function in Fourier space can directly be extracted as follows

$$P(\omega) = \epsilon_0 \left(\epsilon(\omega) - 1\right) E(\omega) \ . \tag{2.15}$$

The situation becomes more complicated when the dielectric function of the system itself becomes time-dependent due to photoexcitation. The dielectric response of the photoexcited sample then not only depends on the external electric probe field $E(t')$, but also on its internal relaxation dynamics, which is shown in Fig. 2.8b. In addition to the probe pulse at time t', a pump pulse (blue) at time t'' is introduced. Hence, the one-time-dependent polarization response $P(t)$ has to be extended to also account for the pump-induced changes of the dielectric response while the polarization evolves. For a thorough analysis a two-time dielectric function $\epsilon(t-t', t-t'')$ is therefore used, which results in a polarization response $P(t, t'')$

$$P(t, t'') = \epsilon_0 \int_{-\infty}^{t} E(t') \left(\epsilon(t-t', t-t'') - 1\right) dt' \ . \tag{2.16}$$

In contrast to the equilibrium case (Equation 2.14), it is not possible to retrieve the dielectric function from Equation 2.16 by deconvolution in Fourier space since both arguments of $\epsilon(t-t', t-t'')$ explicitly depend on the time t. However, by measuring each point of the polarization response at the same pump-gate delay time $t_{\mathrm{pg}} = t - t''$, this problem can be solved [Kin99, Něm02]. Hence, an effective waveform of the polarization response is measured, where each point of the transient corresponds to a fixed age after photoexcitation. Experimentally, this is achieved by keeping the delay time between the pump and the electro-optic gate pulses fixed while scanning the multi-THz probe transient in time (see Section 2.3.2). The polarization response then reduces to

$$P(t, t - t_{\mathrm{pg}}) = \epsilon_0 \int_{-\infty}^{t} E(t') \left(\epsilon(t-t', t_{\mathrm{pg}}) - 1\right) dt' \ . \tag{2.17}$$

Applying the convolution theorem, the time-dependent dielectric function at a particular pump-gate delay time $\epsilon(\omega, t_{\mathrm{pg}})$ can be extracted. Note that the EOS delay time $t_{\mathrm{EOS}} = t - t'$ and pump-gate delay time t_{pg} are independent of each other. Hence, the highest achievable temporal resolution is two-time THz spectroscopy is ultimately given by the gate pulse duration [Kin99, Hub01].

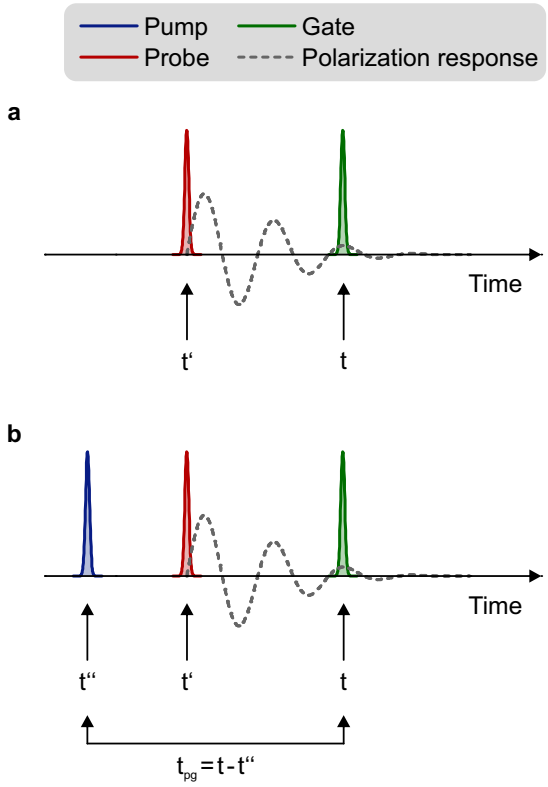

Figure 2.8 | Two-time THz spectroscopy. **a**, A delta-function-like probe pulse (red) at time t' induces a polarization response (gray dashed curve) in an unexcited dielectric medium. The polarization response is subsequently measured by EOS with the help of a delta-function-like gate pulse (green) at time t. By recording the complete polarization response $P(t)$ and the electric field of the probe pulse $E(t)$ by EOS, the full complex-valued dielectric function of the sample can be recovered. **b**, Non-equilibrium response of a dielectric medium excited by a delta-function-like pump pulse (blue) at time t'' which is probed by the probe pulse at time t'. The induced polarization response $P(t, t - t_{\mathrm{pg}})$ at the pump-gate delay time $t_{\mathrm{pg}} = t - t''$ is recorded by EOS using the gate pulse at time t.

2.3.2 Ultrafast spectroscopy

The pump pulses required to trigger femtosecond dynamics are generated by Amplifier IV ($f_{\mathrm{rep}} = 40\,\mathrm{MHz}$, $E_{\mathrm{pulse}} = 9\,\mathrm{nJ}$), which is seeded by a small fraction of the output pulse train of Amplifier III (see Fig. 2.1). Importantly, the seed pulses are picked off by a beam sampler after passing the EOS delay stage t_{EOS}. This way the time delay of the pump and gate pulses are intrinsically synchronized with respect to the multi-THz pulses, which is an essential prerequisite for two-time THz spectroscopy. An additional delay stage after Amplifier IV is used to adjust the relative delay between the pump and gate pulses (t_{pg}) or the pump and multi-THz probe pulses (t_{pp}), respectively. Thus, the setup can operate in two modes:

Intensity resolved pump-probe spectroscopy: Pump-probe measurements are performed by scanning the relative pump-probe delay time t_{pp} while the multi-THz probe pulse intensity is recorded using an intensity-resolved MCT photodiode. The highest achievable temporal resolution is limited by the probe pulse duration to $\geq 60\,\mathrm{fs}$. The zero delay time is defined by the temporal overlap of the maxima of the intensity envelopes from the multi-THz probe pulse and the pump pulse and can approximately be found by performing pump-probe scans on semiconductors at high excitation fluencies. This way an ultrafast sample response is triggered by the injection of an electron-hole plasma [Hub01]. Here, the zero delay time corresponds to half of the rise time of the pump-induced change of the measured signal. In addition, spectral information of the probe pulses as a function of t_{pp} can be retrieved by Fourier transform infrared spectroscopy (FTIR), which is detailed in Section 2.4.2.

Two-time THz spectroscopy: The pump-gate delay time t_{pg} is set constant while performing EOS (t_{EOS}). This way an effective waveform is recorded in which each point on the EOS time axis is measured at the same age after photoexcitation. By varying the pump-gate delay a full two-time multi-THz spectroscopy map is recorded, in which the pump-induced dynamics can be resolved with sub-cycle temporal resolution. The highest achievable temporal resolution is ultimately defined by the gate pulse duration (10 fs in the experiments shown here). Here, the zero time delay is defined by adjusting the gate pulse to the center of the multi-THz waveform and by finding the zero time delay using intensity resolved pump-probe measurements.

Two-time THz spectroscopy enables the direct measurement of the absolute phase and amplitude spectrum with sub-cycle temporal resolution as a function of pump-gate delay time. Thus, the time-dependent, complex-valued dielectric function of the sample can be extracted over a broad frequency range, only limited by the bandwidth of the detection process. Although spectral information can also be inferred using FTIR, only the relative phase of the probe pulses with respect to a reference pulses can be extracted with a time-resolution limited to the probe pulse duration, at best. Since FTIR is based on a linear cross-correlation, it solely detects frequency components that are also apparent in a reference waveform. In contrast to FTIR, EOS enables detection over a broad frequency range [Sch14].

Ultrafast excitation pulses in the near-infrared

Near-infrared pump pulses are custom-tailored by nonlinear pulse propagation in a 9-cm long NLF fiber. Solitonic pulse compression reduces the pulse length to below 22 fs, as is inferred from the nonlinear autocorrelation trace in Fig. 2.9a. The solitonic pulse propa-

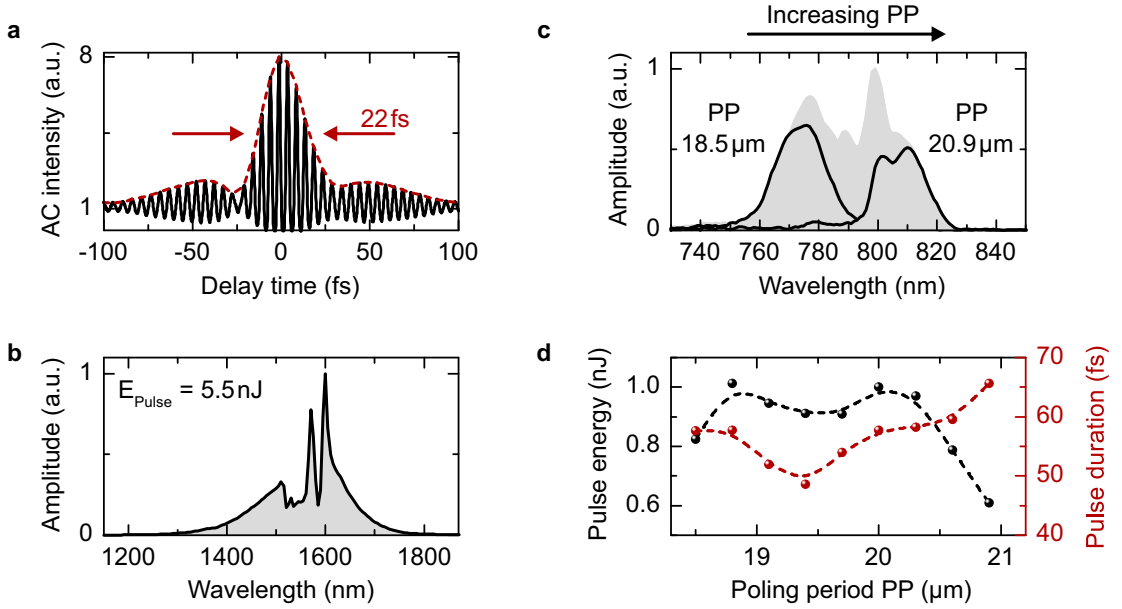

Figure 2.9 | Ultrashort pump pulses. **a**, Interferometric, nonlinear autocorrelation trace of the near-infrared pump pulses after nonlinear pulse propagation in a NLF. Solitonic pulse compression leads to a reduction of the pulse duration to 22 fs with a maximum pulse energy of $E_{\mathrm{pulse}} = 5.5\,\mathrm{nJ}$. **b**, Measured spectrum of the pump pulses. Due to self-phase modulation the spectrum is significantly broadened with a mean photon energy of $E_{\mathrm{photon}} = 0.78\,\mathrm{eV}$. **c**, Two measured spectra (black curves) of the frequency doubled pump pulses, which are generated in a periodically-poled lithium niobate crystal at a poling period (PP) of 18.5 µm and 20.9 µm. The accessible spectral range as a function of PP is indicated by the gray shaded area. The mean photon energy can be tuned in the range of $1.5 - 1.6\,\mathrm{eV}$. **d**, Pulse energy (black curve) and pulse duration (red curve) of the frequency-doubled pump pulses as a function of PP.

gation is also apparent in the photon intensity distribution, which displays a significantly broadened spectrum at both the high and low wavelength regions (see Fig. 2.9b). The pulses exiting the fiber feature a maximum pulse energy of $E_{\mathrm{pulse}} = 5.5\,\mathrm{nJ}$ and a mean photon energy of $E_{\mathrm{photon}} = 0.78\,\mathrm{eV}$.

Femtosecond excitation pulses in the visible

To increase the flexibility of the setup and to access a broader range of ultrafast processes in solids, the near-infrared excitation pulses are optionally frequency doubled in a 300-µm thick periodically-poled lithium niobate (PPLN) crystal. The PPLN allows for conversion efficiencies $> 20\,\%$ by quasi-phase-matching [Fei85, Arb97]. The orientation of the $\chi^{(2)}$ nonlinearity is periodically reversed to compensate for the effects of phase-velocity mismatch in the crystal. The generated second harmonic spectra are depicted in Fig. 2.9c as

a function of the poling period (PP). By changing the PP the phase-matching condition can be adjusted to tune the mean photon energy in the range of 1.5 to 1.6 eV. The duration of the visible excitation pulses ranges between 48 and 96 fs (red curve) with a pulse energy of 0.6 to 1.0 nJ (black curve), as can be seen in Fig. 2.9d.

2.4 Scattering-type near-field microscopy

Merging two-time THz spectroscopy with nanometer spatial resolution will open exciting new possibilities for studying the ultrafast dynamics of low-energy elementary excitations at the surface of single nanoparticles [Sti10, Jac12], nanodomains [Qaz07, Liu13] and single-layer materials [Fei12, Che12, Fei13, Dai14, Woe15, Doc14]. Currently, the spatial resolution of far-field THz spectroscopy is intrinsically limited to the scale of the probing wavelength by diffraction (3 µm − 3 mm) [Abb73]. Averaging over different sizes, orientations and densities of nanoparticles thus makes it impossible to gain a complete understanding of the impact of the nanostructures on the physical properties. To extract some nanoscale information, effective medium theories are employed to model the far-field response of such compound-systems [Jep06, Par07, Ulb11]. However, the fundamental diffraction limit only applies to far-field studies. Hence, accessing the optical near field overcomes this limitation and allows for a dramatically increased spatial resolution [Syn28]. With the invention of scattering-type near-field scanning optical microscopy (s-NSOM) [Zen94, Ino94, Kaw95, Nov98] sub-wavelength imaging became readily available and is used in this work to extend two-time multi-THz spectroscopy to the nanoscale, far beyond the fundamental diffraction limit.

The s-NSOM[7] microscope used throughout the experiment employs sharp silicon tips with platinum-iridium coating[8] as near-field probes. The use of such scattering-type probes has a significant advantage: Scattering from metal tips is intrinsically broadband with a spatial resolution only determined by the radius of curvature of the tip [Tau03a, Kei04]. The s-NSOM itself includes an atomic force microscope operating in tapping mode. The metal tip is attached to a cantilever that oscillates above the sample surface with a defined tapping amplitude (TA) and a tapping frequency Ω_{tip} that is slightly below the resonance frequency of the cantilever. To control the average distance between the tip and the sample a feedback loop is used which exploits the strong influence of the tip-sample interaction on the resonance frequency of the cantilever. For small tip-sample distances, Pauli blocking as well as Coulomb repulsion lead to an increase of the cantilever's resonance frequency, reducing the free space tapping amplitude $\text{TA}_{\text{free space}}$ to the experimental TA, while the

[7] NeaSNOM - 2nd generation, NeaSpec, 82152 Martinsried, Germany
[8] Arrow$^{\text{TM}}$ NCPT, NanoWorld, 2002 Neuchatel, Switzerland

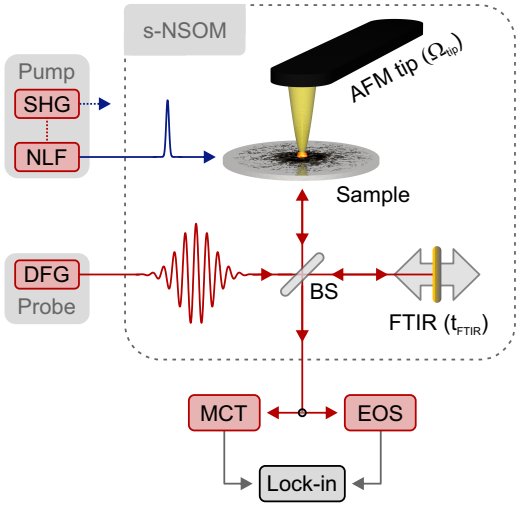

Figure 2.10 | The near-field microscope. Multi-THz probe pulses (red waveform) are sent into the s-NSOM, where they enter a Michelson-type interferometer, which splits the probe pulses in two arms using a silicon beam splitter (BS). The reflected part is focused onto the metal tip of an atomic force microscope (AFM), which oscillates with a tapping frequency Ω_{tip} above the sample. The scattered radiation is recorded by EOS or with a MCT photodiode. Lock-in detection of the measured signals at higher harmonics of Ω_{tip} allows for background-free detection. The second arm of the interferometer can optionally be used to perform nano Fourier transform infrared spectroscopy (nano-FTIR) by scanning the relative delay t_{FTIR} between the interferometer arms. Sample excitation is achieved by focusing the pump pulses (blue pulse) onto the sample below the tip.

tip is approached. The change in TA is measured by a laser that is deflected off the back of the cantilever and is used to define a setpoint ($\mathrm{TA}/\mathrm{TA}_{\mathrm{free\ space}} \approx 80\,\%$) to control the average tip-sample distance.

Optical implementation of the near-field microscope

The incorporation of the AFM into the optical setup to perform ultrafast near-field microscopy is displayed in Fig. 2.10. The multi-THz probe pulses (red waveform) are sent into the microscope, where they enter a Michelson-type interferometer that employs a silicon wafer as beam splitter. The reflected part is focused onto the AFM tip using a parabolic mirror with a numerical aperture of 0.56, leading to a diffraction-limited multi-THz spot size of approximately 10 µm. The scattered near-field radiation off the AFM tip is collected using the same parabolic mirror. After passing the silicon beam splitter, the scattered multi-THz pulses are detected either using the MCT photodiode (intensity resolved) or by performing EOS (field resolved). In the case of EOS, the pulses reflected off the interferometer arm (FTIR) serve as unmodulated reference pulses, which are simultaneously recorded with the scattered waveforms and are used to keep track of the slowly varying Φ_{CE} of the multi-THz radiation (see Section 2.2.1 and Appendix A). In addition, the interferometer and the MCT photodiode can be used to perform nano Fourier trans-

form infrared spectroscopy (nano-FTIR) of the scattered pulses by scanning the relative delay time t_{FTIR}. This is described in detail in Section 2.4.2. In order to perform ultrafast pump-probe studies the near-infrared or visible pump pulses (blue pulse) are focused onto the sample below the tip to a focal spot size of approximately 10 µm.

Background suppression by lock-in detection

One major challenge in s-NSOM is to eliminate unwanted background radiation from the cantilever or the sample surface, which commonly dominates the detected signals. The scattered near-field radiation originates from a mode volume of only $< (100\,\mathrm{nm})^3$, being by nature orders of magnitude lower in intensity than the diffuse reflected radiation. However, the near-field interaction itself provides the essential ingredient to successfully suppress the background radiation in the detection. A theoretical consideration of the near-field interaction can be seen in Fig. 2.11a. A metal tip, oscillating with a defined tapping amplitude (TA) at a tapping frequency Ω_{tip}, is placed close to a sample surface. When the electric field of a light pulse is focused onto the tip with a polarization parallel to the tip shaft, it induces a point dipole within the tip apex. By assuming, that the tip shaft does not strongly contribute to the observed near-field signal, the polarizability of the tip can be approximated by the polarizability of a sphere with a radius of curvature given by the tip apex [Kno00]. The tip dipole induces a surface charge distribution in the sample with a field that can be described by an image dipole. This image dipole in turn influences the electric field at the tip, leading to a coupling between the two dipoles, indicated by the red field lines in Fig. 2.11a. Hence, the presence of the sample significantly alters the near field at the tip and information about the optical properties of the sample are encoded in the light scattered off the tip. For a more detailed derivation of the applied model see Section 3.2.

The scattering efficiency of the coupled dipoles strongly depends on the distance between the tip and the sample. This can be seen in Fig. 2.11b, which features an exponential decay of the scattered intensity with increasing tip-sample distance. For a separation length of a few tip radii the scattered intensity becomes constant and originates from the uncoupled tip dipole. By operating the tip in tapping mode the tip-sample distance is periodically modulated and thereby the scattered near-field intensity, as indicated by the blue dashed curve in Fig. 2.11b. Due to the nonlinear dependence of the scattered radiation on the tip-sample distance, the harmonic motion of the tip translates into an anharmonic scattering response in time, as shown by the blue curve in the inset. In Fourier space the anharmonic response generates non-zero frequency sidebands at the harmonics n of the tip-tapping frequency ($n \cdot \Omega_{\mathrm{tip}}$, with $n = 1, 2, 3, \dots$), which can be

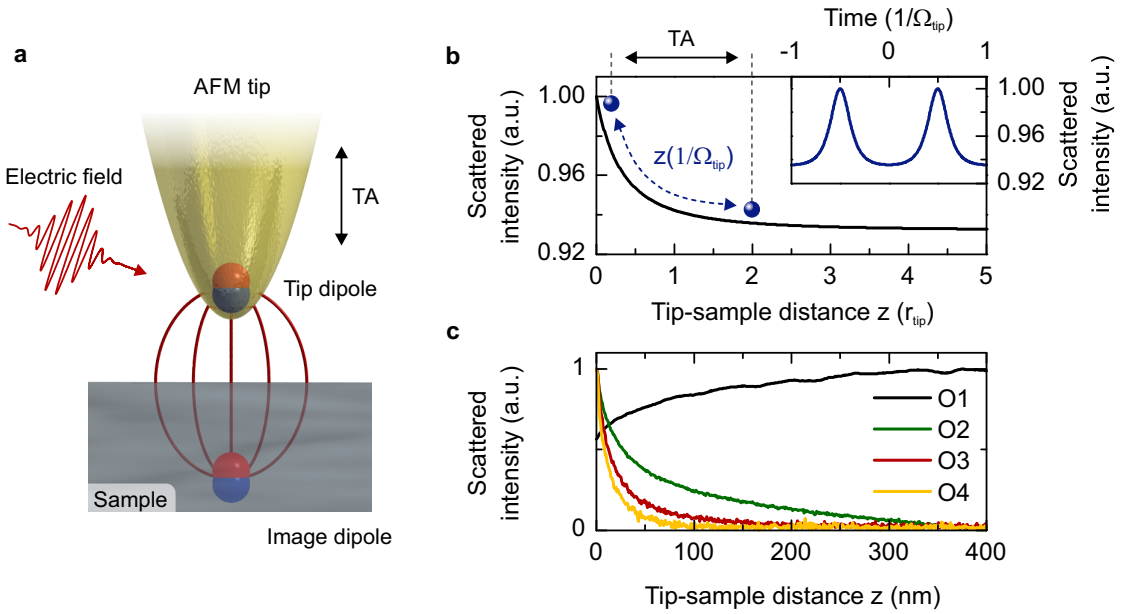

Figure 2.11 | Background suppression by lock-in detection. **a**, Illustration of the tip-sample interaction in s-NSOM. A metal tip, oscillating with a frequency Ω_{tip} and a tapping amplitude (TA), is brought close to a sample surface. The electric field of an incoming light pulse, polarized parallel to the tip shaft, induces a point dipole in the tip. Due to surface charge redistribution an image dipole forms in the sample, modifying the electric field at the tip dipole. This effect leads to a coupling between the dipoles, indicated by the red field lines, that effectively describes the near-field interaction. **b**, Scattered intensity of the coupled dipoles as a function of tip-sample distance (black curve). With increasing distance the intensity decays exponentially towards a constant background, originating from scattering off the uncoupled tip. By operating the tip in tapping mode the scattered intensity is periodically modulated, as indicated by the blue dashed curve. The harmonic motion of the tip directly translates into an anharmonic modulation of the scattered intensity in time (inset, blue curve). Lock-in detection of the scattered radiation at higher harmonics of Ω_{tip} efficiently reduces all background contributions in the detection scheme. **c**, Scattered intensity as a function of tip-sample distance measured on a gold sample at various harmonics of the tapping frequency using the near-field microscope. The signals are recorded with the help of a MCT photodiode and processed by lock-in detection. The first harmonic O1 ($1 \cdot \Omega_{\mathrm{tip}}$, black curve) and the second harmonic O2 (green curve) are still affected by unwanted background radiation from the tip shaft and cantilever. O3 (red curve) and O4 (yellow curve) both feature a clear indication of a pure near-field signal: an exponential decay of the measured signal within approximately 30 nm tip-sample distance. In this measurements the tapping amplitude is set to TA = 130 nm.

filtered using a lock-in approach [Lab00, Kno00]. The achievable background suppression can directly be seen in the experimentally obtained retraction curves measured with the near-field microscope. Here, the scattered near-field intensity is recorded using the MCT photodiode. Fig. 2.11c shows the scattered intensity of various harmonics as a function of the average tip-sample distance. The retraction scan measured at the first demodulation order ($O1 = 1 \cdot \Omega_{tip}$, black curve) does not feature a clear dependence of the scattered signal on the relative distance. Importantly, O1 does not vanish for distances larger than 100 nm, indicating that diffuse scattering off the tip cantilever, which is also modulated at Ω_{tip}, still dominates the measured response. With increasing harmonic order ($O2 - O4$), the near-field contribution becomes clearly visible, leading to an exponential decay of the measured signals with increasing tip-sample distance. Yet, for large tapping amplitudes and small average distances between the tip and the sample, the mechanical motion of the tip itself can become anharmonic. This leads to an additional background for lower demodulation orders, as can be seen in the retraction scan of O2 (green curve). By increasing the demodulation order the anharmonic background can successfully be reduced, resulting in a pure near-field signal in O3 (red curve) and O4 (yellow curve). Hence, the scattered intensity drops exponentially within 30-nm distance between the tip and the sample.

2.4.1 Field-resolved detection with sub-cycle temporal resolution

In the few-THz region ($0.1 - 3$ THz), THz spectroscopy has successfully been employed to detect the scattered radiation of near-field probes with 55 µm spatial resolution in a-NSOM [Hun98] and $\geq$ 150 nm spatial resolution in s-NSOM [Che03, Che04, Zha07, Rib08, Moo12]. While achieving a spatial resolution well below the diffraction limit, none of these studies, however, has probed photoinduced dynamics. Conversely, intensity-resolved detection in the mid-infrared using MCT photodiodes has been employed to investigate the electron dynamics of photoexcited graphene sheets [Wag14a] and bulk semiconductors [Wag14b] in the near field of metal tips. Due to the intensity detection, the observed temporal resolution of $\geq$ 200 fs is thereby intrinsically limited to the probe pulse duration, at best. However, the temporal resolution can be dramatically increased by directly observing the pump-induced change of the oscillating electric near field.

In this work two-time multi-THz spectroscopy is for the first time extended to the nanoscale by measuring the scattered radiation off the near-field tip by EOS. This technological achievement builds the basis to study ultrafast phenomena at the surface of solid-state system with both high spatial and sub-cycle temporal resolution [Eis14] (see Chapter 3 and 4).

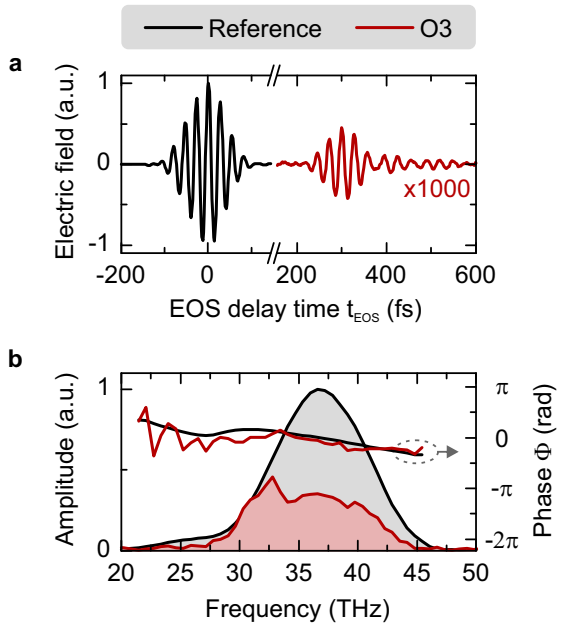

Figure 2.12 | Field-resolved detection of the oscillating electric near field. **a**, Reference waveform (black curve) reflected off the FTIR delay line measured at a lock-in frequency of $f_{\mathrm{EOM}} = 20\,\mathrm{MHz}$ and near-field waveform scattered off a gold sample (red curve, $\times 1000$ magnification factor), measured at the third order sideband $f_{\mathrm{EOM,O3}} = 20\,\mathrm{MHz} + 3 \cdot \Omega_{\mathrm{tip}}$. Ultrasensitive detection is a prerequisite, as the near-field signal corresponds to less than 1000 photons. **b**, Absolute phase (solid curves) and amplitude spectrum (colored areas) of the reference pulse (black) and the scattered pulse (red). The near-field interaction can significantly distort the scattered spectrum in comparison to the reference spectrum, which exhibits a center frequency of 36.6 THz with a bandwidth of 10 THz. The absolute, scattered phase closely follows the reference phase, varying by less than π over the entire frequency spectrum ($25 - 45\,\mathrm{THz}$).

A typical waveform retrieved over a gold sample can be seen in Fig. 2.12a (red curve, $\times 1000$ magnification factor). Here, the pulses reflected off the FTIR delay line serve as reference pulses (black curve). Ultrasensitive lock-in detection is an indispensable prerequisite to measure these scattered waveforms electro-optically, since the near-field signal recorded at the third order harmonic of Ω_{tip} corresponds on average to less than 1000 photons per pulse. Here, the reference waveform is measured at a lock-in frequency of $f_{\mathrm{EOM}} = 20\,\mathrm{MHz}$ and the third-order near-field signal is recorded at the third sideband $f_{\mathrm{EOM,O3}} = 20\,\mathrm{MHz} + 3 \cdot \Omega_{\mathrm{tip}}$. The advantage of field-resolved detection and two-time THz spectroscopy in comparison to intensity-resolved detection schemes can directly be seen by comparing the scattered field transient to the reference waveform. While the latter is close to bandwidth limited, exhibiting a Gaussian field envelope, the pulses scattered off the near-field tip feature trailing oscillations, stretching the pulse in time. Since the sample response of a metal in the mid-infrared wavelength region can be assumed to be spectrally flat, these oscillations result from antenna resonances of the tip itself. In intensity-resolved pump-probe measurements the temporal resolution is directly proportional to the intensity envelope of the multi-THz pulses. Hence, the dependence of the scattered probe-pulse duration on the exact shape of the tip can result in a significant, tip-dependent reduction of the temporal resolution. This drawback can become even more pronounced when

narrow-band resonances within the sample itself additionally elongate the probe pulses in time. Two-time THz spectroscopy resolves this shortcoming using field-resolved detection, which is limited in its temporal resolution only by the duration of the gate pulses (10 fs).

Field-resolved detection provides access to both the absolute phase and amplitude spectrum of the scattered radiation via Fourier transformation, as depicted in Fig. 2.12b. Hence, the local complex-valued dielectric function of a sample can be retrieved from the scattered signals with nanometer spatial resolution and 10 fs temporal resolution. The scattered spectrum (red shaded area, $\times 1000$ magnification factor) with a center frequency of 35 THz is distorted due to the tip resonance as can be seen by comparison to the Gaussian shaped reference spectrum (black shaded area) that features a center frequency of 36.6 THz with a bandwidth of 10 THz. In particular, the frequency components above 33 THz seem to scatter less efficiently. However, the absolute phase (red curve) follows closely along the flat phase of the reference pulse (black curve), varying by less than π over the entire spectral range from 25 to 45 THz. The carrier envelope phase offset of approximately 0 rad can also be observed in the relative position of the electric field to the field envelope in the time-domain images in Fig. 2.12a.

2.4.2 Nano Fourier transform infrared spectroscopy

An alternative approach to obtain spectral information is phase-resolved Fourier transform infrared spectroscopy (FTIR) [Gen75], which is based on a Michelson-type interferometer. In conventional phase-resolved FTIR, the incoming radiation is divided into a signal and a reference arm. The pulses are reflected off two end mirrors and are again overlapped and detected using a MCT photodiode. By scanning the relative delay time between the signal and the reference arm the following linear cross-correlation pattern is recorded

$$\begin{aligned} I(\omega, t_{\mathrm{FTIR}}) &= |E_{\mathrm{sig}}(\omega) + E_{\mathrm{ref}}(\omega, t_{\mathrm{FTIR}})|^2 \\ &= |E_{\mathrm{sig}}(\omega)|^2 + |E_{\mathrm{ref}}(\omega)|^2 + |E_{\mathrm{sig}}(\omega)| \cdot |E_{\mathrm{ref}}(\omega)| \cdot \cos(\phi + \omega t_{\mathrm{FTIR}}) \ . \end{aligned} \tag{2.18}$$

$|E_{\mathrm{sig}}(\omega)|^2$ and $|E_{\mathrm{ref}}(\omega)|^2$ correspond to the laser intensity in the signal and the reference arms, respectively, and give rise to a constant background on the photodiode. The interference term on the right, however, causes a modulation of the background which directly depends on the frequency ω of the laser radiation, the field amplitudes $|E_{\mathrm{sig}}(\omega)|^2$ and $|E_{\mathrm{ref}}(\omega)|^2$, and the relative delay time t_{FTIR}. Hence, Fourier transformation of the recorded interference pattern directly results in a convoluted frequency spectrum that is proportional to $|E_{\mathrm{sig}}(\omega)| \cdot |E_{\mathrm{ref}}(\omega)|$ and to the relative phase ϕ between the interferometer arms [Bir87]. Since FTIR is based on linear cross-correlation, this technique can be

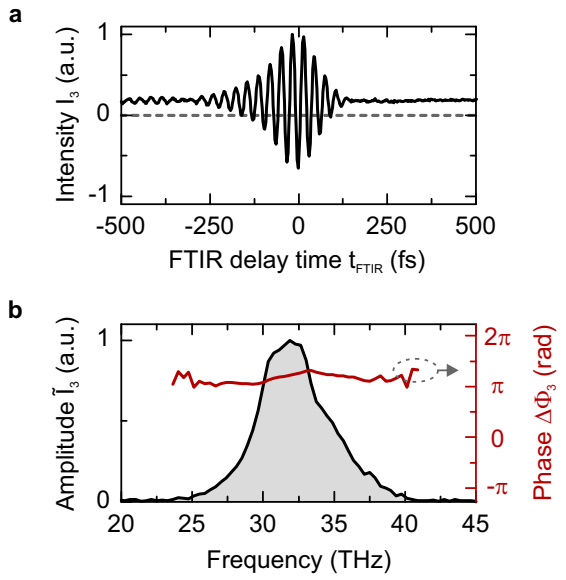

Figure 2.13 | Nano Fourier transform infrared spectroscopy. **a**, Linear cross-correlation of multi-THz pulses scattered off a gold sample. The interferogram is measured at the third demodulation order as a function of the relative delay time t_{FTIR} between the scattered and the reference pulses. The signal features an offset which directly relates to the scattered intensity E_3. In addition a periodic modulation of the base line with a oscillation period of 32 THz is observed in the proximity of the time overlap ($t_{\mathrm{FTIR}} = 0$). **b**, Fourier transformation of interferogram in **a**. The convoluted frequency spectrum (gray shaded area) and the relative phase (red curve) between the reference arm and the scattered signal can be retrieved with a spectral resolution of 0.2 THz.

directly extended to broadband laser sources. Here, the interference pattern is obtained by integrating over all frequency components

$$I(t_{\mathrm{FTIR}}) = \int_0^\infty d\omega \Big(|E_{\mathrm{sig}}(\omega)|^2 + |E_{\mathrm{ref}}(\omega)|^2 + |E_{\mathrm{sig}}(\omega)| \cdot |E_{\mathrm{ref}}(\omega)| \cdot \cos(\phi + \omega t_{\mathrm{FTIR}}) \Big) \, . \tag{2.19}$$

By replacing the end mirror of the signal arm with the s-NSOM tip (see Fig. 2.10), spectral information from the near field can be retrieved by performing nano-FTIR [Hut11, Gov13, Ame13, Wes14]. In addition, the combination of nano-FTIR with pump-probe spectroscopy enables the observation of the spectral evolution of the scattered near field with a temporal resolution given by the probe-pulse duration [Wag14a, Wag14b, Eis14]. The corresponding intensity detected at the nth demodulation order reads

$$I_n(t_{\mathrm{FTIR}}) = \int_0^\infty d\omega \, \Big(|E_n(\omega)|^2 + |E_n(\omega)| \, |E_{\mathrm{ref}}(\omega)| \cdot \cos(\phi_n + \omega t_{\mathrm{FTIR}}) \Big) \, . \tag{2.20}$$

Since lock-in detection is involved, the extraction of the scattered electric field E_n is more challenging and will be discussed in detail in Section 3.2.

A typical interference pattern of multi-THz pulses scattered off a gold sample and measured at the third demodulation order is depicted in Fig. 2.13a. The interferogram features an average intensity offset of 0.2 that corresponds to the scattered intensity $|E_3(\omega)|^2$. Due to the bandwidth $\Delta\nu$ of the multi-THz pulses, the coherence time is accordingly re-

duced to $T_{\mathrm{coh}} \propto 1/\Delta\nu$. Hence, interference is only expected in an interval of $[-T_{\mathrm{coh}}/2, T_{\mathrm{coh}}/2]$ around the temporal overlap between the reference pulse and the scattered signal (t_{FTIR}=0). There, a modulation of the baseline with an oscillation frequency of 32 THz is visible. Interestingly, the peak intensity of the interferogram is a factor of 5 higher than the baseline. This effect is regarded as heterodyne amplification [Kei04], whereby the electric field from the reference arm enhances the measured intensity I_3 via the interference term $|E_3(\omega)| \cdot |E_{\mathrm{ref}}(\omega)|$. The calculated spectrum can be seen in Fig. 2.13b (gray shaded area) with a center frequency of 32 THz and a bandwidth of 6 THz. In this experiment the highest spectral resolution of 0.2 THz is determined by the maximum delay time of the FTIR stage. The relative phase (red curve) between the reference and the scattered signal features a constant offset of π with only minimal dispersion.

Although, nano-FTIR is a well established method it is only capable of measuring the linear sample response. Interference, by definition, appears if both interfering arms possess the required frequency components. In contrast to EOS, nano-FTIR is therefore not capable to spectrally resolve nonlinear processes that introduce new frequency components outside the initial probe spectrum, for instance due to field-enhancement at the tip apex [Hut13, Wim14].

Chapter 3

Local carrier dynamics at the surface of a single indium arsenide nanowire

The development of semiconductor devices has laid the foundation for a plethora of technological achievements, ranging from computer chips to light emitting diodes. The desire to increase their operation speed and reduce their physical dimensions has spurred enormous development of nanometer-scale fabrication methods and novel materials. Nanoscale systems like quantum dots [Jac12, Coc13], single layer materials [Nov04, Che14, Doc14] and nanowires [Yan09, Joy13, Sax13, May13] have the potential to provide new building blocks for next-generation electronic and optoelectronic devices [Ulb11, Gei13]. For small particles, quantization effects, surface states and defects start to become increasingly important, altering the general physical properties known from bulk studies. However, the performance of novel nanostructure-based devices relies on a detailed knowledge of local femtosecond carrier dynamics and surface charge distributions, which calls for new characterization methods with unprecedented temporal and spatial resolutions.

For the first time ultrafast multi-THz spectroscopy in combination with scattering-type near-field scanning optical microscopy is used to investigate the local carrier dynamics at the surface of indium arsenide (InAs). This semiconductor serves as a model system to investigate the capabilities of our novel microscope. It features a direct band gap of $E_{\mathrm{gap}} = 0.35\,\mathrm{eV}$, a high mobility of $> 3000\,\mathrm{cm}^2/\mathrm{Vs}$ at room temperature and an effective electron mass of $m^* = 0.023 \cdot m_0$. Owing to the comparably small effective mass, the resulting plasma frequency $\omega_{\mathrm{p}} = \sqrt{\frac{N_{\mathrm{c}} e^2}{m^* \epsilon_0 \epsilon_\infty}}$ can be tuned readily within the multi-THz wavelength region by changing the carrier density N_{c}. Hence, ultrafast photoexcitation of free carriers is expected to strongly influence the optical properties of the sample. In addition to its technologically relevant properties, a vast sample catalog can be produced

from InAs that allows to tune the sample dimension from bulk crystals to nanowires down to single quantum dots.

Starting with bulk InAs measurements (**Section 3.1**), this chapter introduces the relevant physical quantities observable by ultrafast nano-spectroscopy. A detailed theoretical description of the scattered near field (**Section 3.2**) provides the means to extract the complex-valued dielectric function and the carrier density of the photoexcited bulk crystal as a function of pump-probe delay time (**Section 3.3**). Finally, by performing two-time multi-THz nano-spectroscopy on a single InAs nanowire (**Section 3.4**), the full potential of the microscope is used to directly visualize the ultrafast build-up of a surface depletion layer (**Section 3.5**). Our novel technique provides detailed insights into surface effects, recombination dynamics and the role of carrier doping while also setting the stage for future sub-cycle near-field experiments in a wide range of nanosystems.

3.1 Ultrafast nano-spectroscopy of bulk indium arsenide

Ultrafast nano-spectroscopy of bulk indium arsenide is performed on a single crystalline (100) InAs sample with an intrinsic background doping of $N_{\mathrm{int}} = 3 \cdot 10^{16}\,\mathrm{cm}^{-3}$. Importantly, the sample does not feature any spatial inhomogeneities, enabling the analysis of the sample response upon photoexcitation in a well defined environment. A schematic of the pump-probe geometry can be seen in Fig. 3.1a. The 22-fs near-infrared pump pulses (black), which are perpendicularly polarized with respect to the tip shaft, are focused onto the InAs sample below the AFM tip to a spot size of 10 µm. Upon photoexcitation, free carriers with an excess energy of approximately 0.4 eV are injected into the conduction band. Multi-THz pulses (red, polarized parallel to the tip shaft) with a center frequency of 33 THz are then scattered off the AFM tip to probe the sample response at a defined pump-probe delay time t_{pp} after photoexcitation. The scattered near-field intensity I_3 as a function of t_{pp} can be seen in Fig. 3.1b, where I_3 is normalized to the unpumped value (gray dashed line). The tapping amplitude of the tip is set to 130 nm and the near-infrared pump fluence is $1.1\,\mathrm{mJ/cm}^2$. Starting at negative delay times ($t_{\mathrm{pp}} = -1.5\,\mathrm{ps}$), the scattered intensity decreases, reaching a minimum at $t_{\mathrm{pp}} = -250\,\mathrm{fs}$, at which point I_3 is reduced to a value of 0.4. Within the next 400 fs the scattered intensity increases to a maximum value of approximately 2.2, which is followed by a decay towards a minimum value of 0.15 at $t_{\mathrm{pp}} = 6.3\,\mathrm{ps}$. In the next 100 ps, I_3 slowly recovers to the unpumped value. The initial decrease of the scattered signal is assigned to a 730-fs long pedestal pulse superimposed on the 22-fs pump pulse emerging from the NLF fiber[1]. Thus, the carrier

[1] The 730-fs long pulse can also be seen in the nonlinear autocorrelation in Fig. 2.9a, leading to the pronounced pedestal in the interference trace.

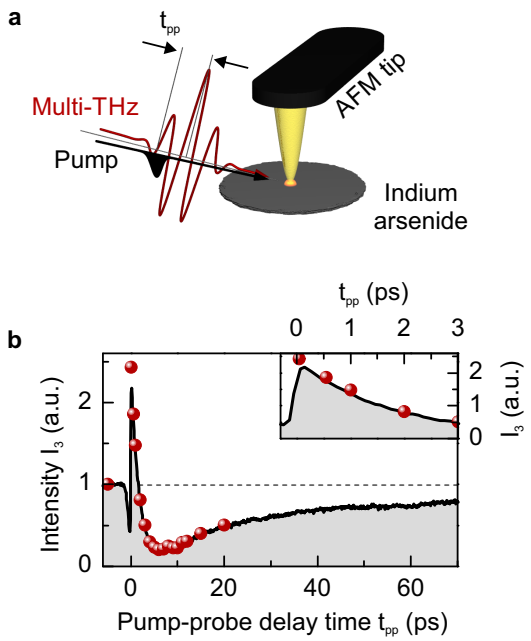

Figure 3.1 | Pump-probe near-field microscopy. **a**, Illustration of pump-probe near-field microscopy on bulk InAs. Near-infrared pump pulses (black, polarized perpendicular to the tip) with a pulse duration of 22 fs are focused to a spot size of 10 µm onto the sample below the tip. Hence, the electrons in the InAs crystal are promoted from the valence into the conduction band. The multi-THz pulses (red, polarized parallel to the tip) subsequently probe the effects of carrier injection as a function of pump-probe delay time t_{pp}. **b**, Scattered intensity I_3 as a function of t_{pp} measured on bulk (100) InAs. I_3 is normalized to the unpumped value, which is indicated by the gray dashed line. The inset is a zoom-in on the pump-probe trace at early times after photoinjection. The red dots correspond to the integrated intensities extracted from the nano-FTIR measurements shown in Fig. 3.3a. The tip-tapping amplitude is 130 nm and the pump fluence is 1.1 mJ/cm^2.

concentration in the conduction band increases prior to the full time-overlap between the 22-fs pump and the multi-THz probe pulses. In contrast, the sharp increase ($t_{\mathrm{pp}} \approx 0$ fs) stems from the 22-fs short part of the pump pulse.

From the pump-probe trace it is directly visible that the near-field signal strongly depends on the photoinjected carrier density. However, the direct relationship between carrier density and scattered intensity is non-trivial. Therefore, nano-FTIR is employed to investigate the impact of the photoexcited carriers on the spectrum of the scattered radiation. A reference amplitude spectrum $\tilde{I}_3$ measured on the unexcited bulk InAs sample can be seen in Fig. 3.2 (gray shaded area) with a frequency maximum at 32.5 THz and a relative phase ($\Delta\Phi_3$, red curve) between the scattered and the reference pulses, featuring minimal dispersion. Upon photoexcitation ($t_{\mathrm{pp}} = 50$ fs, see Fig. 3.3a), the scattering response of the low-frequency components is significantly enhanced, leading to a red-shifted center frequency of 31 THz accompanied by an increase of the peak intensity by a factor of 1.8 with respect to the reference spectrum. For $t_{\mathrm{pp}} > 50$ fs, the enhancement starts to decrease and a local minimum forms (resonance position ν_0) at the high-frequency edge of the spectrum which shifts to lower frequencies with increasing t_{pp} (blue dots). Interestingly, the spectral response is thereby only enhanced for frequency components below

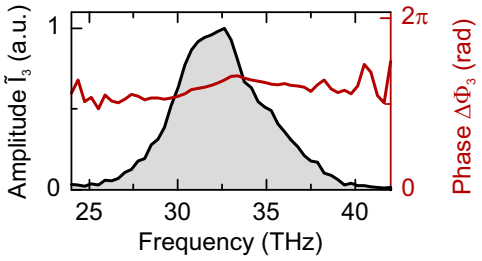

Figure 3.2 | Spectrum scattered off bulk indium arsenide. Amplitude spectrum $\tilde{I}_3$ (gray shaded area) and relative phase $\Delta\Phi_3$ (red curve) measured on an unexcited bulk (100) InAs wafer with an intrinsic carrier density of $N_{\text{int}} = 3 \cdot 10^{16}\,\text{cm}^{-3}$. The tip-tapping amplitude is 130 nm.

the resonance position. At $t_{\text{pp}} = 6\,\text{ps}$, the resonance position is centered at approximately 30 THz, leading to the lowest intensity I_3 of the integrated spectrum. As the resonance position shifts towards lower frequencies, $\tilde{I}_3$ recovers its unpumped shape ($t_{\text{pp}} > 12\,\text{ps}$). The integrated square of the measured spectra is proportional to the scattered intensity and quantitatively correlates with the pump-probe trace, as can be seen by the red dots superimposed on $I_3(t_{\text{pp}})$ in Fig. 3.1b. Hence, the position of the resonance frequency with respect to the multi-THz spectrum determines whether the integrated scattered intensity $I_3(t_{\text{pp}})$ is enhanced or reduced compared to the unpumped value.

The effects of carrier injection can also be seen in the relative phase $\Delta\Phi_3$ extracted from the nano-FTIR measurements (Fig. 3.3b). At the position of the resonance frequency ν_0 in Fig. 3.3a, $\Delta\Phi_3$ changes by 2 to 3 rad over a frequency interval of approximately 4 THz. With evolving t_{pp} the resonance width in the amplitude spectrum reduces and the slope of the phase-change significantly steepens, which could be a first indication for a carrier-cooling process of the hot electrons in the conduction band. The cooling process reduces the electron-electron and electron-phonon scattering rate, leading to a lower damping and thereby a smaller linewidth of possible electron resonances in the system.

In Fig. 3.3c, the resonance positions ν_0, extracted from Fig. 3.3a, are shown as a function of t_{pp} on a semi-logarithmic scale. Starting at a frequency of 36 THz ($t_{\text{pp}} = 550\,\text{fs}$), the resonance position decays to a frequency of 27 THz at $t_{\text{pp}} = 12\,\text{ps}$. In addition, a clear change of the exponential decay is visible at $t_{\text{pp}} \approx 3\,\text{ps}$, pointing towards different decay dynamics of the photoexcited electrons.

These first pump-probe experiments performed on bulk InAs already highlight the potential of our novel microscope to observe ultrafast dynamics in the mid-infrared with a spatial resolution far better than the diffraction limit. However, to extract physical quantities and to understand the origin of the resonance position and its dynamics, a theoretical description of the sample response is pivotal.

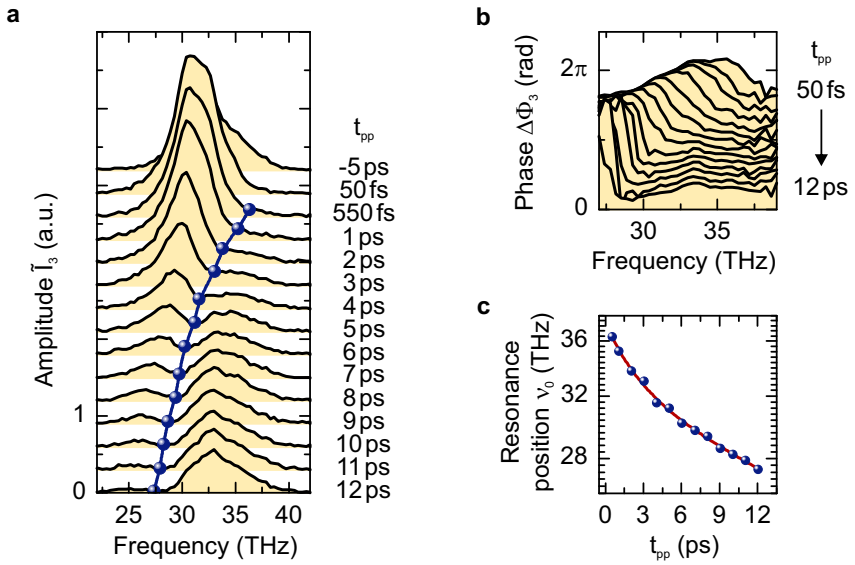

Figure 3.3 | Pump-probe nano Fourier transform infrared spectroscopy on bulk indium arsenide. **a**, Scattered amplitude spectrum $\tilde{I}_3$ as a function of pump-probe delay time t_{pp}. Upon photoexcitation ($t_{pp} = 50\,\text{fs}$) a significant increase of the peak intensity is observed. For $t_{pp} > 550\,\text{fs}$ a local minimum forms (resonance position ν_0) at the high-frequency edge of the spectrum, subsequently red-shifting through $\tilde{I}_3$ within 12 ps (blue dots). **b**, Relative phase extracted from the nano-FTIR measurements. The resonance position ν_0 in **a** is accompanied by a change of $\Delta\Phi_3$ on the order of 2 to 3 rad. **c**, Resonance position ν_0 as a function of pump-probe delay time t_{pp}, plotted on a semi-logarithmic scale. A bi-exponential decay is observed, as indicated by the change of the slope at $t_{pp} \approx 3\,\text{ps}$. All measurements are performed with a tip-tapping amplitude of 130 nm and a pump fluence of $1.1\,\text{mJ/cm}^2$.

3.2 Theory of scattering-type near-field microscopy

The theoretical derivation of the near-field interaction in scattering-type near-field scanning optical microscopy is an important prerequisite to understand the dependence of the scattered radiation on the dielectric properties of the sample. Several analytical approaches have been considered to quantitatively simulate the scattered near-field response. The calculations mainly differ in their modeling of the shape of the AFM tip. In the straightforward, point-dipole model, which is often sufficient, the AFM tip is represented as a sphere with a radius given by the tip radius of curvature [Zen95, Kno99, Kno00, Ras03, Kei04]. However, this model does not always provide a quantitative description of the observed near-field contrasts. Hence, it has been extended to the finite-dipole model, which incorporates the finite size of the tip shaft and its influence on the near-field interaction through additional fit parameters [Cvi07, Aiz08, Gov13].

In this work, both theoretical approaches have been used to simulate the observed carrier dynamics in the photoexcited InAs samples and the two models have produced similar results. The following theoretical derivation will therefore focus on the point-dipole model since an excellent agreement between theory and experiment is achieved using only the dielectric function of the sample as a free parameter.

3.2.1 The point-dipole model

The underlying theoretical considerations of the quasi-static point-dipole model are depicted in Fig. 3.4. Here, the AFM tip is simplified to a sphere [Kno00], which allows for an analytical solution of the model describing the near-field interaction. By applying an external electric field E_{in}, the charges on the surface of the tip redistribute, leading to an effective polarization of the sphere

$$p_{\mathrm{tip}} = \alpha_0 \cdot E_{\mathrm{in}} \ , \tag{3.1}$$

where the polarizability is given by

$$\alpha_0 = 4\pi\epsilon_0 a^3 \cdot \frac{\epsilon_{\mathrm{tip}} - 1}{\epsilon_{\mathrm{tip}} + 2} \ . \tag{3.2}$$

Here, ϵ_0 is the permittivity of free space and $a \approx 10-20\,\mathrm{nm}$ is the radius of curvature of the AFM tip. Importantly, α_0 depends on the dielectric function of the tip material ϵ_{tip}. Since metallic tips (metal coating thickness approximately 20 nm) are employed throughout the experiments, ϵ_{tip} is approximated by the Drude model based on the mid-infrared literature values of gold [Rak98].

The AFM tip is placed above a dielectric sample surface that spans the infinite half volume below the tip. The distance from the tip dipole to the sample surface r is thereby given by the sum of the minimum tip-sample distance z and the tip radius of curvature a. The electric field of the tip dipole

$$E_{\mathrm{tip}}(r) = \frac{p_{\mathrm{tip}}}{2\pi\epsilon_0 r^3} \tag{3.3}$$

induces surface charges in the sample, whose field can effectively be described by an image dipole located at a distance of $2r$ below the tip dipole in the dielectric medium. The polarization of the image dipole is given by

$$p_{\mathrm{image}} = \beta \cdot p_{\mathrm{tip}} \ , \tag{3.4}$$

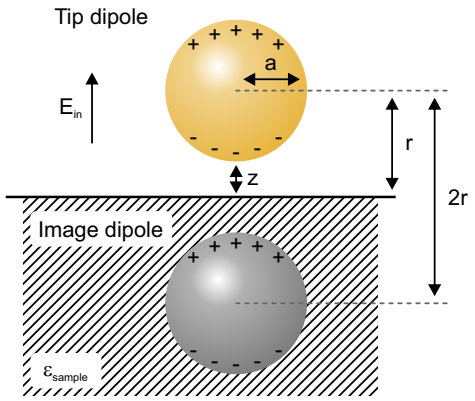

Figure 3.4 | The point-dipole model. Within the point-dipole model the metallic AFM tip is simplified to a sphere. The sphere is positioned over a sample surface with a dielectric function ϵ_{sample} at a distance $r = a+z$, given by the minimum tip-sample distance z and the radius of the sphere a. By applying an external electric field E_{in}, the sphere is polarized, leading to the formation of a tip dipole. The electric field of the tip dipole induces surface charges in the sample, which can be described by an image dipole located at a distance of $2r$ below the tip dipole. The coupling between the dipoles results in a new effective polarization of the tip-sample system, describing the near-field interaction.

with the electrostatic reflection coefficient

$$\beta = \frac{\epsilon_{\text{sample}} - 1}{\epsilon_{\text{sample}} + 1} \,. \tag{3.5}$$

The reflection coefficient β depends on the dielectric function of the sample ϵ_{sample} and originates from the continuity conditions of the electric field across the air-sample interface. The electric field of the image dipole can be written as

$$E_{\text{image}}(r) = \frac{p_{\text{image}}}{2\pi\epsilon_0 r^3} \,. \tag{3.6}$$

In the quasi-static limit, the field from the image dipole acts back on the tip dipole such that the total field affecting the tip is a combination of the external driving field and the field from the image dipole. This assumption is tenable as long as retardation effects between the dipoles can be neglected. With an optical path length between the dipoles of only a few 100 nm, the retardation times are on the few femtosecond timescale. In the mid-infrared wavelength region, the quasi-static approach can therefore be applied since the retardation times are much shorter than the oscillation period of the multi-THz radiation.

The polarization of the tip can then be written as follows, where the total field at the tip consists of the input field E_{in} and the field from the image dipole $E_{\text{image}}(2r)$

$$\begin{aligned} p_{\text{tip}} &= \alpha_0 \cdot \Big(E_{\text{in}} + E_{\text{image}}(2r) \Big) \\ &= \alpha_0 \cdot \left(E_{\text{in}} + \frac{\beta \cdot p_{\text{tip}}}{2\pi\epsilon_0 (2r)^3} \right) \ . \end{aligned} \tag{3.7}$$

Solving Equation 3.7 for p_{tip} yields a new expression for the quasi-static polarization of the tip dipole

$$\begin{aligned} p_{\text{tip}} &= \frac{\alpha_0}{1 - \dfrac{\alpha_0 \beta}{16\pi\epsilon_0 r^3}} \cdot E_{\text{in}} \\ &= \alpha_{\text{eff}} \cdot E_{\text{in}} \ , \end{aligned} \tag{3.8}$$

with the effective polarizability α_{eff} of the coupled tip-sample system

$$\alpha_{\text{eff}} = \frac{\alpha_0}{1 - \dfrac{\alpha_0 \beta}{16\pi\epsilon_0 r^3}} \ . \tag{3.9}$$

The effective polarizability is used to model the near-field interaction via the coupling term $1 - \frac{\alpha_0 \beta}{16\pi\epsilon_0 r^3}$, which depends on the dielectric function of the sample via the reflection coefficient $\beta(\epsilon_{\text{sample}})$. In addition, the coupling term nonlinearly depends on the distance r between the tip and the sample. Note that for large distances r, the effective polarizability reduces to the uncoupled case and $\alpha_{\text{eff}} \approx \alpha_0$.

Since the external electromagnetic driving field $E(t) = E_{\text{in}} \cdot \mathrm{e}^{(i2\pi\nu t)}$ is time-dependent, also the induced polarization of the tip p_{tip} oscillates, leading to the emission of electromagnetic radiation, which carries information about the optical properties of the sample into the far field. As long as the polarization response is linear with the applied electric field, the scattered radiation can be calculated for each frequency individually and is written in the frequency domain as [Ras03, Kei04]

$$\tilde{E}_{\text{tip}}(\nu) \propto \alpha_{\text{eff}}(\nu) \cdot \tilde{E}_{\text{in}}(\nu) \ . \tag{3.10}$$

$\alpha_0(\nu)$, $\beta(\nu)$ and with that $\alpha_{\text{eff}}(\nu)$ are in general complex-valued functions that depend on the light frequency ν via the dielectric values of the tip $\epsilon_{\text{tip}}(\nu)$ and the sample $\epsilon_{\text{sample}}(\nu)$.

For a complete description of the scattered radiation, the indirect illumination of the light reflected off the sample surface has to be considered as well [Ras03, Ren05, Cvi07].

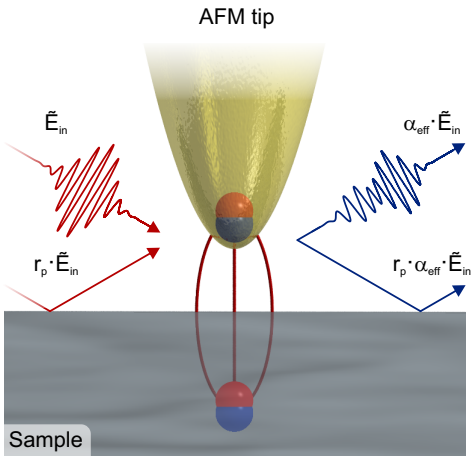

Figure 3.5 | Surface reflection. The effective tip-sample dipole is polarized by an incoming external driving field (red curves) that is composed of two contributions: The first contribution couples directly to the tip-sample system, while the second contribution is reflected at the air-sample interface (Fresnel coefficient $r_\mathrm{p}(\nu)$) before illuminating the tip. The same effect also arises upon re-radiation (blue curves). Some of the scattered light is reflected off the sample surface $r_\mathrm{p}(\nu)\cdot\alpha_\mathrm{eff}(\nu)\cdot\tilde{E}_\mathrm{in}(\nu)$, while most of the scattered radiation directly couples to the far field via $\alpha_\mathrm{eff}(\nu)\cdot\tilde{E}_\mathrm{in}(\nu)$. Since $r_\mathrm{p}(\nu)$ depends on the light frequency ν via $\epsilon_\mathrm{sample}(\nu)$, it has to be incorporated into the theoretical description.

This situation is depicted in Fig. 3.5. The electric field of the incoming radiation (red curves) is composed of two contributions, both polarized parallel to the plane of incidence: The first contribution, $\tilde{E}_\mathrm{in}(\nu)$, directly couples to the tip-sample dipole from the far-field. The second contribution, $r_\mathrm{p}(\nu)\cdot\tilde{E}_\mathrm{in}(\nu)$, is reflected off the sample surface, leading to a reduction of the field strength by the Fresnel coefficient $r_\mathrm{p}(\nu)$ before the light impinges on the tip. The same effect arises upon re-radiation (blue curves). Here, some of the scattered light is reflected off the sample surface leading to a reduced field strength of the radiation by $r_\mathrm{p}(\nu)\cdot\alpha_\mathrm{eff}(\nu)\cdot\tilde{E}_\mathrm{in}(\nu)$. In the far field, this radiation is superimposed with the directly scattered electric field $\alpha_\mathrm{eff}(\nu)\cdot\tilde{E}_\mathrm{in}(\nu)$. Hence, the total scattered radiation is[2]

$$\tilde{E}_\mathrm{scat}(\nu)\propto\Big(1+r_\mathrm{p}(\nu)\Big)^2\cdot\alpha_\mathrm{eff}(\nu)\cdot\tilde{E}_\mathrm{in}(\nu)\ . \tag{3.11}$$

For light polarized parallel to the plane of incidence, the Fresnel reflection coefficient $r_\mathrm{p}(\nu)$

[2] In early implementations of the point-dipole model the total scattered radiation was described by a superposition of both tip and image dipole fields [Kno00, Ras03, Kei04]

$$\tilde{E}_\mathrm{scat}(\nu)=\Big(1+\beta(\nu)\Big)\cdot\alpha_\mathrm{eff}(\nu)\cdot\tilde{E}_\mathrm{in}(\nu)\ .$$

However, the reflection coefficient $\beta(\nu)$ diverges for dielectric values $\epsilon_\mathrm{sample}(\nu)\approx-1$. The consequence would be a violation of energy conservation since the image dipole would radiate more strongly than the tip dipole. In addition, the indirect illumination of the tip by reflection off the sample surface is not considered [Ras03, Ren05]. The early point-dipole model has therefore been reconsidered and the $1+\beta(\nu)$ term has been replaced by $(1+r_\mathrm{p}(\nu))^2$ [Cvi07].

of the air-sample interface is given by

$$r_{\mathrm{p}}(\nu) = \frac{\sqrt{\epsilon_{\mathrm{sample}}(\nu)} \cdot \cos(\theta_i) - \cos(\theta_t)}{\sqrt{\epsilon_{\mathrm{sample}}(\nu)} \cdot \cos(\theta_i) + \cos(\theta_t)} \ . \tag{3.12}$$

Here, $\theta_i = 60\,^\circ$ is the input angle of the radiation with respect to the surface normal of the sample. The angle of transmission can be calculated using Snell's law

$$\theta_t = \arcsin\left(\frac{1}{\sqrt{\epsilon_{\mathrm{sample}}(\nu)}} \cdot \sin(\theta_i)\right) \ . \tag{3.13}$$

In conclusion, the scattered signals depend on the complex-valued dielectric function of the tip $\epsilon_{\mathrm{tip}}(\nu)$, the sample $\epsilon_{\mathrm{sample}}(\nu)$ and the radius of curvature a via the effective polarizability α_{eff} and $r_{\mathrm{p}}(\nu)$, as well as on the input angle θ_i via $r_{\mathrm{p}}(\nu)$. Since all parameters except for $\epsilon_{\mathrm{sample}}$ are constant during measurements, an observed optical contrast can solely be attributed to a change of the optical properties of the sample.

3.2.2 Tapping mode operation and lock-in detection

As seen in Section 2.4 the AFM tip of the microscope is operated in tapping mode. Hence, the strong nonlinear dependence of the effective polarizability $\alpha_{\mathrm{eff}}(\nu)$ on the distance r can be exploited to efficiently suppress background radiation by lock-in detection. This is done by detecting the scattered radiation at higher harmonics n ($n \in \mathbb{N}$) of the tip-tapping frequency Ω_{tip}. To reasonably describe the signals measured with a lock-in, the concept of tapping mode operation has to be implemented in the theory by introducing a time-dependent distance $r(t)$ that simulates the oscillation of the tip above the sample surface. Thus, the effective polarization in Equation 3.9 is modified to

$$\alpha_{\mathrm{eff}}(\nu, t) = \frac{\alpha_0(\nu)}{1 - \dfrac{\alpha_0(\nu)\beta(\nu)}{16\pi\epsilon_0(r(t))^3}} \ , \tag{3.14}$$

with

$$\begin{aligned} r(t) &= a + z(t) \\ &= a + \mathrm{TA} \cdot \Big(1 + \cos(\Omega_{\mathrm{tip}} t)\Big) + z_0 \ . \end{aligned} \tag{3.15}$$

The distance $r(t)$ is composed of the tip radius of curvature a, the harmonic oscillation of the tip with a tapping frequency Ω_{tip} and a tapping amplitude TA, and a minimum offset

z_0 of the lower inflection point of the oscillation. In the experiment z_0 is on the order of 0.5 to 2 nm, whereby in the theory z_0 only influences the total scattering efficiency by a constant scaling factor and is therefore approximated to be zero.

For further analysis it is convenient to write the complex-valued effective polarization $\alpha_{\text{eff}}(\nu, t)$ in the polar representation

$$\alpha_{\text{eff}}(\nu, t) = s(\nu, t) \cdot \mathrm{e}^{i\theta(\nu,t)} \ , \tag{3.16}$$

where

$$s(\nu, t) = |\alpha_{\text{eff}}(\nu, t)| \quad \text{and} \quad \theta(\nu, t) = \measuredangle\left(\alpha_{\text{eff}}(\nu, t)\right) \ . \tag{3.17}$$

The anharmonic response of $\alpha_{\text{eff}}(\nu, t)$ as a function of tip-tapping time t can be expanded in a Fourier series with respect to Ω_{tip}

$$\begin{aligned} \alpha_{\text{eff}}(\nu, t) &= \sum_{n=0}^{\infty} \alpha_n(\nu) \cdot \mathrm{e}^{in\Omega_{\text{tip}}t} \\ s(\nu, t) \cdot \mathrm{e}^{i\theta(\nu,t)} &= \sum_{n=0}^{\infty} s_n(\nu) \cdot \mathrm{e}^{i\theta_n(\nu)} \cdot \mathrm{e}^{in\Omega_{\text{tip}}t} \ , \end{aligned} \tag{3.18}$$

where the corresponding Fourier coefficients for $n > 1$ are numerically calculated using

$$\alpha_n(\nu) = s_n(\nu) \cdot \mathrm{e}^{i\theta_n(\nu)} = \frac{\Omega_{\text{tip}}}{\pi} \int_0^{2\pi/\Omega_{\text{tip}}} dt' \, \alpha_{\text{eff}}(\nu, t') \cdot \mathrm{e}^{-in\Omega_{\text{tip}}t'} \ . \tag{3.19}$$

The total, scattered electric field $\tilde{E}_{\text{scat}}(\nu)$ at the frequency ν can now be written as a sum over all harmonics of the tip-tapping frequency

$$\begin{aligned} \tilde{E}_{\text{scat}}(\nu) &\propto \Big(1 + r_{\text{p}}(\nu)\Big)^2 \cdot \sum_{n=0}^{\infty} \alpha_n(\nu) \cdot \mathrm{e}^{in\Omega_{\text{tip}}t} \cdot \tilde{E}_{\text{in}}(\nu) \\ &= \Big(1 + r_{\text{p}}(\nu)\Big)^2 \cdot \sum_{n=0}^{\infty} s_n(\nu) \cdot \mathrm{e}^{i\theta_n(\nu)} \cdot \mathrm{e}^{in\Omega_{\text{tip}}t} \cdot \tilde{E}_{\text{in}}(\nu) \ , \end{aligned} \tag{3.20}$$

leading to the following general expression for the scattered electric field $\tilde{E}^n_{\text{scat}}(\nu)$ measured with the lock-in at $n \cdot \Omega_{\text{tip}}$

$$\begin{aligned} \tilde{E}^n_{\text{scat}}(\nu) &= C \cdot \Big(1 + r_{\text{p}}(\nu)\Big)^2 \cdot \alpha_n(\nu) \cdot \tilde{E}_{\text{in}}(\nu) \\ &= C \cdot \Big(1 + r_{\text{p}}(\nu)\Big)^2 \cdot s_n(\nu) \cdot \mathrm{e}^{i\theta_n(\nu)} \cdot \tilde{E}_{\text{in}}(\nu) \ . \end{aligned} \tag{3.21}$$

With Equation 3.21 the electric field measured in the experiment by EOS at the third

harmonic of Ω_{tip} can be modeled. The detected reference spectrum from the FTIR delay line (see Section 2.4.1) is here used as input field $\tilde{E}_{\mathrm{in}}(\nu)$

$$\begin{aligned}\tilde{E}^{3}_{\mathrm{scat}}(\nu) &= C \cdot \Big(1 + r_{\mathrm{p}}(\nu)\Big)^{2} \cdot \alpha_{3}(\nu) \cdot \tilde{E}_{\mathrm{in}}(\nu) \\ &= C \cdot \Big(1 + r_{\mathrm{p}}(\nu)\Big)^{2} \cdot s_{3}(\nu) \cdot \mathrm{e}^{i\theta_{3}(\nu)} \cdot \tilde{E}_{\mathrm{in}}(\nu)\ . \end{aligned} \tag{3.22}$$

Meanwhile, $r_{\mathrm{p}}(\nu)$, $\alpha_{3}(\nu)$, $s_{3}(\nu)$ and $\theta_{3}(\nu)$ are completely determined by the complex-valued dielectric functions $\epsilon_{\mathrm{tip}}(\nu)$ and $\epsilon_{\mathrm{sample}}(\nu)$. The constant scaling factor C is used to match the magnitude of the simulated amplitude spectrum to the experimental data and is determined in time-resolved studies from the spectrum scattered off the unexcited sample. Since EOS provides direct access to the oscillating electric field of the scattered radiation, both the amplitude and absolute phase of the electric near field at the third demodulation order are detected. Hence, a direct comparison between the simulation and the experiment is possible and the complex-valued dielectric function $\epsilon_{\mathrm{sample}}(\nu)$ can be modeled. Yet, it has to be mentioned that the elongated shape of the tip can lead to a frequency-dependent modification of the tip polarizability $\alpha_{0}(\nu)$, similar to an antenna resonance. Hence, the scattering efficiency is a tip-dependent function, influencing the bandwidth and phase of the scattered radiation. This can be seen for instance by comparing the reference waveform to the scattered waveform in Fig. 2.12. However, the influence of the tip shape on the scattered spectra can be eliminated in time-resolved measurements by extracting an effective input field from a measurement performed at a negative pump-gate delay time t_{ref}, which incorporates the tip response. The scattered field $\tilde{E}^{n}_{\mathrm{scat}}(\nu, t_{\mathrm{pg}})$ at positive delay times is consequently calculated by

$$\tilde{E}^{n}_{\mathrm{scat}}(\nu, t_{\mathrm{pg}}) = \frac{\Big[\Big(1 + r_{\mathrm{p}}(\nu)\Big)^{2} \cdot s_{n}(\nu) \cdot \mathrm{e}^{i\theta_{n}(\nu)}\Big]_{t_{\mathrm{pg}}}}{\Big[\Big(1 + r_{\mathrm{p}}(\nu)\Big)^{2} \cdot s_{n}(\nu) \cdot \mathrm{e}^{i\theta_{n}(\nu)}\Big]_{t_{\mathrm{ref}}}} \cdot \tilde{E}^{n}_{\mathrm{scat}}(\nu, t_{\mathrm{ref}})\ . \tag{3.23}$$

However, for the electro-optic measurements of the scattered near field presented in this work, the best agreement between theory and experiment has been achieved by directly using the reference field from the FTIR delay line as input field.

3.2.3 Intensity-based detection of the scattered radiation

In contrast to field-resolved studies, conventional intensity-resolved detection using the MCT photodiode measures the absolute square of the scattered electric field. In addition, the photodiode integrates over all frequency components ν in the probe-pulse spectrum. Thus, the total scattered intensity is calculated by taking the integral over all contributing

frequency components of $|\tilde{E}_{\mathrm{scat}}(\nu)|^2$

$$I_{\mathrm{scat}} = \int_0^\infty d\nu' \, \tilde{E}_{\mathrm{scat}}(\nu') \cdot \tilde{E}^*_{\mathrm{scat}}(\nu') \ . \tag{3.24}$$

Using Equation 3.20, I_{scat} is expanded in a Fourier series to relate to the signals measured by lock-in detection

$$\begin{aligned} I_{\mathrm{scat}} \propto \int_0^\infty d\nu' \left(1 + r_{\mathrm{p}}(\nu')\right)^2 \left(1 + r^*_{\mathrm{p}}(\nu')\right)^2 \cdot |\tilde{E}_{\mathrm{in}}(\nu')|^2 \\ \cdot \sum_{k=0}^{\infty} s_k(\nu') \cdot \mathrm{e}^{i\theta_k(\nu')} \cdot \mathrm{e}^{ik\Omega_{\mathrm{tip}}t} \\ \cdot \sum_{l=0}^{\infty} s_l(\nu') \cdot \mathrm{e}^{-i\theta_l(\nu')} \cdot \mathrm{e}^{-il\Omega_{\mathrm{tip}}t} \ . \end{aligned} \tag{3.25}$$

The indices k and l ($k, l \in \mathbb{N}$) describe the harmonic order of the Fourier expansion of the two scattered field components with respect to the tapping frequency Ω_{tip}. This expression can be simplified by rearranging the exponential functions such that

$$\begin{aligned} I_{\mathrm{scat}} \propto \int_0^\infty d\nu' \left(1 + r_{\mathrm{p}}(\nu')\right)^2 \left(1 + r^*_{\mathrm{p}}(\nu')\right)^2 \cdot |\tilde{E}_{\mathrm{in}}(\nu')|^2 \\ \cdot \sum_{k=0}^{\infty} \sum_{l=0}^{\infty} s_k(\nu') s_l(\nu') \cdot \mathrm{e}^{i(\theta_k(\nu') - \theta_l(\nu'))} \cdot \mathrm{e}^{i(k-l)\Omega_{\mathrm{tip}}t} \ . \end{aligned} \tag{3.26}$$

The oscillatory function $\mathrm{e}^{i(k-l)\Omega_{\mathrm{tip}}t}$, describing the oscillation of the tip at a frequency $(k-l)\Omega_{\mathrm{tip}}$, now depends on the two indices k and l. For the scattered intensity to be measured by lock-in detection at the nth harmonic of Ω_{tip}, the oscillatory function has to fulfill the following condition

$$\mathrm{e}^{i(k-l)\Omega_{\mathrm{tip}}t} \equiv \mathrm{e}^{in\Omega_{\mathrm{tip}}t} \ , \text{with } n = k - l \ . \tag{3.27}$$

This condition cancels the summation over the k-index by requiring $k = n + l$. Hence, the scattered intensity I^n_{scat} at the nth harmonic can in general be written as follows

$$\begin{aligned} I^n_{\mathrm{scat}} = D \cdot \int_0^\infty d\nu' \left|1 + r_{\mathrm{p}}(\nu')\right|^2 \cdot |\tilde{E}_{\mathrm{in}}(\nu')|^2 \\ \cdot \sum_{l=0}^{\infty} s_{n+l}(\nu') s_l(\nu') \cdot \mathrm{e}^{i(\theta_{n+l}(\nu') - \theta_l(\nu'))} \ , \end{aligned} \tag{3.28}$$

using D as constant scaling factor. Importantly, the intensity I^n_{scat} depends not solely on the nth harmonic of the effective polarizability, but rather on a convolution of all

harmonics. For instance, at the 3rd harmonic Equation 3.28 reads

$$I^3_{\mathrm{scat}} = D \cdot \int_0^\infty d\nu' \left|1 + r_{\mathrm{p}}(\nu')\right|^2 \cdot |\tilde{E}_{\mathrm{in}}(\nu')|^2 \cdot \Big[s_3(\nu') s_0(\nu') \cdot \mathrm{e}^{i(\theta_3(\nu') - \theta_0(\nu'))} + s_4(\nu') s_1(\nu') \cdot \mathrm{e}^{i(\theta_4(\nu') - \theta_1(\nu'))} + \dots \Big] \,. \tag{3.29}$$

The influence of the different harmonic orders on the observed near-field signal can usually be ignored in time-integrated (steady-state) measurements. Since $s_0(\nu)$ is much larger than the amplitudes at higher orders, all terms in the series beyond the first one are negligible. In addition, $s_0(\nu)$ acts similar to the far-field reflection coefficient and is relatively insensitive to the tip position. Changes to the scattered intensity I^3_{scat} observed by scanning the sample on the nanoscale can therefore be directly attributed to $s_3(\nu)$. However, when performing pump-probe measurements, this situation has to be reconsidered. Upon photoexcitation the optical properties of an extended region of the sample can be altered, which in turn significantly changes $s_0(\nu)$ and thus directly influences I^3_{scat}. In contrast to field-resolved measurements, where no convolution between different harmonics is present, this circumstance can not be avoided and should be considered in the interpretation of the sample contrast.

3.2.4 Spectral information using nano-FTIR

The MCT photodiode that measures the scattered intensity is also used to perform standard FTIR spectroscopy [Hut11, Wag14b]. Here, the scattered radiation is overlapped in time and space with a reference multi-THz pulse on the MCT detector, as described in Section 2.4.2. The delay of the reference pulse t_{FTIR} is scanned relative to the scattered probe pulse and the resulting intensity interferogram is recorded. The reference waveform is, to a good approximation, identical to the waveform incident on the near-field tip. Hence, $\tilde{E}_{\mathrm{ref}}(\nu)$ can be written as

$$\begin{aligned} \tilde{E}_{\mathrm{ref}}(\nu, t_{\mathrm{FTIR}}) &= \tilde{E}_{\mathrm{in}}(\nu) \cdot \mathrm{e}^{-i2\pi\nu t_{\mathrm{FTIR}}} \\ &= |\tilde{E}_{\mathrm{in}}(\nu)| \cdot \mathrm{e}^{i\phi_{\mathrm{in}}(\nu)} \cdot \mathrm{e}^{-i2\pi\nu t_{\mathrm{FTIR}}} \,, \end{aligned} \tag{3.30}$$

where $|\tilde{E}_{\mathrm{in}}(\nu)|$ is the amplitude and $\phi_{\mathrm{in}}(\nu)$ the phase of the input waveform. The additional phase $\phi_{\mathrm{FTIR}} = -2\pi\nu t_{\mathrm{FTIR}}$ introduced by the FTIR delay line depends on the frequency ν and the relative delay t_{FTIR}. For convenience the scattered electric field is also written

in the polar representation

$$\tilde{E}_{\mathrm{scat}}(\nu) = |\tilde{E}_{\mathrm{scat}}(\nu)| \cdot \mathrm{e}^{i\phi_{\mathrm{scat}}(\nu)} \ . \tag{3.31}$$

The total, scattered intensity $I_{\mathrm{scat,\ total}}(t_{\mathrm{FTIR}})$ measured by the photodiode at a given delay t_{FTIR} can now be calculated by integrating over all contributing frequency components

$$I_{\mathrm{scat,\ total}}(t_{\mathrm{FTIR}}) = \int_0^\infty d\nu' \, |\tilde{E}_{\mathrm{scat}}(\nu') + \tilde{E}_{\mathrm{ref}}(\nu', t_{\mathrm{FTIR}})|^2 \ , \tag{3.32}$$

or equivalently

$$\begin{aligned} I_{\mathrm{scat,\ total}}(t_{\mathrm{FTIR}}) = \int_0^\infty d\nu' \Big[& |\tilde{E}_{\mathrm{scat}}(\nu')|^2 + |\tilde{E}_{\mathrm{ref}}(\nu', t_{\mathrm{FTIR}})|^2 \\ & + \tilde{E}_{\mathrm{scat}}(\nu')\tilde{E}^*_{\mathrm{ref}}(\nu', t_{\mathrm{FTIR}}) + \tilde{E}^*_{\mathrm{scat}}(\nu')\tilde{E}_{\mathrm{ref}}(\nu', t_{\mathrm{FTIR}}) \Big] \ . \end{aligned} \tag{3.33}$$

By inserting the polar representation of the reference field (Equation 3.30) and the scattered field (Equation 3.31), the equation can be simplified to

$$\begin{aligned} I_{\mathrm{scat,\ total}}(t_{\mathrm{FTIR}}) = \int_0^\infty d\nu' \Big[& |\tilde{E}_{\mathrm{scat}}(\nu')|^2 + |\tilde{E}_{\mathrm{ref}}(\nu', t_{\mathrm{FTIR}})|^2 \\ & + 2 \cdot |\tilde{E}_{\mathrm{scat}}(\nu')||\tilde{E}_{\mathrm{in}}(\nu')| \cos(\phi_{\mathrm{scat}}(\nu') - \phi_{\mathrm{in}}(\nu') + 2\pi\nu' t_{\mathrm{FTIR}}) \Big] \ . \end{aligned} \tag{3.34}$$

The second term $|\tilde{E}_{\mathrm{ref}}(\nu, t_{\mathrm{FTIR}})|^2$ in Equation 3.34 corresponds to the intensity of the multi-THz radiation in the reference arm. Since its intensity is not modulated at Ω_{tip}, this term does not contribute to the signal measured with the lock-in and can therefore be neglected. In contrast, the first term $|\tilde{E}_{\mathrm{scat}}(\nu)|^2$ corresponds to the intensity of the scattered radiation and leads to a constant offset of the recorded interferogram at the nth demodulation order (see Fig. 2.13). The third term gives rise to a frequency-dependent modulation of the scattered intensity as a function of t_{FTIR} that contains spectral information about the scattered near-field radiation. In the following discussion only the last term is therefore considered, which is given by

$$\begin{aligned} I_{\mathrm{scat}}(t_{\mathrm{FTIR}}) = 2 \int_0^\infty d\nu' \, & |\tilde{E}_{\mathrm{scat}}(\nu')||\tilde{E}_{\mathrm{in}}(\nu')| \\ & \cdot \cos(\phi_{\mathrm{scat}}(\nu') - \phi_{\mathrm{in}}(\nu') + 2\pi\nu t_{\mathrm{FTIR}}) \ . \end{aligned} \tag{3.35}$$

To extract the scattered spectrum at the frequency ν_0, the Fourier transform of the detected interferogram $I_{\mathrm{scat}}(t_{\mathrm{FTIR}})$ is calculated

$$\begin{aligned}\tilde{I}_{\mathrm{scat}}(\nu_0) = 2\int_{-\infty}^{\infty} dt_{\mathrm{FTIR}} \int_0^{\infty} d\nu' \, |\tilde{E}_{\mathrm{scat}}(\nu')||\tilde{E}_{\mathrm{in}}(\nu')| \\ \cdot \cos(\phi_{\mathrm{scat}}(\nu') - \phi_{\mathrm{in}}(\nu') + 2\pi\nu' t_{\mathrm{FTIR}}) \cdot \mathrm{e}^{-i2\pi\nu_0 t_{\mathrm{FTIR}}} \\ = \int_{-\infty}^{\infty} dt_{\mathrm{FTIR}} \int_0^{\infty} d\nu' \, |\tilde{E}_{\mathrm{scat}}(\nu')||\tilde{E}_{\mathrm{in}}(\nu')| \\ \cdot \Big[\mathrm{e}^{i(\phi_{\mathrm{scat}}(\nu') - \phi_{\mathrm{in}}(\nu'))} \mathrm{e}^{i2\pi(\nu'-\nu_0)t_{\mathrm{FTIR}}} \\ + \mathrm{e}^{-i(\phi_{\mathrm{scat}}(\nu') - \phi_{\mathrm{in}}(\nu'))} \mathrm{e}^{i2\pi(-\nu'-\nu_0)t_{\mathrm{FTIR}}}\Big] \, , \end{aligned} \tag{3.36}$$

where the relation $\cos(x) = \frac{1}{2}(\mathrm{e}^{ix} - \mathrm{e}^{-ix})$ is used. The expression can be further simplified with the help of the integral representation of the Dirac delta distribution

$$\int_{-\infty}^{\infty} dt \, \mathrm{e}^{i2\pi(\nu-\nu_0)t} = 2\pi\delta(\nu - \nu_0) \, , \tag{3.37}$$

which results in

$$\begin{aligned}\tilde{I}_{\mathrm{scat}}(\nu_0) = \; 2\pi \int_0^{\infty} d\nu' \, |\tilde{E}_{\mathrm{scat}}(\nu')||\tilde{E}_{\mathrm{in}}(\nu')| \\ \cdot \Big[\mathrm{e}^{i(\phi_{\mathrm{scat}}(\nu') - \phi_{\mathrm{in}}(\nu'))} \cdot \delta(\nu' - \nu_0) + \mathrm{e}^{-i(\phi_{\mathrm{scat}}(\nu') - \phi_{\mathrm{in}}(\nu'))} \cdot \delta(-\nu' - \nu_0)\Big] \, . \end{aligned} \tag{3.38}$$

The frequency integration cancels the delta distributions and leads to an evaluation of $\tilde{I}(\nu_0)$ at positive and negative frequencies ν_0 and $-\nu_0$, respectively

$$\begin{aligned}\tilde{I}_{\mathrm{scat}}(\nu_0) = \; 2\pi \cdot \Big[|\tilde{E}_{\mathrm{scat}}(\nu_0)||\tilde{E}_{\mathrm{in}}(\nu_0)| \cdot \mathrm{e}^{i(\phi_{\mathrm{scat}}(\nu_0) - \phi_{\mathrm{in}}(\nu_0))} \\ + |\tilde{E}_{\mathrm{scat}}(-\nu_0)||\tilde{E}_{\mathrm{in}}(-\nu_0)| \cdot \mathrm{e}^{-i(\phi_{\mathrm{scat}}(-\nu_0) - \phi_{\mathrm{in}}(-\nu_0))}\Big] \, . \end{aligned} \tag{3.39}$$

In Fourier space the field components at positive and negative frequencies are related such that $\tilde{E}(\nu) = \tilde{E}^*(-\nu)$. Hence the amplitude is symmetric ($|\tilde{E}(\nu)| = |\tilde{E}(-\nu)|$) and the phase is antisymmetric ($\phi(\nu) = -\phi(-\nu)$) with respect to the origin of the frequency axis. Equation 3.39 can therefore be rewritten as

$$\begin{aligned}\tilde{I}_{\mathrm{scat}}(\nu_0) = \; 4\pi \cdot |\tilde{E}_{\mathrm{scat}}(\nu_0)||\tilde{E}_{\mathrm{in}}(\nu_0)| \cdot \mathrm{e}^{i(\phi_{\mathrm{scat}}(\nu_0) - \phi_{\mathrm{in}}(\nu_0))} \\ = \; 4\pi \cdot \tilde{E}_{\mathrm{scat}}(\nu_0)\tilde{E}^*_{\mathrm{in}}(\nu_0) \, . \end{aligned} \tag{3.40}$$

Now, the expression for the scattered electric field derived in Equation 3.20 can be inserted

$$\tilde{I}_{\mathrm{scat}}(\nu) = F \cdot \Big(1 + r_{\mathrm{p}}(\nu)\Big)^2 \cdot \sum_{n=0}^{\infty} s_n(\nu) \cdot \mathrm{e}^{i\theta_n(\nu)} \cdot \mathrm{e}^{in\Omega_{\mathrm{tip}}t} \cdot |\tilde{E}_{\mathrm{in}}(\nu)|^2 \ . \tag{3.41}$$

Here, the variable ν_0 has been redefined as ν and a constant scaling factor F has been introduced which contains all scalar prefactors. The scattered intensity $\tilde{I}^n_{\mathrm{scat}}(\nu)$ calculated from the interferogram $I(t_{\mathrm{FTIR}})$, which is measured with the lock-in at the nth demodulation order, is in general given by

$$\tilde{I}^n_{\mathrm{scat}}(\nu) = F \cdot \Big(1 + r_{\mathrm{p}}(\nu)\Big)^2 \cdot s_n(\nu) \cdot \mathrm{e}^{i\theta_n(\nu)} \cdot |\tilde{E}_{\mathrm{in}}(\nu)|^2 \ . \tag{3.42}$$

It is important to note, that the phase of the scattered intensity $\tilde{I}^n_{\mathrm{scat}}(\nu)$ only describes the relative phase between the reference and the scattered radiation, which is induced by the scattering process. The phase information of the input radiation is lost due to the intensity-based detection scheme ($|\tilde{E}_{\mathrm{in}}(\nu)|^2$). In contrast to EOS, nano-FTIR is therefore only capable of detecting the scattered amplitude spectrum with a relative phase. Equation 3.42 also reveals that the spectrally resolved intensities measured by nano-FTIR at the nth demodulation order are not convoluted by different harmonics of the scattered polarizability, contrary to the scattered intensities detected directly using the MCT photodiode (see Equation 3.28). Thus, nano-FTIR can be used as a reliable way to extract spectral information from the scattered near-field radiation. The direct simulation of $\tilde{I}^n_{\mathrm{scat}}(\nu)$ is, however, challenging since $|\tilde{E}_{\mathrm{in}}(\nu)|^2$ is currently not obtainable with the experimental setup. In time-resolved measurements, this uncertainty can be eliminated by extracting $|\tilde{E}_{\mathrm{in}}(\nu)|^2$ from the spectrum recorded at a negative pump-probe delay time t_{ref}. $\tilde{I}^n_{\mathrm{scat}}(\nu, t_{\mathrm{pp}})$ at positive delay times is then calculated in the following way

$$\tilde{I}^n_{\mathrm{scat}}(\nu, t_{\mathrm{pp}}) = \frac{\Big[\Big(1 + r_{\mathrm{p}}(\nu)\Big)^2 \cdot s_n(\nu) \cdot \mathrm{e}^{i\theta_n(\nu)}\Big]_{t_{\mathrm{pp}}}}{\Big[\Big(1 + r_{\mathrm{p}}(\nu)\Big)^2 \cdot s_n(\nu) \cdot \mathrm{e}^{i\theta_n(\nu)}\Big]_{t_{\mathrm{ref}}}} \cdot \tilde{I}^n_{\mathrm{scat}}(\nu, t_{\mathrm{ref}}) \ . \tag{3.43}$$

The theoretical understanding of the origin of the scattered electric field and the scattered intensity, builds the foundation to extract quantitative information out of the observed dynamics in the near-field experiments. It has to be stressed that the only fitting parameter used to model the sample response in this work is the sample dielectric function $\epsilon_{\mathrm{sample}}$.

3.2.5 The impact of the sample dielectric function

The interpretation of an observed material contrast is a key challenge in near-field microscopy and requires a good understanding of the influence of the dielectric function of the sample ϵ_{sample} on the scattering process. To investigate this dependence, the complex-valued scattering efficiency $A_3(\epsilon_{\text{sample}}) \cdot \mathrm{e}^{i\phi_3(\epsilon_{\text{sample}})}$ is defined at the third demodulation order using Equation 3.21 to

$$\frac{E^3_{\text{scattered}}}{E_{\text{in}}} = A_3(\epsilon_{\text{sample}}) \cdot \mathrm{e}^{i\phi_3(\epsilon_{\text{sample}})} = C \cdot \Big(1 + r_{\text{p}}(\epsilon_{\text{sample}})\Big)^2 \cdot \alpha_3(\epsilon_{\text{tip}}, \epsilon_{\text{sample}}) \ , \quad (3.44)$$

which contains the full scattering information of the tip-sample system. In the following calculations, the dielectric function of the tip[3] is set constant to $\epsilon_{\text{tip}} = -3386 + i1457$. The amplitude and phase of the scattering efficiency evaluated as a function of the real part $\epsilon_{\text{real}} = \text{Re}(\epsilon_{\text{sample}})$ of the sample dielectric function can be seen in Fig. 3.6a and b, respectively. Here, the imaginary part $\epsilon_{\text{imag}} = \text{Im}(\epsilon_{\text{sample}})$ of the dielectric function is used as a constant parameter, with values of $\epsilon_{\text{imag}} = 1, 5, 10$ and $\lim_{\epsilon_{\text{imag}}\to\infty} \epsilon_{\text{imag}}$. The amplitude $A_3(\epsilon_{\text{sample}})$ is normalized to $A_3(\epsilon_{\text{sample}} = 0 + i \lim_{\epsilon_{\text{imag}}\to\infty} \epsilon_{\text{imag}})$. For $\epsilon_{\text{imag}} = 1$ and $\epsilon_{\text{real}} \ll -100$, the amplitude of the scattering efficiency $A_3(\epsilon_{\text{sample}}) \approx 1$ (not shown). With increasing ϵ_{real} (black curve in Fig. 3.6a) the amplitude slightly decreases before dropping rapidly at $\epsilon_{\text{real}} = -2.5$ towards a minimum value of $A_3(\epsilon_{\text{sample}}) \approx 0.06$ at $\epsilon_{\text{real}} = 0.8$. This drop is followed by a recovery of $A_3(\epsilon_{\text{sample}})$ towards 1 for $\epsilon_{\text{real}} \to \infty$. The strong change of $A_3(\epsilon_{\text{sample}})$ near the zero-crossing of ϵ_{real} is attributed to a near-field resonance of the coupled tip-sample system [Kei04], which is also visible in the corresponding phase (black curve in Fig. 3.6b). Approaching the zero-crossing of ϵ_{real} from the negative side the phase increases, reaching a peak value of $\phi_3 \approx \pi\,\text{rad}$ at $\epsilon_{\text{real}} = -0.9$. This is followed by a fast reduction towards $\phi_3 = 0\,\text{rad}$. The width of the near-field resonance in the amplitude and phase of the scattering efficiency directly depends on the value of ϵ_{imag} (see Fig. 3.6a and b). With increasing ϵ_{imag} the near-field resonance broadens and the minimum position of $A_3(\epsilon_{\text{sample}})$ shifts towards larger values of ϵ_{real}, as indicated by the gray dashed line in Fig. 3.6a. In contrast, the peak in the phase of the scattering efficiency moves towards smaller values of ϵ_{real} as a function of ϵ_{imag} (gray dashed line in Fig. 3.6b). For $\epsilon_{\text{imag}} \to \infty$ (yellow curve) the scattering efficiency is independent of ϵ_{real}, resulting in a constant amplitude of $A_3(\epsilon_{\text{sample}}) = 1$ and a constant phase of $\phi_3 = 0\,\text{rad}$.

In Fig. 3.6c and d, the full dependence of $A_3(\epsilon_{\text{sample}})$ on the complex-valued dielectric function ϵ_{sample} is depicted. $A_3(\epsilon_{\text{sample}})$ changes most prominently for values in the proximity of the zero-crossing of ϵ_{real} and for $\epsilon_{\text{imag}} < 50$. From this graph a prediction of the

[3] Dielectric value of gold at a driving frequency $\nu = 30\,\text{THz}$, calculated with the Drude formalism [Rak98].

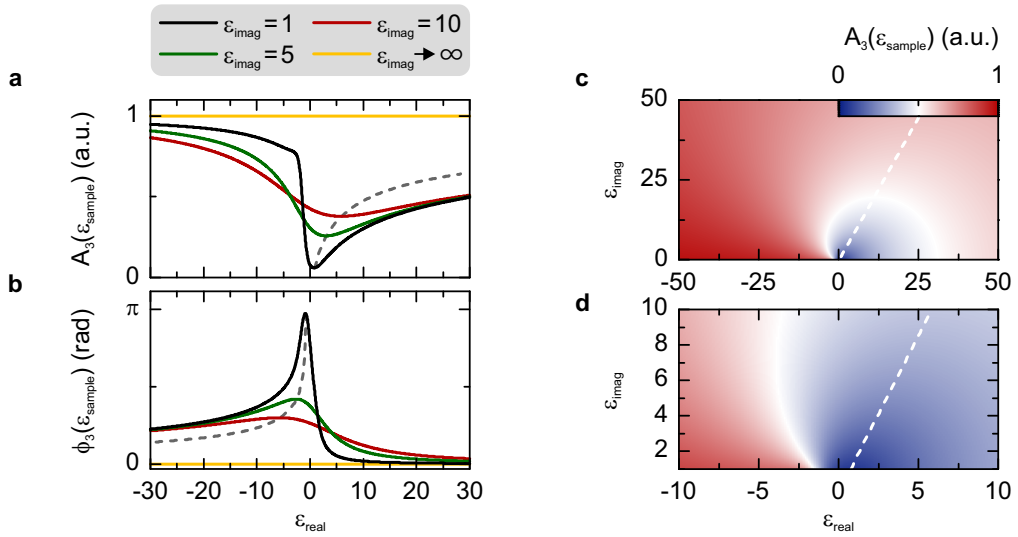

Figure 3.6 | Dependence of the scattering efficiency on the sample dielectric function. **a**, Amplitude $A_3(\epsilon_{\text{sample}})$ of the scattering efficiency as a function of the real part ϵ_{real} of the complex sample dielectric function ϵ_{sample}. The imaginary part of ϵ_{sample} is used as a constant parameter $\epsilon_{\text{imag}} = 1$ (black curve), 5 (green curve), 10 (red curve) and $\lim_{\epsilon_{\text{imag}}\to\infty} \epsilon_{\text{imag}}$ (yellow curve). The gray dashed line indicates the minimum position of $A_3(\epsilon_{\text{sample}})$ as a function of ϵ_{real} and ϵ_{imag} **b**, Corresponding phase ϕ_3 of the scattering efficiency. The gray dashed line indicates the maximum of ϕ_3 as a function of ϵ_{real} and ϵ_{imag} **c**, Dependence of the amplitude $A_3(\epsilon_{\text{sample}})$ on the complex-valued dielectric function ϵ_{sample}. $A_3(\epsilon_{\text{sample}})$ is significantly modified for dielectric values in the proximity of the zero-crossing of ϵ_{real} and for $\epsilon_{\text{imag}} < 50$. **d**, Magnified view of the region close to the zero-crossing of ϵ_{real}. The white dashed lines indicate the minimum position of $A_3(\epsilon_{\text{sample}})$.

image contrast for different materials can be made: Materials, which offer a large negative value of ϵ_{real} in the multi-THz frequency region (e.g. metals), are expected to exhibit an intrinsically strong scattering efficiency. In contrast, materials with a positive real part of the dielectric function, e.g. semiconductors, will feature a lower scattering response. This is especially true for materials with $-1 < \epsilon_{\text{real}} < 10$ and $\epsilon_{\text{imag}} < 10$.

The strong contrast between metallic and semiconducting behavior has already been exploited to investigate the thermally driven phase transition in vanadium dioxide using s-NSOM [Qaz07] and to image regions of high carrier density in nanowires [Sti10]. Note that for semiconductors the scattering efficiency can also be significantly influenced by the presence of phonons [Ren05, Dai14], plasmons [Che12, Fei12, Wag14b] or excitons [Jac12], which modify the dielectric function of the sample.

3.3 Modeling the near-field response of bulk indium arsenide

Indium arsenide is a well-known material whose optical properties have been extensively studied in far-field measurements. The calculated band structure [Saï08] along the $\Gamma - \mathrm{L}$ and $\Gamma - \mathrm{X}$ direction can be seen in Fig. 3.7a. It features a direct band gap with $E_{\mathrm{gap}} = 0.35\,\mathrm{eV}$ at the Γ-point. The effective masses of the electrons or holes are given by the curvature of their respective bands $(1/m^*) \propto \partial^2 E/\partial k^2$ at $k = 0$ (indicated by the red dashed curves), which results in $m_{\mathrm{e}}^* = 0.023 \cdot m_0$ for the electrons in the conduction band and $m_{\mathrm{hh}}^* = 0.41 \cdot m_0$ for the heavy holes in the valence band. Here, m_0 is the mass of a free electron $(9.11 \cdot 10^{-31}\,\mathrm{kg})$. In our experiments, electrons from the valence bands are promoted into the lowest conduction band by means of photon absorption. For a mean photon energy of $E_{\mathrm{photon}} = 0.78\,\mathrm{eV}$, the electrons originate predominately from the heavy-hole band because its density of states is much larger than that of the light-hole band[4]. The process of carrier excitation and recombination in InAs is illustrated in Fig. 3.7b, whereby an intrinsic electron doping of N_{int} is assumed. Upon photoexcitation ($t_{\mathrm{pp}} = 0\,\mathrm{fs}$ or $t_{\mathrm{pg}} = 0\,\mathrm{fs}$), electrons with an excess energy of approximately 0.4 eV are injected into the conduction band by the ultrafast, 22-fs near-infrared pump pulses. Consequently, the total electron density is the sum of the intrinsic and the pump-induced carriers, defined by $N_{\mathrm{c}} = N_{\mathrm{int}} + N_{\mathrm{pump}}$. With evolving pump-probe delay time, the hot electron gas thermalizes via electron-electron and electron-phonon scattering and the electron and hole populations decay through the following mechanisms:

Radiative recombination: Electrons and holes decay via direct band-to-band recombination at the Γ-point. The energy released in the annihilation process is emitted as a photon. Recombination times for bulk InAs are typically larger than 1 ns [Vod92].

Shockley–Read–Hall recombination: Here, the decay of the carrier population is caused by defects and impurities in the crystal, which can form trapped states within the band gap. The electrons relax non-radiatively in a two-step process via the defect states into the valence band and recombine with the existing holes, dissipating their energy to the lattice. The recombination times strongly depend on the density of trapped states.

[4] The density of states of a bulk crystal is proportional to the effective mass of the carriers and is defined as follows:

$$D(E) = \frac{(2m^*)^{3/2}}{2\pi^2\hbar^3}\sqrt{E}\ .$$

With the effective mass of the light holes of $m_{\mathrm{lh}}^* = 0.026 \cdot m_0$, the relative density of states between the heavy and the light holes is

$$\frac{D_{\mathrm{hh}}(E)}{D_{\mathrm{lh}}(E)} = \left(\frac{m_{\mathrm{hh}}}{m_{\mathrm{lh}}}\right)^{3/2} \approx 60\ .$$

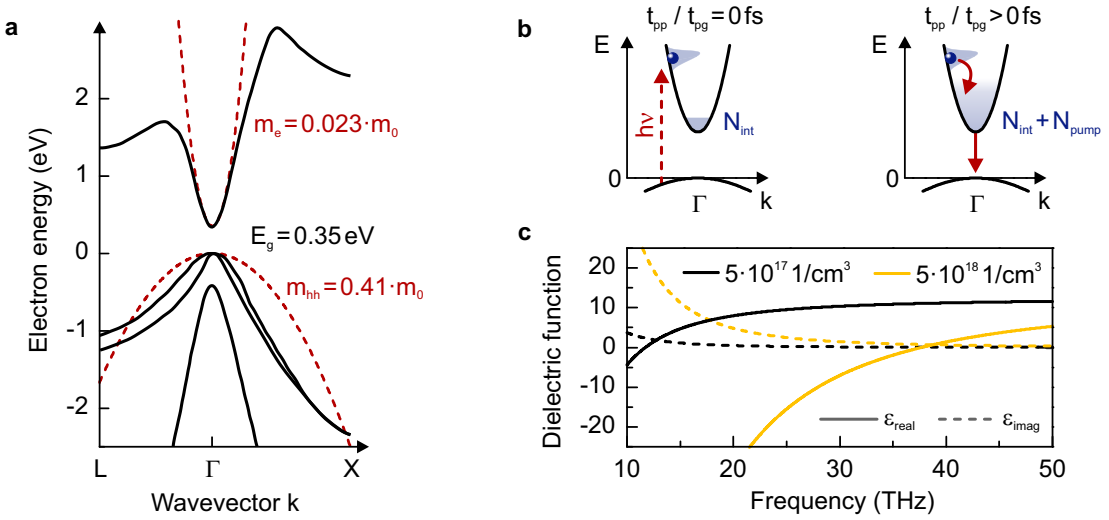

Figure 3.7 | Optical properties of indium arsenide. **a**, Calculated band structure of InAs along the $\Gamma - \mathrm{L}$ and the $\Gamma - \mathrm{X}$ directions [Saï08], featuring a direct band gap with $E_{\mathrm{gap}} = 0.35\,\mathrm{eV}$. The curvatures of the heavy-hole and the conduction bands at the Γ-point are indicated by the red dashed curves. From the curvature of the bands the effective mass of the electrons $m_{\mathrm{e}}^* = 0.023 \cdot m_0$ and the heavy holes $m_{\mathrm{hh}}^* = 0.41 \cdot m_0$ can be deduced with respect to the free electron mass m_0. **b**, Illustration of the carrier injection and recombination process. Upon photoexcitation ($t_{\mathrm{pp}} = 0\,\mathrm{fs}$ or $t_{\mathrm{pg}} = 0\,\mathrm{fs}$) carriers are promoted into the conduction band by the ultrafast near-infrared pump pulse. Hence, the total carrier concentration N_{c} is composed of the intrinsic N_{int} and the pump-induced carrier density N_{pump}. With evolving pump-probe delay time the hot electron gas thermalizes via electron-electron and electron-phonon scattering, followed by recombination, which leads to a decay of the carrier density towards the intrinsic electron concentration N_{int}. **c**, Dielectric functions of InAs calculated with the Drude model with a scattering rate $\gamma = 14\,\mathrm{THz}$ for carrier densities of $N_{\mathrm{c}} = 5 \cdot 10^{17}\,\mathrm{cm}^{-3}$ (black curves) and $N_{\mathrm{c}} = 5 \cdot 10^{18}\,\mathrm{cm}^{-3}$ (yellow curves). The solid and the dashed curves correspond to $\mathrm{Re}(\epsilon(\omega))$ and $\mathrm{Im}(\epsilon(\omega))$, respectively.

Surface recombination: Similar to the Shockley-Read-Hall recombination, carriers can also decay non-radiatively at the semiconductor surface via surface states created by dangling bonds and impurities. Reported values for InAs surfaces yield carrier decay times on the order of 30 to 1000 ps [Kan00, Joy13, Wag14b], strongly depending on the density of the surface states.

Auger recombination: Auger recombination is a non-radiative three particle process in which an electron and a hole recombine, transferring their energy to another electron. The excited electron subsequently dissipates the excess energy to the lattice via electron-phonon scattering. Since three particles are involved, Auger recombination is only relevant to the decay dynamics at high carrier densities. In InAs the Auger recombination coefficient is $A = 1.1 \cdot 10^{-26}\,\mathrm{cm}^6/\mathrm{s}$ [Vod92], yielding a recombination time of $\tau = 1/(A \cdot N_{\mathrm{c}}^2) \approx 4\,\mathrm{ps}$ for carrier densities of $N_{\mathrm{c}} = 5 \cdot 10^{18}\,\mathrm{cm}^{-3}$.

3.3.1 The Drude model

In analogy to the description of carriers in metals, the optical properties of the electrons and holes in a semiconductor can be described by the Drude model. In contrast to metals, even strongly doped semiconductors have carrier densities well below $10^{20}\,\mathrm{cm}^{-3}$. Hence, the characteristic plasma frequency is located in the far to mid-infrared wavelength region.

The Drude model is a classical approach for describing the response of carriers in metals to external fields. The charged particles are modeled as a gas of free carriers with zero average momentum [Dre02]. By applying a time-dependent electric driving field with a frequency $\omega = 2\pi\nu$, the carriers are forced into an oscillatory motion, which is characterized by the conductivity $\sigma(\omega)$

$$\sigma(\omega) = \frac{N_\mathrm{c} e^2 \tau}{m^*} \cdot \frac{1}{1 - i\omega\tau} \ , \tag{3.45}$$

with N_c being the carrier density and e and m^* the charge and the effective mass of the carriers, respectively. The Drude scattering time τ is associated with the average carrier scattering time. In the case of a semiconductor, the dielectric function can be derived from the conductivity by the following relation

$$\epsilon(\omega) = \epsilon_\infty + \frac{i\sigma(\omega)}{\epsilon_0 \omega} \ . \tag{3.46}$$

Here, ϵ_∞ is a constant, material-specific offset of the dielectric function which is modified by the presents of the free-carrier conductivity $\sigma(\omega)$. Using the definition of the Drude conductivity $\sigma(\omega)$, $\epsilon(\omega)$ can be rewritten as [Yu05]

$$\epsilon(\omega) = \epsilon_\infty \Big(1 - \frac{\omega_\mathrm{p}^2}{\omega^2 + i\gamma\omega}\Big) \ , \tag{3.47}$$

where the screened plasma frequency is defined as

$$\omega_\mathrm{p} = \sqrt{\frac{N_\mathrm{c} e^2}{m^* \epsilon_0 \epsilon_\infty}} \ , \tag{3.48}$$

and the carrier scattering rate γ is given by the inverse of the Drude relaxation time ($\gamma = 1/\tau$).

The real and imaginary part of $\epsilon(\omega)$ are

$$\mathrm{Re}(\epsilon(\omega)) = \epsilon_\infty\Big(1 - \frac{\omega_\mathrm{p}^2}{\omega^2+\gamma^2}\Big) \tag{3.49}$$

$$\mathrm{Im}(\epsilon(\omega)) = \epsilon_\infty\frac{\gamma}{\omega}\frac{\omega_\mathrm{p}^2}{\omega^2+\gamma^2}\ . \tag{3.50}$$

Importantly, $\mathrm{Re}(\epsilon(\omega))$ features a zero-crossing at the frequency ν_zero

$$\nu_\mathrm{zero} = \omega_\mathrm{zero}/2\pi = \sqrt{\omega_\mathrm{p}^2-\gamma^2}/2\pi\ , \tag{3.51}$$

which can be approximated to be $\nu_\mathrm{zero} \approx \omega_\mathrm{p}/2\pi$ for values of $\omega_\mathrm{p} \gg \gamma$. Hence, for oscillation frequencies of the electric field below the plasma frequency ($\nu < \omega_\mathrm{p}/2\pi$), $\mathrm{Re}(\epsilon(\omega))$ becomes negative and the semiconductor behaves like a metal, screening the external driving field inside the material. In contrast, for frequencies $\nu > \omega_\mathrm{p}/2\pi$ the material is partially transparent.

The derived dielectric function of InAs calculated by Equation 3.47 can be seen in Fig. 3.7c, using the high frequency permittivity of InAs of $\epsilon_\infty = 12.3$ [Mad04] as input parameter. The effective mass m^* is given by the reduced mass of the electron-hole plasma $\mu = (1/m_\mathrm{e}^* + 1/m_\mathrm{hh}^*)^{-1}$, with m_e^* and m_hh^* being the effective masses of the electrons and the heavy holes, respectively. Due to the relatively high effective mass of the heavy holes, μ can be approximated by the effective mass of the electrons in the conduction band $\mu \approx m_\mathrm{e}^* = 0.023 \cdot m_0$. The scattering rate is set to $\gamma = 14\,\mathrm{THz}$, which corresponds to a carrier scattering time of $\tau \approx 70\,\mathrm{fs}$. The real part (solid curve) and imaginary part (dashed curve) of the calculated dielectric function are shown for electron densities of $N_\mathrm{c} = 5 \cdot 10^{17}\,\mathrm{cm}^{-3}$ (black curve) and $N_\mathrm{c} = 5 \cdot 10^{18}\,\mathrm{cm}^{-3}$ (yellow curve). With increasing carrier density the zero-crossing of $\mathrm{Re}(\epsilon(\omega))$ blue-shifts from $\nu_\mathrm{zero} \approx 12\,\mathrm{THz}$ at $N_\mathrm{c} = 5 \cdot 10^{17}\,\mathrm{cm}^{-3}$ to $\nu_\mathrm{zero} \approx 38\,\mathrm{THz}$ at $N_\mathrm{c} = 5 \cdot 10^{18}\,\mathrm{cm}^{-3}$.

The fingerprint of the plasma frequency

The Drude model is now used to study the influence of the photoexcited InAs sample on the scattered electric field as a function of frequency ν (see Equation 3.21). As has already been seen in Section 3.2.5, the zero-crossing of the real part of the sample dielectric function should have a significant impact on the scattered amplitude and phase, due to the appearance of the near-field resonance. This is simulated by approximating the broadband multi-THz probe pulses with a Gaussian-shaped spectrum $|\tilde{E}_\mathrm{in}|$ with a center frequency of 30 THz (FWHM bandwidth of 10 THz) and a constant phase $\phi_\mathrm{in} = 0\,\mathrm{rad}$. In the first graph in Fig. 3.8a (1), the calculated amplitude (gray shaded area) and phase

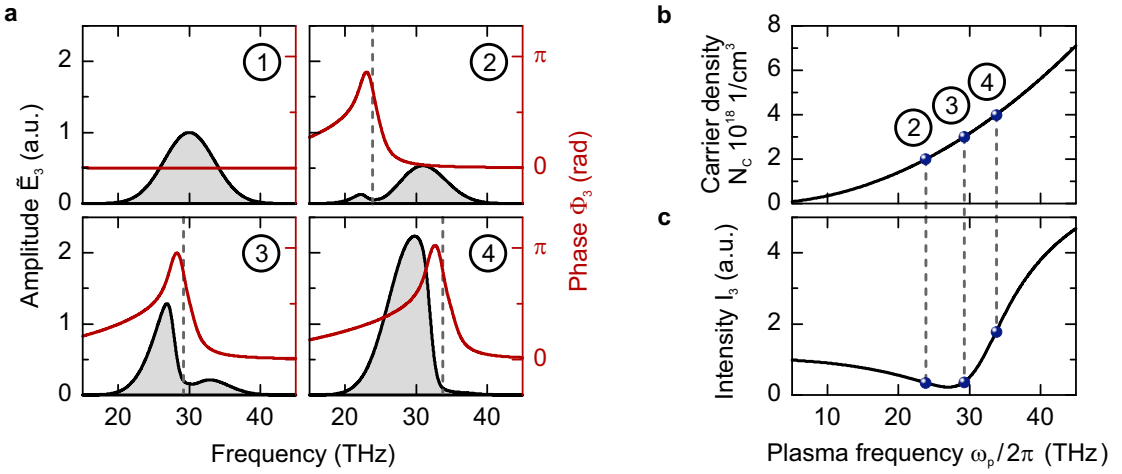

Figure 3.8 | Scattering response of indium arsenide. **a**, Theoretical simulation of the amplitude $\tilde{E}_3$ (gray shaded area) and phase ϕ_3 (red curve) scattered off an InAs sample. A Gaussian-shaped spectrum with a center frequency of 30 THz and a FWHM bandwidth of 10 THz is used as an input spectrum. The calculations are performed with a carrier density of $N_c = 5 \cdot 10^{16}\,\mathrm{cm}^{-3}$ for the first image (1), $N_c = 2 \cdot 10^{18}\,\mathrm{cm}^{-3}$ for (2), $N_c = 3 \cdot 10^{18}\,\mathrm{cm}^{-3}$ for (3) and $N_c = 4 \cdot 10^{18}\,\mathrm{cm}^{-3}$ for (4). The position of the corresponding plasma frequency of the electrons in the conduction band is indicated in each plot by the gray dashed line. **b**, Carrier density as a function of plasma frequency for InAs. The blue dots correspond to the values of the carrier densities in **a**. **c**, Spectrally integrated intensity I_3 as a function of plasma frequency. The blue dots indicate the scattered intensity corresponding to the scattered spectra in **a**. For all calculations, the Drude scattering rate is set constant to $\gamma = 14\,\mathrm{THz}$.

(red curve) of the electric field scattered off an InAs sample measured at the third demodulation order are shown, assuming an electron density of $N_c = 5 \cdot 10^{16}\,\mathrm{cm}^{-3}$. The corresponding plasma frequency is $\omega_p/2\pi \approx 4\,\mathrm{THz}$, which barely influences the scattered spectrum in the mid-infrared. This situation changes with increasing carrier density. At $N_c = 2 \cdot 10^{18}\,\mathrm{cm}^{-3}$ (Fig. 3.8a (2)), an overall reduction of the scattered amplitude for all frequency components is observed. Additionally, a clear dip in the amplitude spectrum appears at $\nu = 24.1\,\mathrm{THz}$, which is close to the plasma frequency (gray dashed line) that is positioned at $\omega_p/2\pi = 23.8\,\mathrm{THz}$. The dip is attributed to the near-field resonance, which is also apparent in the phase of the scattered spectrum. Approaching the plasma frequency, the phase increases to a maximum value of $\phi = 2.7\,\mathrm{rad}$ at $\nu = 23\,\mathrm{THz}$, followed by a decrease towards $\phi = 0\,\mathrm{rad}$. For carrier densities of $N_c = 3 \cdot 10^{18}\,\mathrm{cm}^{-3}$ and $N_c = 4 \cdot 10^{18}\,\mathrm{cm}^{-3}$, the dip and the phase change shift to higher frequencies, as can be seen in Fig. 3.8a (3) and (4), respectively. The scattering efficiency is visibly enhanced for frequencies $\nu < \omega_p/2\pi$, leading to a significant increase of the entire scattered spec-

trum for plasma frequencies exceeding the maximum frequency component of the input pulse-spectrum. All spectra are calculated with a Drude scattering rate of $\gamma = 14\,\mathrm{THz}$. The scattering rate mainly influences the width of the resonance, leading to a broadening with increasing γ. In addition, the enhancement of the scattered amplitude below $\omega_\mathrm{p}/2\pi$ is reduced for larger Drude scattering rates. This effect is also visible in Fig. 3.6a as a function of imaginary part of the sample dielectric function. In Fig. 3.8b, the carrier density as a function of plasma frequency is shown, with the carrier densities corresponding to the images in Fig. 3.8a indicated by blue dots.

To investigate the effects of carrier injection on the spectrally integrated scattered intensity, I_3 is calculated (see Equation 3.29) as a function of the plasma frequency ω_p using the same input spectrum as in Fig. 3.8a. The results can be seen in Fig. 3.8c, where the scattered intensity I_3 is normalized to the value at $\omega_\mathrm{p} = 0$. As the plasma frequency shifts into the bandwidth of the input spectrum, the integrated scattered intensity drops, reaching a minimum of 0.2 at $\omega_\mathrm{p}/2\pi = 27\,\mathrm{THz}$, which is close to the center frequency of the input spectrum. As the plasma frequency traverses the spectrum towards higher frequencies, the scattered intensity increases such that it exceeds a value of 3.8 at $\omega_\mathrm{p}/2\pi > 40\,\mathrm{THz}$. The plasma frequency yielding the minimum scattered intensity is phenomenologically linked to the center frequency of the input spectrum. Hence, the spectrally integrated pump-probe dynamics can vary distinctly for different probing spectra: For probe pulses with center frequencies above the maximum pump-induced plasma frequency of the sample, the scattered intensity dynamics feature only a transient attenuation. In contrast, for probe pulses with center frequencies well below the maximum pump-induced plasma frequency, an enhancement of I_3 is observed, followed by an attenuation as the plasma frequency decays through the probe-pulse spectrum to its equilibrium value.

Comparing the simulated scattered intensity to the measured pump-probe dynamics on bulk InAs (Fig. 3.1b), the observed enhancement and attenuation of I_3 for $t_\mathrm{pp} > 150\,\mathrm{fs}$ can now be understood to be the results of the plasma frequency shifting through the spectrum due to the decay of the carrier density.

3.3.2 Modeling of the experimental results of bulk indium arsenide

To corroborate the assumption that there is a transient plasma frequency within the bandwidth of the multi-THz probe pulses, the scattered amplitudes and phases of I_3 measured on InAs as a function of pump-probe delay time are directly simulated by the point dipole model (see Equation 3.43) using a sample dielectric function given by the Drude model. The scattered amplitude and phase at negative pump-probe delay times (depicted in Fig. 3.2) are used as input parameters for the simulation, as described in Section 3.2.

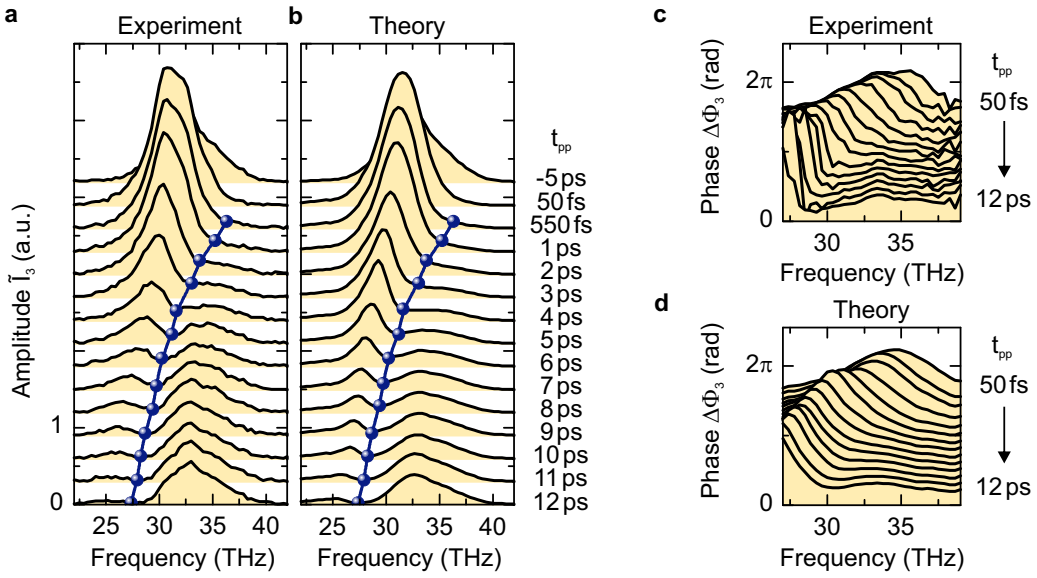

Figure 3.9 | Modeling the pump-probe dynamics of bulk indium arsenide. **a**, Scattered amplitude spectrum $\tilde{I}_3$ measured as a function of pump-probe delay time t_{pp} by nano-FTIR. **b**, Amplitude progression simulated using the point-dipole model and a sample dielectric function defined by the Drude model. Only the carrier density N_{c} and the scattering rate γ of the sample are used as fit parameters. The blue dots indicate the local minimum ν_0 which is related to the plasma frequency that shifts through the probe pulse spectrum with evolving t_{pp}. **c**, Relative phase measured by pump-probe FTIR spectroscopy. **d**, Phases simulated using the point-dipole model and the same parameters as in the corresponding amplitude spectra in **b**. The experimental spectra are measured with a tip-tapping amplitude of 130 nm and a pump fluence of 1.1 mJ/cm^2.

In Fig. 3.9a and b, the experimentally measured and theoretically calculated amplitude spectra $\tilde{I}_3(\nu)$ are shown as a function of pump-probe delay time t_{pp}, respectively. The strength of the scattered amplitude as well as the position of the observed resonance are nicely reproduced by the model for all pump-probe delay times. The corresponding relative phases of the experiment are shown in Fig. 3.9c, as are the calculated relative phases extracted from the point-dipole model (Fig. 3.9d), using the same parameters as in the corresponding amplitude spectra in Fig. 3.9b. Remarkably, the excellent agreement between experiment and theory is achieved using only the carrier density N_{c} and the Drude scattering rate γ as fitting parameters. From the theoretical calculations, the dip in the amplitude spectrum can now be related to the position of the plasma frequency of the carriers in the sample, which is directly proportional to the square root of the local carrier density. Following photoexcitation, the carrier population decays and the plasma frequency shifts to lower frequencies as t_{pp} evolves.

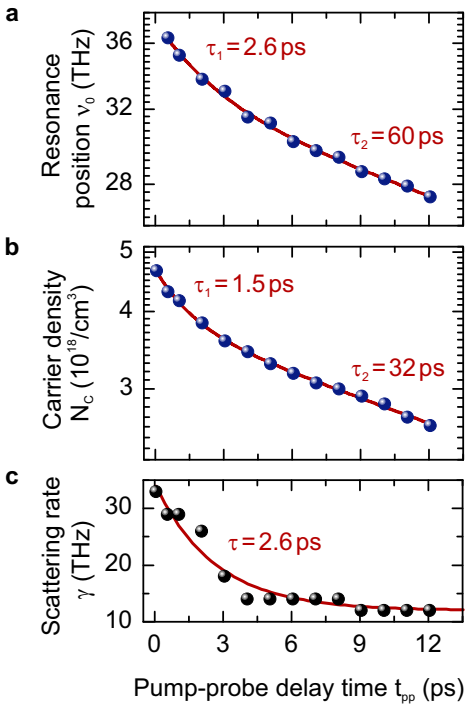

Figure 3.10 | Carrier dynamics at the surface of bulk indium arsenide. a, Resonance position ν_0 as a function of pump-probe delay time t_{pp} (blue dots), extracted from the scattered amplitude spectra $\tilde{I}_3$ in Fig. 3.9a. The decay is plotted on a semi-logarithmic scale and is fit by a bi-exponential decay (red curve) of the resonance position with a fast decay time of $\tau_1 = 2.6\,\mathrm{ps}$, followed by a slower decay time of $\tau_2 = 60\,\mathrm{ps}$. **b**, Carrier density N_c as a function of t_{pp} extracted from the point-dipole model (blue dots). Similar to **a**, a bi-exponential decay (red curve) is seen with a fast decay time of $\tau_1 = 1.5\,\mathrm{ps}$ and a slower decay time $\tau_2 = 32\,\mathrm{ps}$ for $t_{\mathrm{pp}} > 1.5\,\mathrm{ps}$. **c**, Drude scattering rate γ extracted from the point-dipole model. Following photoexcitation, the scattering rate of the hot electron gas relaxes within $\tau = 2.6\,\mathrm{ps}$.

To investigate the decay dynamics of the carriers, the time-dependent resonance position (blue dots in Fig. 3.9a) is extracted from the experimental data and plotted on a semi-logarithmic scale as a function of t_{pp} (see Fig. 3.10a). A bi-exponential decay is observed and the dynamics can be fitted by

$$\nu_0(t_{\mathrm{pp}}) = 4.7\,\mathrm{THz} \cdot \mathrm{e}^{-t_{\mathrm{pp}}/2.6\,\mathrm{ps}} + 29.7\,\mathrm{THz} \cdot \mathrm{e}^{-t_{\mathrm{pp}}/60\,\mathrm{ps}} + 3\,\mathrm{THz}\,. \tag{3.52}$$

Here, the constant offset of 3 THz corresponds to the plasma frequency of the intrinsic carrier concentration of $3 \cdot 10^{16}\,\mathrm{cm}^{-3}$, which was supplied by the manufacturer. The decay of the plasma frequency is governed by an initial fast response with a decay constant of $\tau_1 = 2.6 \pm 0.8\,\mathrm{ps}$ and a slower response with a decay time of $\tau_2 = 60 \pm 11\,\mathrm{ps}$. The same behavior is also observed in the decay of the carrier density, which is extracted from point-dipole model (Fig. 3.10b). Here, the bi-exponential fit results in

$$N_\mathrm{c}(t_{\mathrm{pp}}) = 8.5 \cdot 10^{17}\,\mathrm{cm}^{-3} \cdot \mathrm{e}^{-t_{\mathrm{pp}}/1.5\,\mathrm{ps}} + 3.8 \cdot 10^{18}\,\mathrm{cm}^{-3} \cdot \mathrm{e}^{-t_{\mathrm{pp}}/32\,\mathrm{ps}} + 3 \cdot 10^{16}\,\mathrm{cm}^{-3}\,, \tag{3.53}$$

featuring a fast carrier decay time of $\tau_1 = 1.5 \pm 0.2\,\mathrm{ps}$ and a slower decay time of $\tau_2 = 32 \pm 1.7\,\mathrm{ps}$. Hence, within the uncertainties, the decay times of the carrier density correspond to half the decay times of the plasma frequency. This is expected from the definition of the plasma frequency $\omega_\mathrm{p} \propto \sqrt{N_\mathrm{c}}$ (see Equation 3.48), which relates the

decay times corresponding to the resonance position τ_{ν_0} and the carrier density τ_{N_c} by $e^{-t/\tau_{\nu_0}} = e^{-t/(2\tau_{N_c})}$.

The fast decay of the carrier density ($\tau_1 = 1.5\,\mathrm{ps}$) is attributed to electron trapping into surface states. For $t_{pp} > 1.5\,\mathrm{ps}$, the trapped states saturate [Jep01, Van14], leading to a slow-down of the carrier dynamics and hence an increase of the decay time to $\tau_2 = 32\,\mathrm{ps}$. In this regime, the reduction of the carrier density is mainly determined by non-radiative surface recombination or Shockley-Read-Hall recombination. However, since near-field microscopy is most sensitive to the surface of the investigated material, surface recombination is most likely the relevant decay channel [Wag14b]. In addition to the carrier density, the Drude scattering rate can also be extracted from the model. Upon photoexcitation, a hot electron gas is generated, leading to an increase of the Drude scattering rate to $\gamma = 34\,\mathrm{THz}$. With evolving t_{pp}, the electrons cool via electron-phonon interactions, reducing the scattering rate to $\gamma = 12\,\mathrm{THz}$, as can be seen in Fig. 3.10c. The decay of γ is approximated by an exponential fit

$$\gamma(t_{pp}) = 22.5\,\mathrm{THz} \cdot e^{-t_{pp}/2.6\,\mathrm{ps}} + 12\,\mathrm{THz}\ , \tag{3.54}$$

resulting in a decay time of $2.6 \pm 0.3\,\mathrm{ps}$, which is comparable to values reported in literature [Wag14b].

3.4 Field-resolved observation of local electron dynamics within a single indium arsenide nanowire

The comprehensive understanding of the pump-probe dynamics observed on bulk InAs can now be used to investigate the local carrier dynamics within single InAs nanowires on the sub-cycle timescale. Nanowires based on III–V semiconductors are regarded as future building blocks in electronics and optoelectronics and already operate as efficient terahertz sources [Sel11], active elements in field effect transistors [Vit12] and nanoscale, near-infrared laser [Sax13, May13]. The ongoing development of such nanowire-based devices requires a deep understanding of their femtosecond carrier dynamics and surface charge distributions on the nanoscale.

The InAs nanowires[5] investigated here were grown bottom-up on InAs (111)B substrates by chemical beam epitaxy using gold particles as a growth catalyst. The extrinsic carrier density is $N_c \approx 2 \cdot 10^{17}\,\mathrm{cm}^{-3}$ and results from strong selenium background doping. After growth, the nanowires were transferred to a diamond substrate, which features no phonon

[5] The InAs nanowires have been provided by the group of Miriam S. Vitiello, NEST, CNR-Istituto Nanoscienze and Scuola Normale Superiore, 56127 Pisa, Italy.

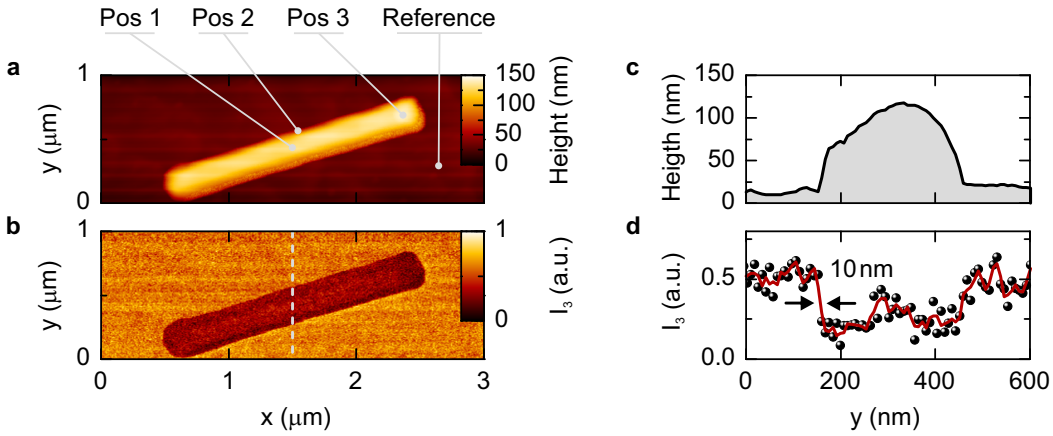

Figure 3.11 | Near-field imaging of a single indium arsenide nanowire. a, Topography of the InAs nanowire placed on a diamond substrate, measured by the AFM. **b**, Scattered multi-THz near-field intensity I_3 as a function of position. A clear contrast between the InAs nanowire and the diamond substrate is observed. The gray dashed line indicates the x-position of the line-scan shown in **c** and **d**. **c**, Topography of the line-scan over the InAs nanowire with a maximum height of approximately 120 nm. **d**, Corresponding scattered intensity (black dots) with a smoothed guide to the eye superimposed (red curve). Black arrows indicate the position of the 10-nm wide edge at the onset of the nanowire. All measurements are performed at a tapping amplitude of 130 nm.

or electron resonances in the mid-infrared that could complicate the interpretation of the scattered near-field response. In particular, the large band-gap of diamond (5.5 eV) compared to the pump-photon energy ($E_{\mathrm{photon}} = 0.78\,\mathrm{eV}$) prevents carrier injection into the substrate. An AFM scan of the particular nanowire investigated here is shown in Fig. 3.11a. The hexagonally-shaped nanowire has a length of approximately 2 µm with a maximum height of 140 nm. While the topography is measured, the scattered multi-THz near-field intensity I_3 of the unpumped nanowire is simultaneously recorded as a function of position, which can be seen in Fig. 3.11b. Here, a clear contrast between the nanowire and the diamond substrate is observed, which results from a larger multi-THz scattering efficiency on the diamond substrate than on the InAs nanowire. This high contrast can be exploited to quantify the spatial resolution of our microscope by performing a line scan across the center of the nanowire. The measured topography and the corresponding near-field intensity I_3 are depicted in Fig. 3.11c and d, respectively. The exact x-position of the line scan is indicated as gray dashed line in Fig. 3.11b. At the edge of the nanowire ($y = 160\,\mathrm{nm}$), I_3 features a sharp decrease, highlighted by the black arrows, from which a spatial resolution of 10 nm is deduced.

In addition to the spatially-resolved steady-state response of I_3 on the nanowire, shown in Fig. 3.11b, intensity-resolved pump-probe microscopy is employed to record near-field

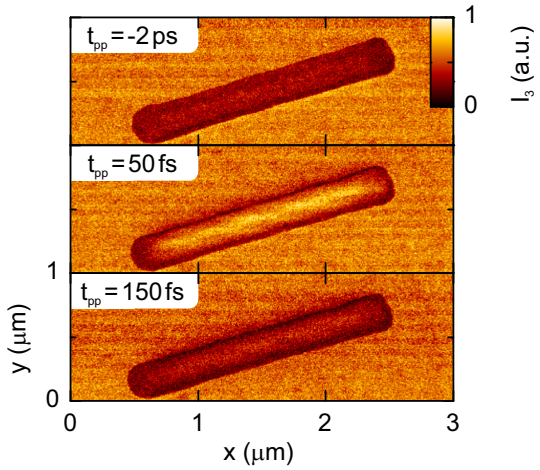

Figure 3.12 | Ultrafast movie. Near-field images of the InAs nanowire at different pump-probe delay times. Upon photoexcitation ($t_{\mathrm{pp}} = 50\,\mathrm{fs}$), free carriers are excited into the conduction band leading to a significant increase of the scattered intensity I_3 along the central axis of the nanowire. The enhanced scattering is short-lived: At $t_{\mathrm{pp}} = 150\,\mathrm{fs}$ the near-field image of the nanowire has already dimmed significantly, pointing towards carrier decay times below 100 fs. All measurements are performed with a tip-tapping amplitude of 130 nm and a pump fluence of $1.0\,\mathrm{mJ/cm^2}$.

images as a function of the relative arrival time (t_{pp}) between the near-infrared pump and multi-THz probe pulses at the sample (see Fig. 3.12). Following ultrafast photoinjection of free carriers by the 22-fs near-infrared pump pulses, the scattering efficiency from the central axis of the nanowire is strongly enhanced ($t_{\mathrm{pp}} = 50\,\mathrm{fs}$). However, in contrast to the case of bulk InAs measurements, this increased scattering is short-lived: At $t_{\mathrm{pp}} = 150\,\mathrm{fs}$ the nanowire has already dimmed significantly, indicating the existence of electron dynamics with decay times below 100 fs. The observed inhomogeneities of the pump-induced near-field signals at the nanowire surface are representative of local differences in the dielectric function, highlighting the fundamental new insights into the carrier dynamics of nanostructures that can be gained by time-resolved near-field microscopy.

To investigate the full evolution of the scattered intensity I_3 as a function of t_{pp}, pump-probe traces are recorded at specific positions on the nanowire, which are identified in Fig. 3.11a. As already inferred from the near-field images in Fig. 3.12, the dynamics strongly dependent on the exact position of the tip (Fig. 3.13). In the center of the nanowire (Position 1), $I_3(t_{\mathrm{pp}})$ is characterized by a large peak at $t_{\mathrm{pp}} = 50\,\mathrm{fs}$ with a resolution-limited rise time of approximately 60 fs. The peak is followed by a decay with two distinct time constants. The first decay occurs over approximately 100 fs, which is close to the time resolution of the pump-probe intensity measurements of $\geq 60\,\mathrm{fs}$, given by the probe pulse duration. The ultrafast decay is then followed by a slower decay time on the order of a few ps. In contrast to the center position, the extremities of the nanowire feature a substantially reduced peak height (Positions 2 and 3). However, the initial sub-100-fs decay is visible at all positions on the nanowire. To exclude any influence of the substrate on the observed dynamics, a pump-probe trace $I_3(t_{\mathrm{pp}})$ is recorded on diamond (Reference position), featuring no pump-induced response.

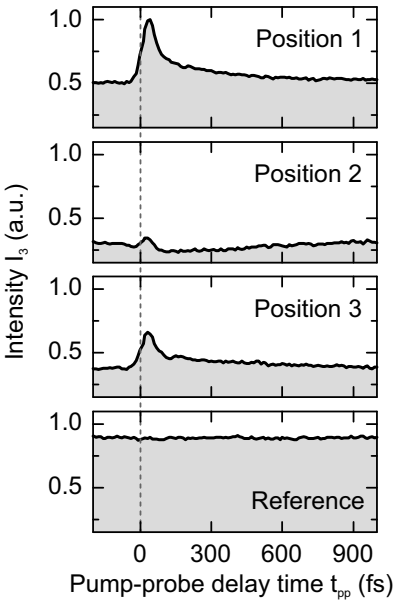

Figure 3.13 | Pump-probe dynamics. Pump-probe traces of the scattered intensity I_3, measured at the positions on the nanowire surface indicated in Fig. 3.11a. At Position 1, I_3 features a sharp increase at the pump-probe delay time $t_{\mathrm{pp}} = 0\,\mathrm{fs}$ (gray dashed line), with a rise time of approximately 60 fs. In contrast, the extremities of the nanowire (Position 2 and 3) feature a substantially reduced peak height. No pump-probe dynamics are observed on the diamond substrate (Reference position). All measurements are performed with a tip-tapping amplitude of 130 nm and a pump fluence of $1.0\,\mathrm{mJ/cm^2}$.

The similarities between the observed pump-probe dynamics on the InAs nanowire and the InAs bulk crystal suggests that the pump-induced carrier density in the nanowire leads to a shift of the plasma frequency up to the high-frequency edge of the multi-THz probe pulse spectrum (peak). Decay of the free carrier population subsequently reduces the plasma frequency, and with it the scattered intensity I_3. The initial decay of $I_3(t_{\mathrm{pp}})$ within less than 100 fs is of particular interest, since it is much faster than typical carrier recombination times in semiconductors (see Section 3.3) and is not observed in the measurements performed on bulk InAs. To extract quantitative information regarding the carrier densities and their dynamics, two-time THz spectroscopy (see Section 2.3) is performed to resolve the carrier decay with the ultimate, sub-cycle temporal resolution (10 fs in our experiment).

3.4.1 Two-time THz spectroscopy with nanometer spatial resolution

To perform two-time THz spectroscopy, the tip is placed on the center of the unpumped nanowire (Position 1 in Fig. 3.11a) and the scattered multi-THz radiation is detected by electro-optic sampling at the third order sideband $f_{\mathrm{EOM},O3} = 20\,\mathrm{MHz} + 3 \cdot \Omega_{\mathrm{tip}}$ (see Section 2.4.1). Fig. 3.14a shows the scattered electric near field E_3 (red curve, $\times 5000$ magnification factor) together with a reference waveform (black curve), measured by EOS at a lock-in frequency of 20 MHz. It has to be emphasized that the near-field signals at the third demodulation order measured on the InAs nanowire correspond to less than 50

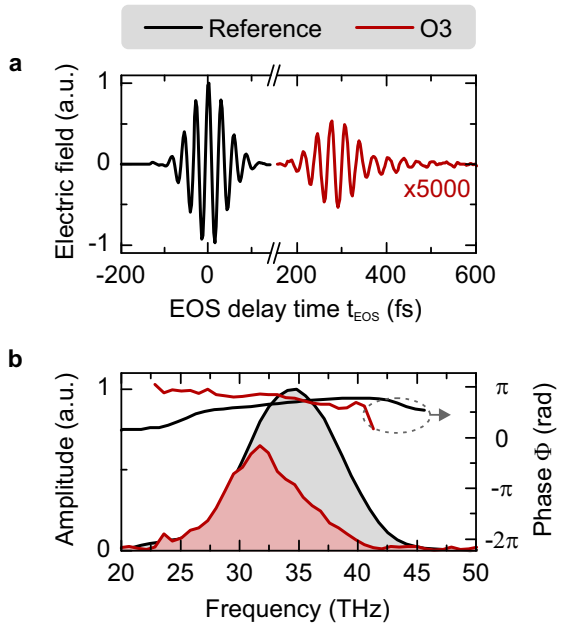

Figure 3.14 | Field-resolved detection of the radiation scattered off the center of the indium arsenide nanowire. **a**, Reference waveform (black curve) of the multi-THz radiation measured at a lock-in frequency of $f_{\mathrm{EOM}} = 20\,\mathrm{MHz}$. The near field (red curve, $\times 5000$ magnification factor) scattered off the center of the nanowire (Position 1 in Fig. 3.11a) is measured at the third order sideband $f_{\mathrm{EOM},O3} = 20\,\mathrm{MHz} + 3 \cdot \Omega_{\mathrm{tip}}$. Here, the scattered multi-THz waveform corresponds to less than 50 photons per pulse. **b**, Absolute phases (solid curves) and amplitude spectra (shaded areas) of the reference pulse (black) and the scattered pulse (red). The measurements are performed at a tapping amplitude of 130 nm.

photons per multi-THz pulse. These waveforms are only detectable due to the excellent stability of the experimental setup and the low noise background of the differential lock-in detection at the Nyquist-frequency of the laser system. The absolute phases and the amplitude spectra of the reference (black) and the scattered waveforms (red) calculated by Fourier transformation are plotted in Fig. 3.14b. Here, an antenna-like tip response reduces the scattering efficiency for frequencies larger than 31 THz. As a consequence, the bandwidth of the scattered radiation is reduced compared to the Gaussian-shaped input spectrum, consequently stretching the scattered pulses in time, as can be seen in Fig. 3.14a. The absolute phase of the scattered radiation, however, follows the flat phase of the reference pulses closely.

Using two-time terahertz spectroscopy, it is now possible to ascertain the temporal evolution of the local dielectric function upon photoexcitation over timescales shorter than a single oscillation cycle of the multi-THz probe pulses. An effective waveform scattered off the photoexcited nanowire is recorded by scanning the terahertz-gate delay t_{EOS} while keeping the pump-gate delay t_{pg} fixed (see Section 2.3). The waveform scattered at negative pump-gate delay times ($t_{\mathrm{pg}} = -5\,\mathrm{ps}$) can be seen in Fig. 3.15a. The visible trailing oscillations in the near-field transient for $t_{\mathrm{EOS}} > 50\,\mathrm{fs}$, are completely suppressed upon carrier injection ($t_{\mathrm{pg}} = 0\,\mathrm{fs}$), as can be seen by the black curve in Fig. 3.15b. With evolving t_{pg} the trailing oscillations reappear and their oscillation period increases from approximately 30 fs at $t_{\mathrm{pg}} = 350\,\mathrm{fs}$ to 32 fs at $t_{\mathrm{pg}} = 750\,\mathrm{fs}$. These trailing oscillations are a characteristic fingerprint of a resonance within the multi-THz frequency spectrum:

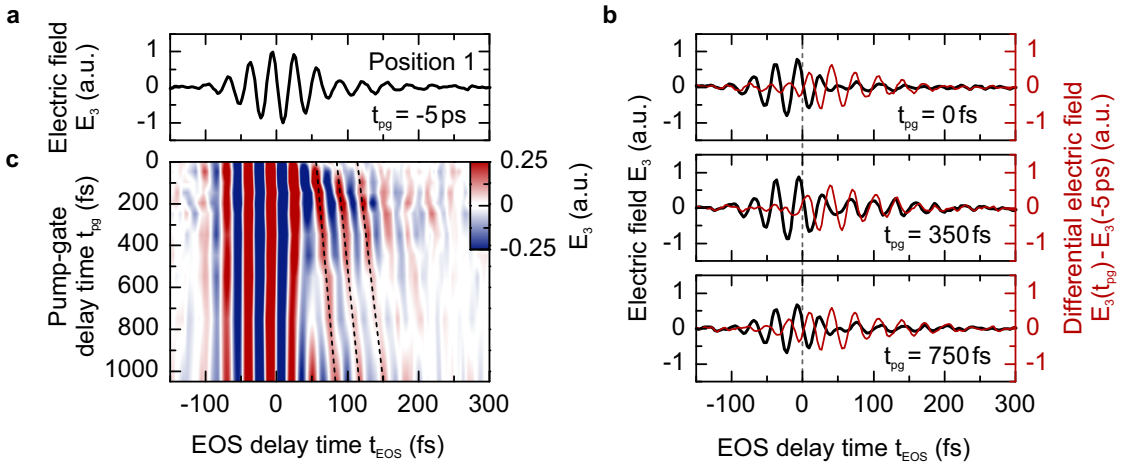

Figure 3.15 | Dynamics of the oscillating electric near field. **a**, Effective multi-THz waveform measured by EOS at the center of the nanowire (Position 1 in Fig. 3.11a) at negative pump-gate delay time $t_{\mathrm{pg}} = -5\,\mathrm{ps}$. **b**, Upon photoexcitation at $t_{\mathrm{pg}} = 0\,\mathrm{fs}$, the trailing oscillations of the scattered electric field are significantly altered for terahertz-gate delays $t_{\mathrm{EOS}} > 50\,\mathrm{fs}$. The change of the trailing oscillations hints towards the existence of a transient resonance within the multi-THz probe spectrum. The free induction decay of these resonances can be isolated by calculating the differential electric field $E_3(t_{\mathrm{pg}}) - E_3(-5\,\mathrm{ps})$ (red curves). **c**, Two-time THz spectroscopy map of the scattered electric near field at the center of the nanowire. Black dashed lines are guides to the eye, indicating the shift of the trailing oscillations to later times with increasing t_{pg}. For all data the pump fluence is $1.1\,\mathrm{mJ/cm^2}$ and the tapping amplitude is 130 nm.

The first few oscillation cycles of the multi-THz probe field start to drive an existing resonance by coupling to its dipole moment. The excited, oscillating dipoles subsequently decay while emitting coherent radiation at precisely their eigenfrequency. This free induction decay can be isolated from the measured waveforms by calculating the differential electric field $E_3(t_{\mathrm{pg}}) - E_3(-5\,\mathrm{ps})$, shown by the red curves in Fig. 3.15b. The full evolution of the scattered electric field as a function of t_{pg} is compiled in a two-time THz spectroscopy map in Fig. 3.15c, which is recorded with a temporal resolution of 10 fs and a spatial resolution of 10 nm. Here, the trailing oscillations feature a clear shift to later times accompanied by a slow down of the oscillation period, as indicated by the black dashed lines.

3.4.2 Femtosecond carrier dynamics at the surface of a single indium arsenide nanowire

Field-resolved detection of the scattered terahertz waveforms provides access to both the absolute phase and amplitude in the frequency domain by Fourier transformation. Hence, the scattered amplitude spectra $\tilde{E}_3$ are extracted from the measured waveforms in Fig. 3.15c, and are depicted in Fig. 3.16a as a function of t_{pg}. The observed resonance in the time domain manifests itself as a dip in $\tilde{E}_3$ at the resonance position ν_0 (blue dots). This resonance is accompanied by a change in the phase at ν_0, as seen in Fig. 3.16c. With evolving t_{pg} the resonance shifts to lower frequencies, traversing the bandwidth of $\tilde{E}_3$ within a picosecond. The parameters of the experiment (tapping amplitude, pump fluence and spectral bandwidth of the multi-THz pulses) are identical to those used for pump-probe nano-FTIR performed on the InAs bulk crystal (see Section 3.3). As a consequence, the observed resonance position ν_0 is attributed to the plasma frequency ω_{p} of the photoexcited carriers in the InAs nanowire. This assumption of a bulk-like plasma resonance is further corroborated by the following observations: (i) no effects of the pump-induced dynamics on the nanowire size are observed; (ii) metallic tips are known to strongly couple to the local dielectric properties of the sample, being largely insensitive to size-dependent resonances. The scattered spectra are simulated using the point-dipole model and a nanowire dielectric function defined by the Drude model and the results of the simulations can be seen in Fig. 3.16b and d. Using only the carrier density N_{c} and the Drude scattering rate γ as free fitting parameters, the time evolution of both the amplitude and the absolute phase is reproduced[6].

To quantify the decay times of the observed dynamics, the resonance position ν_0 is extracted from the measured spectra and is plotted in Fig. 3.17a on a semi-logarithmic scale as a function of t_{pg}. The ν_0 dynamics are similar to those measured on bulk InAs, but on much faster timescales. The data is well-described by a bi-exponential decay

$$\nu_0(t_{\mathrm{pg}}) = 52\,\mathrm{THz} \cdot \mathrm{e}^{-t_{\mathrm{pg}}/40\,\mathrm{fs}} + 28.6\,\mathrm{THz} \cdot \mathrm{e}^{-t_{\mathrm{pg}}/3.5\,\mathrm{ps}} + 7.5\,\mathrm{THz}\ . \tag{3.55}$$

Here, the offset frequency of 7.5 THz corresponds to the plasma frequency of the extrinsic carrier concentration of $2 \cdot 10^{17}\,\mathrm{cm}^{-3}$, due to the selenium background doping of the nanowire. The first decay time of the resonance position is $\tau_1 = 40 \pm 10\,\mathrm{fs}$. This is followed by a slower decay ($\tau_2 = 3.5 \pm 0.3\,\mathrm{ps}$) that is comparable to the fast decay time measured on bulk InAs (see Fig. 3.10a). From the simulations, the carrier dynamics can

[6] Alternatively, the same behavior can be characterized by nano-FTIR, with a reduced time resolution (see Appendix B).

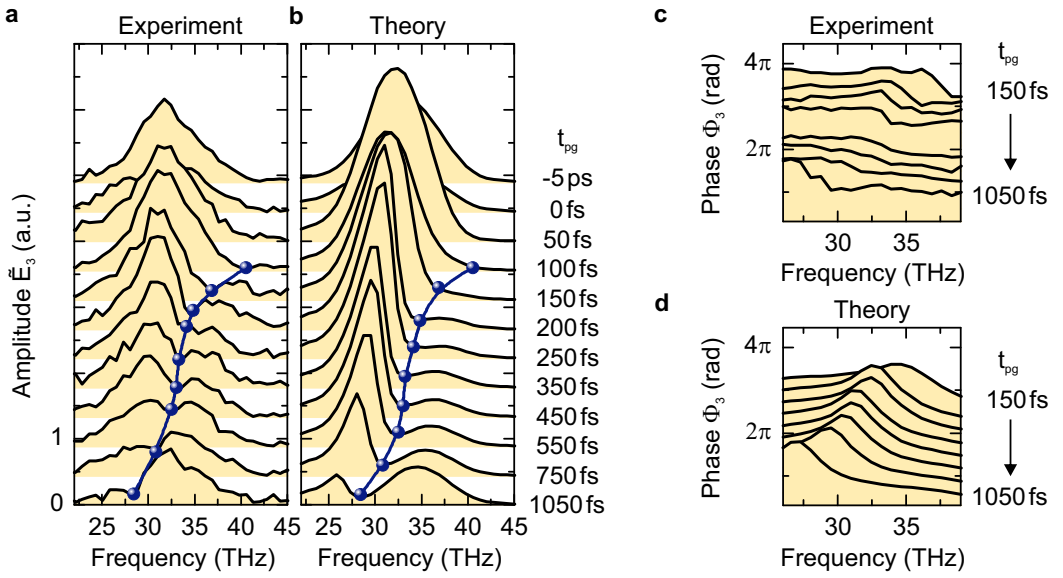

Figure 3.16 | Sub-cycle spectral dynamics. **a**, Amplitude spectra $\tilde{E}_3$ of the multi-THz waveforms shown in Fig. 3.15c, as a function of pump-gate delay time t_{pg}. The resonance position ν_0 is indicated by the blue dots. **b**, Simulated amplitude spectra using the point-dipole model and a nanowire dielectric function given by the Drude model. The simulations only depend on two parameters: The carrier density N_{c} and the Drude scattering rate γ. **c**, Absolute phases Φ_3 of scattered waveforms measured by EOS. A phase shift of approximately 2.5 rad is observed at the resonance position. **d**, Calculated phases extracted from the point-dipole model using the same parameters as in the corresponding amplitude spectra in **b**. For the experimental data, the pump fluence is 1.1 mJ/cm^2 and the tapping amplitude is 130 nm.

also be extracted (see Fig. 3.17b), and are consistent with a bi-exponential curve

$$N_{\mathrm{c}}(t_{\mathrm{pg}}) = 1.4 \cdot 10^{19}\,\mathrm{cm}^{-3} \cdot \mathrm{e}^{-t_{\mathrm{pg}}/20\,\mathrm{fs}} + 4.5 \cdot 10^{18}\,\mathrm{cm}^{-3} \cdot \mathrm{e}^{-t_{\mathrm{pg}}/1.7\,\mathrm{ps}} + 2 \cdot 10^{17}\,\mathrm{cm}^{-3}\ . \quad (3.56)$$

The decay time $\tau_1 = 20\,\mathrm{fs}$ is defined to be half the initial decay time of the resonance position as expected from the relation between the carrier density and the plasma frequency ($\nu_0 \approx \omega_{\mathrm{p}} \propto \sqrt{N_{\mathrm{c}}}$). The carrier densities weighting the exponentials and the second decay time are taken as free fitting parameters. The slower decay ($\tau_2 = 1.7 \pm 0.2\,\mathrm{ps}$) is comparable to the initial dynamics observed on bulk InAs and is therefore assigned to electron trapping into surface states. In contrast to bulk InAs, no saturation of the trapping dynamics is observed. This may be attributed to an increase of the surface state density due to stacking faults of the nanowire crystal structure during growth, the large concentration of selenium doping ions and the enhanced influence of the surface due to the high surface-to-volume ratio of the nanowires [Joy13]. The larger density of defect states

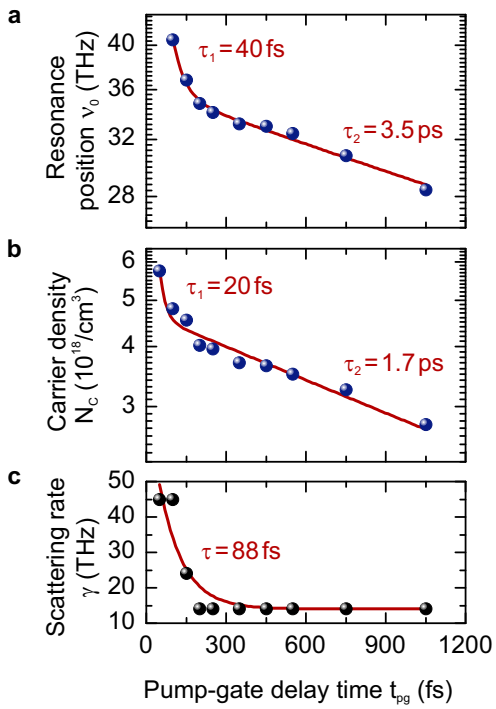

Figure 3.17 | Carrier dynamics on a single indium arsenide nanowire. **a**, Resonance position ν_0 as a function of pump-gate delay time t_{pg}, extracted from the scattered amplitude spectra in Fig. 3.16a and plotted on a semi-logarithmic scale. A bi-exponential decay of the resonance position is observed, featuring a fast decay time of $\tau_1 = 40\,\mathrm{fs}$, followed by a slower decay time of $\tau_2 = 3.5\,\mathrm{ps}$. **b**, Carrier density N_{c} as a function of t_{pg} extracted from the point-dipole model. Similar to **a**, a bi-exponential decay is retrieved. The fast decay time is defined to $\tau_1 = 20\,\mathrm{fs}$ followed by carrier trapping into surface states with a decay time of $\tau_2 = 1.7\,\mathrm{ps}$. **c**, Drude scattering rate γ extracted from the point-dipole model. The scattering rate of the hot electron gas is reduced within $\tau = 88\,\mathrm{fs}$ after photoexcitation due to carrier cooling.

might also be responsible for the observed carrier cooling dynamics shown in Fig. 3.17c. The decay of the Drude scattering rate can be fitted by

$$\gamma(t_{\mathrm{pg}}) = 61\,\mathrm{THz} \cdot \mathrm{e}^{-t_{\mathrm{pg}}/88\,\mathrm{fs}} + 14\,\mathrm{THz}\ . \tag{3.57}$$

After photoexcitation, a highly energetic electron gas is present, featuring a Drude scattering rate of $\gamma = 45\,\mathrm{THz}$ (at $t_{\mathrm{pg}} = 50\,\mathrm{fs}$). Within $\tau = 88 \pm 22\,\mathrm{fs}$, γ decays to 14 THz, which agrees with reported scattering rates for electrons in InAs nanowires [Joy13].

Still, the origin of the initial ultrafast dynamics of the carrier density remains unclear. Typical recombination times of carriers in semiconductors are on the picosecond timescale, which renders such decay channels unlikely. Even typical carrier cooling times are on the order of picoseconds, making the 88-fs decay of the scattering rate γ anomalously fast. To reveal the physical driving mechanism, responsible for the ultrafast carrier decay ($< 40\,\mathrm{fs}$) following photoexcitation, a new technique is developed, which is called **femtosecond tomography**.

3.5 Depletion layer formation at the surface of the indium arsenide nanowire

The confinement of the near field at the tip apex not only defines the spatial resolution of the s-NSOM on the sample surface, but also applies to the evanescent field extending from the near-field tip into the sample. Interestingly, the magnitude of the tapping amplitude in combination with lock-in detection at higher harmonics of the tapping frequency, determines the probing-depth sensitivity of the recorded signal, and thus the size of the probing volume. These findings[7] have already been exploited to perform steady-state near-field tomography, where gold structures covered with multiple 10 nm of transparent material [Tau05, Kru12, Eng13] or InAs quantum dots embedded in a thin host membrane [Jac12], have been visualized.

The probing-depth sensitivity can be quantified by recording retraction scans as a function of tapping amplitude. Here, the distance between the tip and the sample is gradually increased while the scattered intensity I_3 is simultaneously recorded. The decay of the normalized scattered intensity I_3 upon retraction from a gold sample is depicted in Fig. 3.18a. For a tapping amplitude of TA = 50 nm (black curve), I_3 drops exponentially with tip-sample distance, resulting in a $1/e$ decay length of approximately 15 nm. At a larger tapping amplitude (TA = 150 nm, red curve), the decay length increases to approximately 25 nm, indicating an increased sensitivity of the near-field signal to larger tip-sample distances. The full evolution of the decay length is shown in Fig. 3.18b (black dots), and features a linear increase (red dashed line) as a function of tapping amplitude. Similar to the free-space decay length, the penetration depth into the sample can be tuned with the tapping amplitude, and can be approximated by the free-space decay length divided by the refractive index of the sample. For InAs, this results in a probing depth ranging from 3 to 9 nm. However, it should be clarified, that the signals measured at larger probing depths are convoluted with the sample response originating from a shallower probing volume, making it difficult to quantify the absolute penetration depth. Nevertheless, by varying the tapping amplitude the relative probing depth can be changed by a factor of three.

To investigate the impact of the tapping amplitude on the observed dynamics, the pump-induced change of I_3 is investigated at Position 1 of the nanowire (see Fig. 3.11a) as a function of pump-probe delay time t_{pp} and tapping amplitude TA. All pump-probe traces are normalized to the baseline at a delay time of approximately -1 ps to compen-

[7] Note that steady-state near-field tomography can also be performed using a constant tapping amplitude and by recording the scattered intensity at different harmonic orders [Gov14]. For higher demodulation orders, the scattered signals originate from a more localized volume at the surface of the sample.

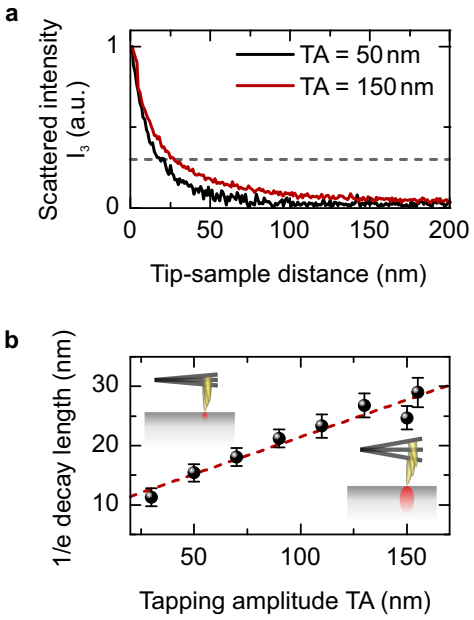

Figure 3.18 | Free-space decay of I_3. a, Normalized retraction scans of the scattered intensity I_3 measured as a function of tip-sample distance on a gold sample. For a tapping amplitude TA = 50 nm (black curve), I_3 decays within a $1/e$ decay length of approximately 15 nm. When the tapping amplitude is enlarged to TA = 150 nm (red curve), the free-space decay increases to a value of approximately 25 nm, indicating an enhanced sensitivity of the detected near-field signal to larger tip-sample distances. The gray dashed line corresponds to the $1/e$-decay value of the scattered intensity. **b**, Evolution of the free-space decay length as a function of tapping amplitude (black dots), featuring a linear increase (red dashed line). By tuning the tapping amplitude the probing depth can be varied by a factor of three.

sate for changes of the scattered intensity with tapping amplitude. As can be seen in Fig. 3.19a for TA = 50 nm (black curve), the scattered intensity I_3 increases within 60 fs (at t_{pp} = 0 fs, limited by the probe-pulse duration), followed by a decay with approximately the same time constant. While the fast initial decay can be seen for all tapping amplitudes, the strength of the subsequent dynamics for $t_{pp} > 150$ fs is strongly modified with increasing TA. This is most prominent for the pump-probe trace recorded with a tapping amplitude of TA = 130 nm (yellow curve). Interestingly, the scattered intensities of the pump-induced dynamics coincide at t_{pp} = 50 fs, indicating a homogeneous carrier distribution with depth directly after photoexcitation. However, the subsequent dynamics point towards distinctly different behavior of the electron population decay for large (deep probing) and small tapping amplitudes (shallow probing).

The observed difference in the dynamics for $t_{pp} > 150$ fs is of particular interest since a notable difference in the scattered amplitude spectrum should be observable as a function of TA. To this end nano-FTIR is employed to extract the position of the resonance frequency ν_0 as a function of tapping amplitude at a constant pump-probe delay time of t_{pp} = 300 fs (black dashed line in Fig. 3.19a), which is shown in Fig. 3.19b. For tapping amplitudes TA > 90 nm, the resonance positions (black dots) are located at approximately 32 to 33 THz. In contrast, at smaller tapping amplitudes, the resonance position significantly decreases from 31.5 THz at TA = 70 nm to 29.6 THz at TA = 40 nm suggesting the presence of a surface layer with reduced carrier density.

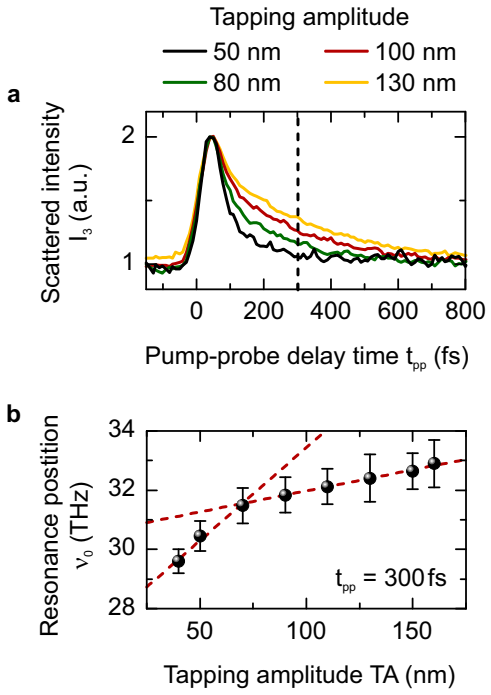

Figure 3.19 | Femtosecond tomography. **a**, Pump-induced change of the scattered intensity I_3 as a function of pump-probe delay time t_{pp} and tapping amplitude TA. All pump-probe traces are normalized to the baseline at negative delay times. **b**, Resonance position ν_0 (black dots) as a function of tapping amplitude, extracted from nano-FTIR measurements performed at a pump-probe delay time of $t_{\mathrm{pp}} = 300\,\mathrm{fs}$ (black dashed line in **a**). The red dashed lines are guides to the eye indicating the rapid change of the resonance position for small tapping amplitudes. For all measurements the pump fluence is $0.75\,\mathrm{mJ/cm^2}$.

This hypothesis is corroborated by Fig. 3.20a, wherein the scattered spectra $\tilde{I}_3$ for low (TA = 50 nm, red curve) and high tapping amplitudes (TA = 130 nm, black curve) are depicted for two distinct pump-probe delay times. At $t_{\mathrm{pp}} = 50\,\mathrm{fs}$, both spectra display a similar shape and feature a clear resonance within their spectrum. For TA = 50 nm and TA = 130 nm the resonance positions are located at approximately 34.6 THz (red dashed line) and 34.3 THz (black dashed line), respectively. This situation changes for $t_{\mathrm{pp}} = 250\,\mathrm{fs}$; here, the resonance position measured at TA = 50 nm (red dashed line) is shifted to a lower frequency (31.3 THz) relative to the measurements performed at larger tapping amplitudes (black dashed line, 32.7 THz). For a comprehensive picture, the full temporal evolution of ν_0 as a function of TA is shown in Fig. 3.20b. Following photoexcitation the resonance positions for both high (TA = 130 nm, black dots) and low tapping amplitudes (TA = 50 nm, red dots) agree within uncertainty. However, after only a few 10 fs, a separation of the resonance positions is observed, resulting in a constant reduction of ν_0 and hence the carrier density at the surface of the nanowire. Subsequent carrier trapping into surface states for $t_{\mathrm{pp}} > 200\,\mathrm{fs}$, reduces the resonance position for high and low tapping amplitudes with a decay time of approximately $3.7 \pm 0.4\,\mathrm{ps}$ (gray dashed lines).

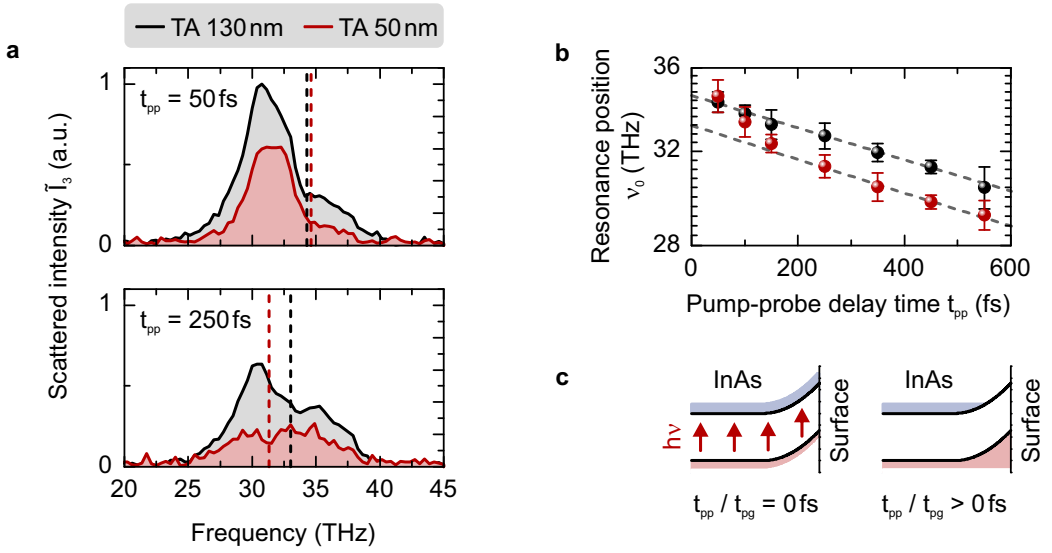

Figure 3.20 | Depletion layer formation at the surface of the indium arsenide nanowire. **a**, Scattered amplitude spectra $\tilde{I}_3$ for a tapping amplitude of TA = 130 nm (black curve) and TA = 50 nm (red curve), measured by nano-FTIR at a pump-probe delay time of $t_{pp} = 50$ fs (top) and $t_{pp} = 250$ fs (bottom). The resonance positions ν_0 for high and low tapping amplitudes are indicated by the black and red dashed lines, respectively. **b**, Full evolution of ν_0 as a function of t_{pp} recorded with a tapping amplitude of TA = 50 nm (red dots) and TA = 130 nm (black dots). The gray dashed lines correspond to the exponential decays of the resonance positions at $t_{pp} > 200$ fs with a decay time of 3.7 ps. Following photoexcitation ($t_{pp} = 50$ fs) the resonance positions for high and low tapping amplitudes coincide. However, within a few 10 fs a separation of the resonance position occurs. For $t_{pp} > 200$ fs, this effect leads to a constant reduction of the ν_0 at the surface (low TA) compared to larger probing depths (high TA). **c**, Illustration of the depletion layer formation. At $t_{pp} = 50$ fs or $t_{pg} = 50$ fs the photoexcited carrier density is homogeneously distributed within the nanowire. With evolving t_{pp} (t_{pg}), built-in fields lead to the acceleration of carriers away from the surface, resulting in an effectively reduced carrier density in the near-field probing volume. For all measurements the pump fluence is 0.75 mJ/cm^2.

The dynamics of ν_0 as a function of tapping amplitude (Fig. 3.20b) confirm that the fast initial decay (40 fs) of the resonance position measured by EOS (see Fig. 3.17) corresponds to the formation time of a surface depletion layer [Dek93], which is illustrated in Fig. 3.20c. Upon photoexcitation ($t_{\mathrm{pp}} = 50\,\mathrm{fs}$ or $t_{\mathrm{pg}} = 50\,\mathrm{fs}$), a homogeneous carrier distribution is created within the nanowire. Subsequent acceleration by a built-in surface field reduces the carrier density at the surface, such that the built-in field is compensated by the charged carrier redistribution. In the near-field measurements, this effect can be directly observed by an effective reduction of the plasma frequency, as the carriers are accelerated out of the near-field probing volume. After 40 fs the depletion layer is fully formed, leading to a 10 % difference in average carrier density between the probing volumes for low and high tapping amplitudes as inferred from the difference in ν_0 observed in Fig. 3.20b.

The observation of a surface depletion layer in InAs is rather surprising since donor-type surface states lead to a pinning of the Fermi level within the conduction band above the bulk Fermi energy. As a consequence, an electron accumulation layer is formed at the surface [Nog91, Can98, Pip06, Hal12, Joy13]. However, for degenerate doping, as is the case for the investigated nanowires, the bulk Fermi energy can exceed the pinned Fermi level at the surface. Hence, the band bending can be inverted, resulting in the formation of a surface depletion layer [Pip06]. Additional measurements of the surface depletion layer formation at the end of the nanowire (Position 3, Fig. 3.11a) are shown in Appendix C.

Estimation of the formation time of a surface depletion layer

The measured separation of the resonance position in Fig. 3.20b can be employed to estimate the strength of the built-in surface field and thus the formation time of the depletion layer in a straightforward calculation. At a pump-probe delay time of $t_{\mathrm{pp}} = 250\,\mathrm{fs}$, the carrier densities for low and high tapping amplitude are calculated using Equation 3.48 to be $3.45 \cdot 10^{18}\,\mathrm{cm}^{-3}$ (31.3 THz) and $3.76 \cdot 10^{18}\,\mathrm{cm}^{-3}$ (32.7 THz), respectively. The field generated by the difference in carrier density $\Delta N_{\mathrm{c}} = 3.15 \cdot 10^{17}\,\mathrm{cm}^{-3}$ is assumed to compensate the built-in surface field E_{d}. Thus, E_{d} can be approximated by a simple capacitor, whose field is given by

$$E_{\mathrm{d}} = \frac{\sigma}{\epsilon_0 \epsilon_\infty}\,, \tag{3.58}$$

with the surface charge density of a capacitor $\sigma = \Delta N_{\mathrm{c}} e d$ which depends on the charge separation distance d. The probing depth of the near-field signals can be estimated by the free-space decay length shown in Fig. 3.18b divided by the refractive index of InAs $\sqrt{\epsilon_\infty} = 3.51$. The calculated difference in probing depth of 3.2 nm between the high and low tapping amplitude serves here as an estimate for the charge separation distance d. Hence, the built-in surface field is calculated to be $E_{\mathrm{d}} \approx 15\,\mathrm{kV/cm}$, which is the same as

the order of magnitude for built-in surface fields reported in literature [Zha92, Dek93].

The formation time of the depletion layer can be estimated in the ballistic limit by considering the acceleration of a charged particle with an effective mass m^* in the surface field E_d. The transition time across the distance d is then calculated to be

$$t = \sqrt{\frac{2d}{a}} = \sqrt{\frac{2dm^*}{eE_\mathrm{d}}} \ . \tag{3.59}$$

By inserting the estimated electric field from Equation 3.58, the transition time can be rewritten

$$t = \sqrt{\frac{2m^*\epsilon_0\epsilon_\infty}{\Delta N_\mathrm{c} e^2}} \approx 25\,\mathrm{fs} \ , \tag{3.60}$$

whereby the dependence of the transition time on the charge separation distance d cancels. In this straightforward model, the formation time for a surface depletion layer in InAs solely depends on the difference in the carrier density, which can directly be extracted from the experimental measurements. The calculated formation time of 25 fs agrees remarkably well with the experimentally observed < 40 fs dynamics on the InAs nanowire measured by EOS (see Fig. 3.17).

3.6 Observation of femtosecond carrier dynamics on nanometer scales

In conclusion, the novel microscope is successfully employed to study the pump-induced carrier dynamics at the surface of bulk indium arsenide and single indium arsenide nanowires with spatial resolution of 10 nm ($\lambda/1000$). Using intensity-resolved detection and nano-FTIR of the scattered near field with a temporal resolution ≥ 60 fs, the dominant carrier decay channels in the investigated bulk InAs samples have been identified most likely to be surface state trapping (2 ps) and surface state recombination (30 ps). Furthermore, ultrafast imaging of the nanowire as a function of pump-probe delay time, locally-resolved pump-probe measurements, field-resolved detection and two-time multi-THz spectroscopy with 10 fs temporal resolution have been demonstrated within a single InAs nanowire, on a sub-nanoparticle scale. In addition, with the development of femtosecond tomography, the ultrafast build-up (< 40 fs) of a depletion layer at the surface of our highly doped InAs nanowires has been observed. Theoretical simulations of the near-field measurements with the help of an extended point-dipole model strongly corroborates the interpretation of the experimental data. A summary of the novel microscope, its capabilities and the experiments performed on InAs is published in *Nature Photonics* [Eis14].

Chapter 4

Ultrafast dynamics in strongly correlated materials

The motion of electrons in solids is determined by the long-range Coulomb interaction, where the correlation between all charged particles has to be considered. Therefore, it is surprising that the basic properties of condensed matter systems can often be understood in the limit of non-interacting electrons, where a single electron is assumed to move in an effective mean-field generated by all the charges in the system. However, the approximation of non-interacting electrons is insufficient to describe the unusual behavior emerging in many materials, e.g. transition-metal oxides. Fascinating effects like superconductivity [Onn11, Pas10], charge density waves [Grü88, Por14a] and insulator-to-metal transitions [Mor59, Küb07, Coc12] are just a few examples. The properties in such materials are dictated by electron-electron, electron-phonon and magnetic correlations [Bas11, Mor12], culminating in incredibly complex situations. Interestingly, these correlations can result in competing ground states, where slight changes in temperature, pressure or doping can induce a phase transition and significantly alter the macroscopic properties.

Vanadium dioxide (VO_2) has emerged as a model system for strongly correlated materials [Mor59], in particular, because it features a first-order insulator-to-metal phase transition [Ber69] at a temperature of $T_c = 341\,\mathrm{K}$. The change to the electronic behavior is accompanied by a rearrangement of the crystal lattice from a monoclinic phase at $T < T_c$, where the vanadium atoms are dimerized and tilted with respect to the c_R-axis, to a rutile phase at $T > T_c$, as seen in Fig. 4.1a and b, respectively (vanadium atoms: red, oxygen atoms: blue). The dissociation of the vanadium dimers leads to a halving of the crystal's unit cell (black dashed box) along the rutile crystal axis c_R. In this configuration, the vanadium atoms are arranged in a body-centered tetragonal lattice, where each vana-

dium atom is surrounded by an octahedron of oxygen atoms. The electronic properties can be described in a phenomenological band scheme [Goo71, Eye02] based on the hybridization of the oxygen $2p$ and vanadium $3d$-orbitals, leading to π and σ-like bands (see Fig. 4.1a and b). The larger overlap between the $2p$ and $3d$-orbitals forming the σ-band (not shown) increases their bonding-antibonding splitting to well below and above the Fermi energy and are therefore not considered here. In addition to the π-bands which are shown in Fig. 4.1b, the overlap of the vanadium $3d$-orbitals along the c_{R} direction of the rutile lattice establishes a conduction channel commonly labeled as the $d_{||}$-band. In the rutile (metallic) phase, the Fermi energy (gray dashed line) is located within the antibonding π^* and the $d_{||}$-bands. The transition into the monoclinic phase at lower temperatures (Fig. 4.1a) introduces a splitting of the $d_{||}$-band of approximately 2.5 eV [Koe06]. Furthermore, the displacement of the dimerized vanadium atoms increases the overlap of the $2p$ and $3d$-orbitals which enhances their coupling strength and shifts the π^*-band to higher energies [Shi90]. The splitting of the $d_{||}$-band and the energy shift of the π^*-band lead to the formation of a band gap with a transition energy from the $d_{||}$ to the π^*-band of 0.7 eV [Goo71], rendering monoclinic VO_2 an insulator. Despite the simple phenomenological picture of the band structure shown in Fig. 4.1, a theoretical calculation of the electron dispersion remains challenging [Wen94, Eye02]. First realistic results have been reported based on a cluster dynamical mean-field theory [Bie05], incorporating both electron-electron and electron-phonon correlations.

Although the optical properties of VO_2 are intensively studied, the physical origin of the observed phase transition remains controversial. Due to the concurrent change of the crystal structure and the electronic properties, two possible scenarios are debated: (i) The insulator-to-metal transition could be predominantly induced by electron-phonon correlations described by a Peierls instability [Goo71, Wen94]; (ii) strong electron-electron interactions could lead to a localization of the electrons by Coulomb repulsion, an effect attributed to a Mott transition [Zyl75]. A recent theoretical study, however, has underlined the importance of both electron-electron and electron-phonon correlations on the phase transition [Bie05, Küb07].

Ultrafast optical excitation of the electrons in the $d_{||}$-orbitals provides an alternative route to switch VO_2 from the insulating to the metallic state [Bec94, Cav01]. The pump-induced dynamics promise valuable insights into the temporal hierarchy of electronic and lattice contributions. If electron-electron correlations are responsible for the formation of the insulating phase, ultrafast carrier injection should lead to an instantaneous collapse of the band gap following photoexcitation. On the contrary, if the phase transition is invoked by a deformation of the crystal lattice, the metallic state is expected to appear temporally retarded. The observation of a subpicosecond formation time of the metallic

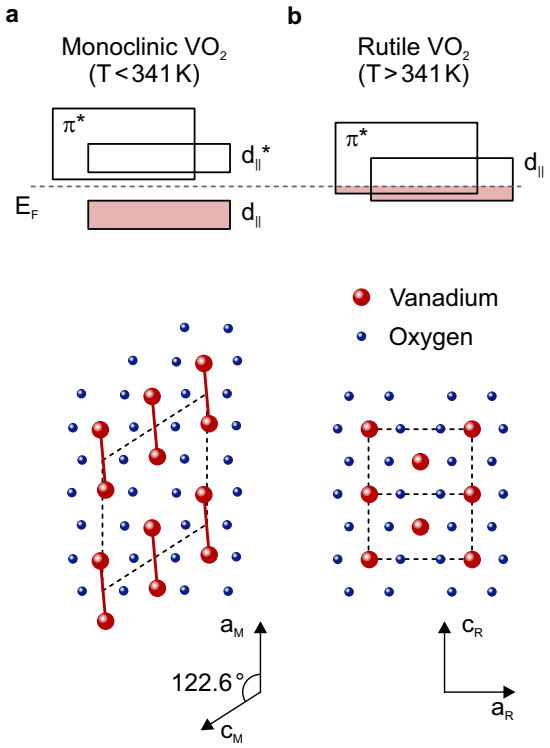

Figure 4.1 | Vanadium dioxide. a, Simple band structure and crystal lattice of monoclinic VO_2 at a temperature $T < 341\,\mathrm{K}$. The Fermi level (gray dashed line) is located between the bonding $d_{||}$ and the antibonding $d^*_{||}$-orbital, leading to the formation of a band gap with an energy from the $d_{||}$ to the π^*-band of 0.7 eV. The distorted crystal lattice features a dimerization of the vanadium atoms (red lines) and an angle between the a_M and the c_M-axis of 122.6 °. **b**, Rutile band and crystal structure of VO_2 which forms above the phase transition temperature of $T_\mathrm{c} = 341\,\mathrm{K}$. The band gap collapses, leading to a Fermi energy that is located in the $d_{||}$ and the π^*-bands. Simultaneously, the breaking of the vanadium dimers leads to a reordering of the crystal, resulting in a halving of the unit cell.

phase points towards a non-thermal behavior [Cav01, Küb07, Hil07, Nak08, Pas11, Coc12]. However, the extracted transition time is believed to be ultimately limited to 80 fs [Cav04], corresponding to half the oscillation period of the $5 - 6\,\mathrm{THz}$ phonons, which map the monoclinic onto the rutile lattice structure. This bottleneck in transition time has been attributed to the essential role of the crystal structure on the insulator-to-metal transition [Küb07, Pas11, Vee13].

Recent time-resolved photoelectron spectroscopy measurements of VO_2, however, are in contrast to the conclusions derived from the observed bottleneck in the switching dynamics. Tracing the energy of photo-emitted electrons as a function of pump-probe delay time has revealed a population of electron states at the Fermi energy immediately following photoexcitation [Weg14]. The instantaneous collapse of the band gap supports the idea of an electronically driven insulator-to-metal phase transition. In addition, recent optical pump-probe experiments performed on various single-crystalline VO_2 nanoparticles featured phase transition times ranging from 40 to 200 fs [Cal15]. The varying timescales are attributed to defects, dopants and strain, influencing the local behavior of the phase transition. These findings bring the conclusions obtained from far-field measurements on nano-granular VO_2 into questions and indicate the necessity to investigate the femtosecond dynamics of the phase transition on the nanometer scale where local effects can directly be identified and considered in the experimental analysis.

Scattering-type near-field scanning optical microscopy provides the means to investigate the surface of VO_2 with a spatial resolution on the 10-nm scale. Such measurements have demonstrated that the metallic state forms in nanometer-sized domains and subsequently grows while the sample is heated across the phase transition [Qaz07, Fre09, Qaz11]. Additionally, strain and defects have been shown to strongly influence the local phase transition within VO_2 single crystals [Jon10, Cal15] and films [Liu13, Liu14]. However, no time-resolved experiments have been reported investigating the femtosecond transition dynamics inside a single nanodomain. Such measurements could directly resolve the intrinsic material response without averaging over regions with different defect, dopant and strain densities and might identify the fundamental driving forces of the insulator-to-metal phase transition in VO_2. In this chapter, preliminary results of steady-state (**Section 4.1**) and ultrafast near-field microscopy (**Section 4.2**) performed on a single VO_2 nanowire are presented. These measurements mark the first detailed analysis of pump-induced carrier dynamics in VO_2 on the nanoscale and provide insight into the influence of the substrate on the local insulator-to-metal phase transition.

4.1 Thermally-driven phase transition

The VO_2 nanowires[1] investigated here are grown on a sapphire substrate and can be seen in the optical microscope image shown in Fig. 4.2a. During growth, the nanowires predominantly follow the hexagonal lattice structure of the substrate, leading to an ordered formation of nanowires on the surface. Interestingly, after a certain length several nanowires feature a distinct change in their growth direction, forming V-shaped structures with a characteristic angle of approximately 120 °, close to the angle of 122.6 ° between the a_M and c_M-axis of the monoclinic crystal (see Fig. 4.1a). An AFM scan of a single nanowire is shown in Fig. 4.2b. The nanowire has a length of approximately 7 µm and a width of 500 nm with defects located between $x = 1.5$ and 3.5 µm. In contrast, no defects are observed between $x = 3.5$ and 7 µm and the nanowire is assumed to be single crystalline within this region. This can also be seen in the near-field intensity I_3 at a sample temperature of $T = 294$ K (see Fig. 4.2c). In this case a continuous-wave quantum cascade laser (QCL) operating at a wavelength of 8.43 µm is used to illuminate the AFM tip. While the scattered near-field intensity is homogeneous along the single-crystal region of the nanowire, there is a modulation of I_3 at the defect sites.

An increase of the sample temperature to approximately 353 K (Fig. 4.2d) thermally drives the insulator-to-metal transition. A periodic modulation of I_3 is observed along

[1] The VO_2 nanowires have been provided by the group of Richard Haglund, Physics and Astronomy Department of the Vanderbilt University, TN 37240 Nashville, USA.

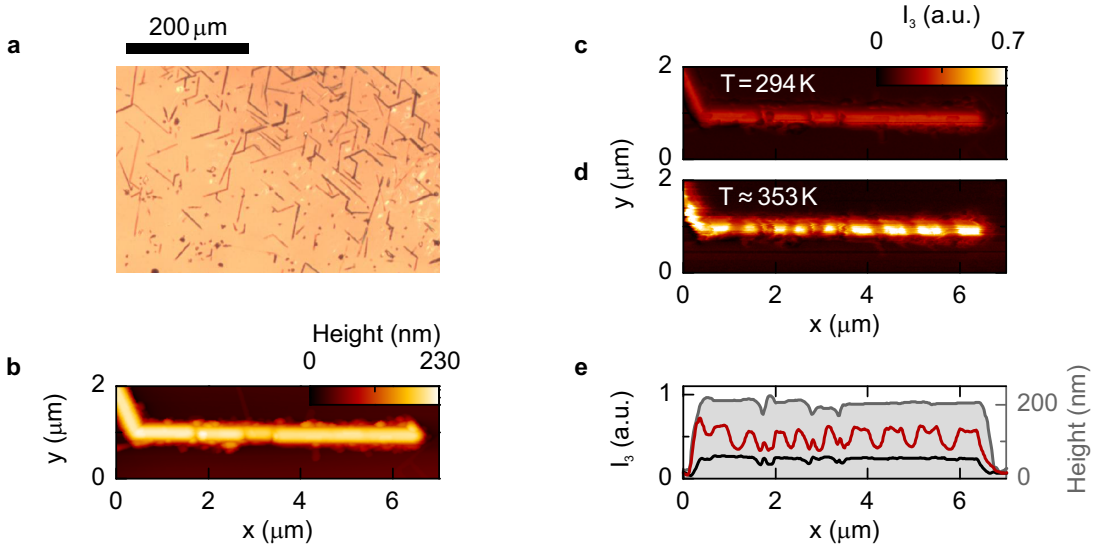

Figure 4.2 | Vanadium dioxide nanowires. **a**, Optical microscope image of the VO_2 nanowires on a sapphire substrate. The nanowires predominantly orient themselves during growth along the hexagonal crystal structure of the substrate. **b**, AFM image of a single nanowire with a length of approximately 7 µm and a width of approximately 500 nm. The smooth surface between $x = 3.5$ and 7 µm indicates that this region is single-crystalline VO_2, in contrast to the region between $x = 1.5$ and 3.5 µm, which has defects. **c**, Scattered intensity I_3 as a function of position on the nanowire corresponding to the AFM scan shown in **b**. Here, a continuous-wave quantum cascade laser (QCL) operating at a wavelength of 8.43 µm is used to illuminate the AFM tip. The sample temperature is set to $T = 294$ K. **d**, Near-field image of the nanowire heated across the phase transition to a temperature of $T \approx 353$ K. An alternating pattern of insulating and metallic domains is observed. **e**, Averaged line-scan of the near-field intensity along the nanowire axis at a temperature of $T = 294$ K (black curve) and $T \approx 353$ K (red curve). The line scans are extracted from the corresponding near-field images shown in **c** and **d** at $y \approx 1$ µm, averaged over an interval of $\Delta y \approx 200$ nm. The modulation period in the single-crystalline segment is approximately 770 nm. The gray shaded area corresponds to the height profile of the nanowire which is extracted from the atomic force microscope image in **b** at $y \approx 1$ µm. The atomic force microscope and the near-field measurements are performed with a tapping amplitude of 130 nm.

the nanowire axis, which can be explained as an alternating pattern of metallic and insulating domains. As expected from the point dipole model (see Section 3.2), the scattering efficiency off the metallic state is significantly increased when compared to the insulating state [Qaz07]. This is also seen prominently in the line-scans along the nanowire axis extracted from the near-field images at $T = 294\,\mathrm{K}$ (black curve) and $T \approx 353\,\mathrm{K}$ (red curve), shown in Fig. 4.2e. Note that the scattered intensity recorded on the insulating nanowire (black curve) does not feature any spatial inhomogeneity on the single crystal, which could be correlated to the appearance of the metallic domains. Such a periodic formation of metallic domains has already been observed along the c_R-direction of VO_2 placed on various substrates (SiO_2, TiO_2 or polycarbonate substrate) and has been interpreted to be the result of strain from the lattice mismatch between the sample and the substrate [Wu06, Cao09, Jon10, Liu13]. It has been postulated that to minimize the strain energy, a structural transition from the monoclinic into the rutile crystal structure occurs in certain domains, which is accompanied by a reduction of the c_R-axis by 1 % [Liu13]. While in the defect-rich section, the metallic domains occur correlated to the positions of the defects, the single-crystal region features a periodic pattern of domains with a modulation period of approximately 770 nm, indicating a uniform coupling of the nanowire to the substrate across the entire single crystal.

Optical photoexcitation of the $d_{||}$-electrons can alternatively be used to drive the insulator-to-metal phase transition and has already been employed in quasi-equilibrium near-field microscopy to investigate strained VO_2 films [Liu13]. Due to the high repetition rate of the laser system employed in this work, the photoinduced phase transition is not able to recover to the insulating state between subsequent pump pulses. Hence, by reaching a distinct threshold of photoexcitation, the phase transition is triggered and the metallic state persists until the pump pulses are switched off. However, it is yet unclear whether the optically and the thermally driven phase transitions on the VO_2 nanowire will result in the same near-field pattern. This is investigated by focusing the visible pump pulses ($\lambda \approx 800\,\mathrm{nm}$) on the sample below the tip while probing the near field with the continuous-wave radiation from the QCL scattered off the tip[2]. Due to the limited range of the pump fluence achievable from the frequency-doubled erbium-doped fiber laser system, the sample is heated to a temperature of $T \approx 338\,\mathrm{K}$ to reduce the threshold for photo-switching [Coc12]. Near-field images as a function of pump fluence Φ are shown in Fig. 4.3a. At $\Phi = 0.3\,\mathrm{mJ/cm^2}$, the scattered intensity is homogeneous with no indications of a phase transition. This situation changes at $\Phi = 0.5\,\mathrm{mJ/cm^2}$, where two metallic domains form, one near the right end and one near a defect. By further increasing the pump fluence,

[2] Note, that by using continuous-wave lasers as probe light, no time-resolved measurements can be performed and only the steady-state response is resolved.

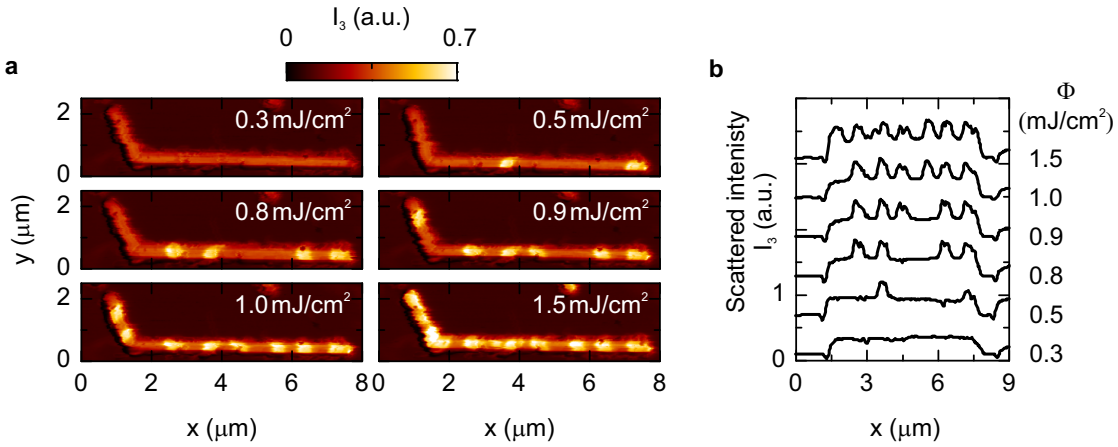

Figure 4.3 | Phase transition by optical excitation. **a**, Near-field images of the VO_2 nanowire, photoexcited by the visible pump pulses ($\lambda_{\text{pump}} \approx 780\,\text{nm}$) with a fluence varying between 0.3 and $1.5\,\text{mJ/cm}^2$ (pump power between 7.4 and 31.6 mW). The sample response is probed with the continuous-wave QCL. With increasing fluence, single domains switch into the metallic state, resulting in the same pattern as observed in the thermally driven phase transition, seen in Fig. 4.2d. **b**, Line scans measured along the nanowire axis as a function of pump fluence. All measurements are performed with a tapping amplitude of 130 nm and a sample temperature of 338 K.

more domains start to appear, leading ultimately to the same pattern as observed in the thermally driven phase transition in Fig. 4.2d. The position of the domains on the nanowire are constant once formed, as can be seen in the extracted line scans along the nanowire axis, shown in Fig. 4.3b.

4.2 Femtosecond carrier dynamics within a single vanadium dioxide nanowire

To investigate the character of the insulating state below the photo-switching threshold, ultrafast pump-probe measurements are performed in the center of different metallic and insulating regions. The nanowire is excited with a pump fluence of $1.7\,\text{mJ/cm}^2$ and the conductivity of the pump-induced carriers is subsequently probed by ultrabroadband multi-THz pulses. To avoid the transition of the nanowire into the metallic state in time-resolved measurements, the threshold for photo-switching is increased by reducing the sample temperature to $T = 294\,\text{K}$. Very first results of the electron dynamics in the VO_2 nanowire can be seen in Fig. 4.4, where Position 1 and 3 correspond to domains that develop a metallic character at elevated temperature (white circled areas) and Position 2

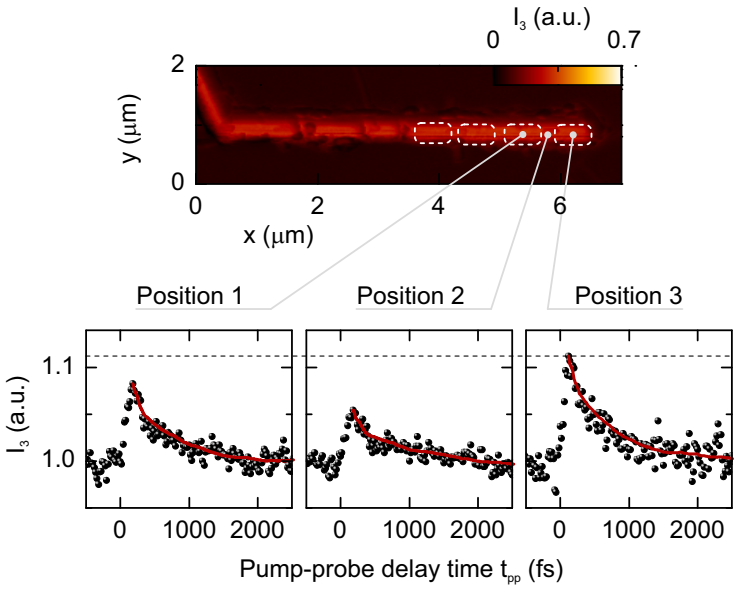

Figure 4.4 | Femtosecond dynamics within a single vanadium dioxide nanowire. Steady-state near-field image of the VO_2 nanowire (top) at a temperature of T = 294 K. The white circled areas highlight positions that switch to the metallic state at elevated temperatures. Position 1 and 3 indicate the first two metallic domains on the right while Position 2 corresponds to the insulating region in-between. Pump-probe traces (bottom) recorded at the positions indicated in near-field image (top). The pump-induced change ($\lambda_{\mathrm{pump}} \approx 780\,\mathrm{nm}$) of the scattered near field I_3 (black dots) is probed by an ultrabroadband multi-THz waveform as a function of pump-probe delay time t_{pp}. The red curves correspond to a smoothed average of the decay of the pump-probe trace. In all pump-probe measurements the tapping amplitude is 130 nm and the pump fluence is $1.7\,\mathrm{mJ/cm^2}$.

to an insulting domain (see Fig. 4.4, top). Upon photoexcitation, Position 1 features an increase of the scattered intensity I_3 with a rise time of approximately 250 fs, resulting in a maximum pump-induced change of I_3 compared to the unpumped value of 8 %, as can be seen in Fig. 4.4. The same dynamics are also observable at Position 3, featuring in comparison an increased peak height of 11 %, which is indicated by the gray dashed line. At Position 2, however, the maximum pump-induced change of I_3 is significantly reduced to approximately 5 %. In contrast to the homogeneously scattered intensity observed in quasi-equilibrium measurements on the insulating single-crystal nanowire (Fig. 4.2c and Fig. 4.3a at $0.3\,\mathrm{mJ/cm^2}$), the significant difference in peak height of the ultrafast pump-probe traces as a function of position can now be used to predict which parts of the nanowire switch to the metallic state at elevated temperatures. Even more, by comparing the pump-probe traces to the results obtained on indium arsenide, the change of the scattered intensity as a function of pump-probe delay time can qualitatively be correlated

with an increase of the conductivity in the sample. The subsequent decay of the carrier population then leads to a relaxation of the pump-induced response on a timescale of a few picoseconds. A more quantitative extraction of the carrier density and the decay time from the pump-probe traces is currently explored based on the point-dipole model, derived in Section 3.2.

The difference in the peak height observed in the pump-probe scans is rather surprising, as the pump fluence and hence the density of photoinjected carriers should be close to identical at all three positions. In addition, the single-crystalline VO_2 renders a dependence of the scattered intensity on surface artifacts unlikely. Most probably, the difference in the observed peak height is therefore correlated to the local conductivity of the sample, which is modified within certain regions of the nanowire due to strain induced by the substrate. This complements the observation of the fluence dependence of the optically driven phase transition at elevated temperatures shown in Fig. 4.3a. Since Position 3 exhibits the highest conductivity, the phase-transition threshold is already achieved at a moderate pump fluence of $0.5\,\mathrm{mJ/cm^2}$ (11.7 mW). The reduced conductivity at Position 1 seems to be correlated with an increased threshold for photo-switching and a higher pump fluence ($0.8\,\mathrm{mJ/cm^2}$, 16.6 mW) is needed to drive the phase transition. Finally, due to the lowered conductivity at Position 2, no phase transition is observed within the range of the pump fluence available in the experiment.

These preliminary results of the dynamics of the photoinduced carrier density in VO_2 in combination with the spatially-resolved fluence dependence in the optically-induced phase transition underline the novel insights obtained by combining high spatial *and* temporal resolution. Going beyond quasi-equilibrium measurements, the ultrafast response as a function of position can now be used to predict the switching behavior of the insulator-to-metal transition. Finally, the extraction of the conductivity from the pump-probe traces could be a measure of the localization of the electrons and how they are influenced by strain and defects on the nanoscale. A more detailed experimental and theoretical analysis of the VO_2 nanowire and its ultrafast response upon photoexcitation of free carriers is subject to current research and will soon help to quantitatively discuss the observed dynamics.

Chapter 5

Summary and outlook

This thesis has introduced a novel microscope which combines the outstanding properties of ultrafast multi-THz spectroscopy and scattering-type scanning near-field optical microscopy to observe the femtosecond dynamics of low-energy elementary excitations, e.g. phonons, plasmons and excitons, at the surface of solid-state systems. Ultrabroadband phase-locked mid-infrared light pulses are focused onto a nanometer-sized metal tip of the atomic force microscope. When approached to a sample surface, the tip acts as a local optical probe, confining the light pulses at its apex. Detection of the scattered radiation reveals information about the optical properties of the sample with a spatial resolution of 10 nm, ultimately limited by the tip radius of curvature. Electro-optic sampling, one of the most notable techniques of THz spectroscopy, is employed to detect the scattered oscillating electric near field directly in the time domain with a temporal resolution of 10 fs. Together with pump-probe experiments this technique enables the observation of the dynamics of low-energy elementary excitations on sub-cycle timescales, faster than a single oscillation cycle of the multi-THz probe pulses. The combination of ultrafast multi-THz spectroscopy and near-field microscopy culminates in a unique microscope that achieves an unprecedented combined temporal (10 fs) and spatial (10 nm) resolution in the mid-infrared wavelength region [Eis14].

The novel microscope is based on the combination of two technology platforms: (i) An ultrastable and ultracompact erbium-doped fiber laser system that is entirely custom tailored for preeminent performance; (ii) a near-field microscope based on non-dispersive optics, which guarantees the utmost temporal resolution by avoiding temporal broadening of the femtosecond light pulses. The laser system provides few-cycle multi-THz pulses with center frequencies in the range of 27 to 52 THz with pulse energies of up to 28 pJ. These waveforms are sent into the near-field microscope, where they are focused onto the

atomic force microscope tip to probe the local sample response. The scattered radiation, originating from a volume of approximately $(10\,\mathrm{nm})^3$, is detected by either a photodiode or by electro-optic sampling, which traces the oscillating electric field stroboscopically with 10-fs gate pulses. In addition, to investigate non-equilibrium dynamics, ultrashort pump pulses in the near infrared (pulse duration 22 fs) or in the visible (pulse duration $48-65\,\mathrm{fs}$) are used to photoexcite the sample below the tip. The combination of multi-THz nano-spectroscopy with pump-probe measurements enables two-time THz spectroscopy on the nanoscale, which makes it possible to trace the evolution of the sample following ultrafast excitation on a sub-cycle timescale (10 fs) while simultaneously maintaining a spatial resolution of 10 nm. The fundamental advantage of field-resolved detection of the scattered terahertz waveforms originates from the direct access to both the absolute phase and amplitude in the frequency domain via Fourier transformation. Hence, the temporal evolution of the local, complex-valued dielectric function of the sample can be retrieved. Alternatively, spectrally-resolved measurements can also be performed by nano Fourier transform infrared spectroscopy. However, this measurement scheme is based on intensity-resolved detection and is thus limited to a temporal resolution given by the duration of the multi-THz probe pulses at best ($> 60\,\mathrm{fs}$).

In a proof of principle experiment, the pump-induced carrier dynamics in bulk indium arsenide have been investigated. Here, the photoinjection of electrons by the 22-fs near-infrared pump pulse shifts the screened plasma frequency of the free carriers in indium arsenide into the spectral range of the probe pulses, leading to the formation of a pronounced resonance. Tracing the plasma resonance as a function of pump-probe delay time directly reveals the carrier recombination dynamics, which have been identified as trapping of electrons into surface states on a sub-2-ps timescale and subsequent surface state recombination with a decay time of 32 ps.

Following these introductory experiments, time-resolved near-field microscopy in the multi-THz frequency range is extended to nanoscale objects, yielding for the first time a detailed insight into the carrier dynamics of InAs nanowires on the sub-nanoparticle scale. By mapping the scattered intensity as a function of position and pump-probe delay time an ultrafast movie of the carrier distribution following photoexcitation is recorded. To resolve the carrier dynamics within the nanowire on a sub-cycle timescale, two-time THz spectroscopy is performed, tracing the oscillating electric near field scattered off the sample surface as a function of pump-probe delay time. Similar to bulk indium arsenide, a resonance is observed within the spectrum of the multi-THz probe pulses, which is linked to the plasma frequency of the carriers in the nanowire. However, the decay dynamics are distinctly different: Upon photoexcitation the initial carrier density decays within less

than 40 fs. This ultrafast decay is followed by trapping of electrons into surface states with a time constant of approximately 2 ps, similar to the decay time observed in the bulk material. To unravel the origin of this ultrafast decay (< 40 fs), a new technique has been developed in the course of this thesis which is called femtosecond tomography. The near-field confinement at the tip apex extends not only laterally but also vertically from the tip into the sample. Interestingly, adjusting the tapping amplitude can thereby be used to tune the probing volume, enabling the observation of depth-dependent dynamics. By performing femtosecond tomography, the initial decay has been found to depend on the probing depth and has been attributed to the formation of a depletion layer at the surface of the indium arsenide nanowire within less than 40 fs [Eis14].

A theoretical description of the detected signals scattered off the atomic force microscope tip has been achieved in the framework of the point-dipole model, which has been refined to be applicable to the experiments performed. The simulations solely depend on the dielectric function of the sample, which is modeled in the case of indium arsenide with the Drude formalism describing free carriers in semiconductors. Using only the carrier density and the Drude scattering rate as free fitting parameters, an excellent agreement has been achieved between simulation and experiment. The dependence of the near-field interaction on the dielectric function of the sample is now understood in detail and can be used to predict the image contrast and the influence of photoexcitation on the scattering response in a wide class of materials.

Furthermore, this thesis shows first ultrafast pump-probe measurements performed on the strongly correlated material vanadium dioxide using the ultrafast near-field microscope. A thorough understanding of the emerging many-body phenomena in such systems is often hindered by the tremendous complexity of the interplay of electron-electron, electron-phonon and magnetic correlations. In this context, vanadium dioxide is one of the most intensely studied model systems, featuring a first order insulator-to-metal transition which can be driven optically or thermally. Due to the concurrent change of the electronic properties and the lattice structure during the phase transition, the origin of the insulator-to-metal transition has been the center of controversy. This thesis introduces first time-resolved near-field experiments, which have been performed on a single vanadium dioxide nanowire attached to a sapphire substrate. By heating the sample across the phase transition temperature, a periodic pattern of insulating and metallic domains forms along the nanowire axis, which has been attributed to surface strain induced by a lattice mismatch between the vanadium dioxide nanowire and the substrate. To investigate the influence of the strain on the conductivity of the electrons, visible-pump multi-THz probe experiments have been performed at certain positions along the nanowire while the sam-

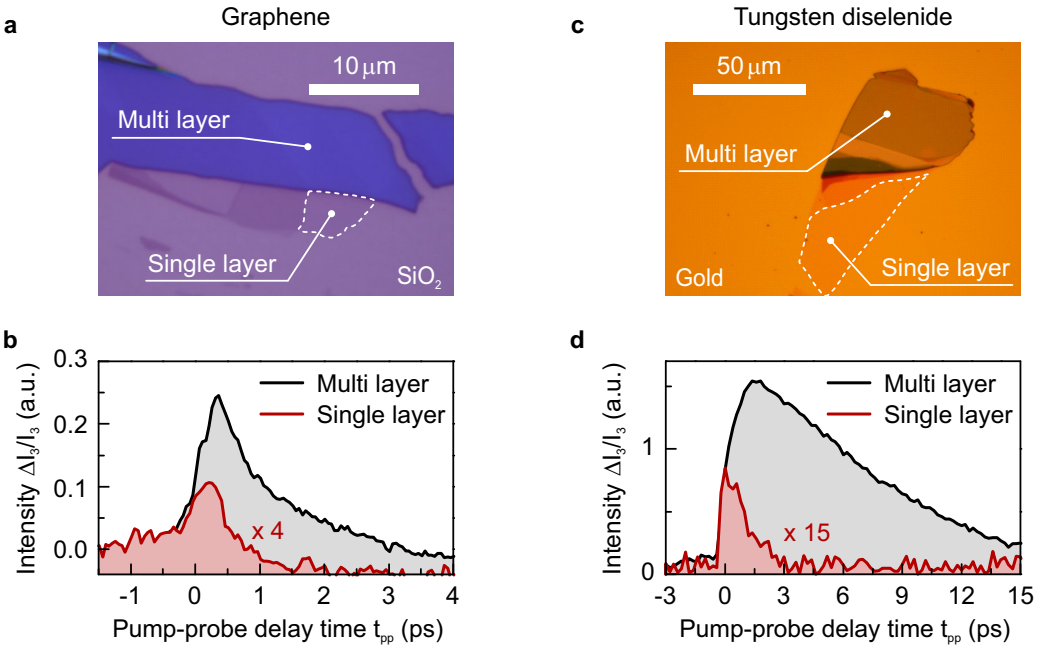

Figure 5.1 | Carrier dynamics in single layer materials. **a**, Optical microscopy image of an exfoliated graphene sample on a silicon dioxide (SiO_2) substrate. An area consisting of single layer graphene is indicated by the white dashed curve. **b**, Relative pump-induced change of the scattered intensity normalized to the unpumped value ($\Delta I_3/I_3$). Upon photoexcitation with the 60-fs visible pump pulses ($\lambda_{\text{pump}} \approx 777\,\text{nm}$), the scattering response of single layer (red curve, $\times 4$ magnification factor) and multi-layer graphene (black curve) is significantly enhanced. **c**, Optical microscopy image of an exfoliated tungsten diselenide sample on a gold substrate. The single layer region is indicated by the white dashed curve. **b**, Relative pump-induced change of the scattered intensity normalized to the unpumped value ($\Delta I_3/I_3$). Upon photoexcitation with the 60-fs visible pump pulses ($\lambda_{\text{pump}} \approx 777\,\text{nm}$), both the single layer (red curve, $\times 15$ magnification factor) and the multi-layer of tungsten diselenide (black curve) feature an increased scattering response. In all measurements the pump fluence is $0.6\,\text{mJ/cm}^2$ and the tapping amplitude is 130 nm.

ple temperature was below the phase transition temperature. Surprisingly, domains that switch to the metallic state at elevated temperatures exhibit a photoconductivity which is approximately a factor of two higher than domains which remain in the insulating phase. These preliminary results point towards a strong influence of the local strain on the electrons inside the strongly correlated material even in the insulating state and are currently being investigated in greater detail.

Future directions of the novel ultrafast near-field microscope include the investigation of single layer materials like transition metal dichalcogenides [Hua12, Che14, Doc14], boron nitride [Dai14, Dai15], graphene [Gei07] and single layer heterostructures [Nov12, Gei13, Xia14, Woe15]. These materials are regarded as novel building-blocks for upcoming elec-

tronic and optoelectronic devices and are the subject of intense research. The indirect observation of propagating surface plasmons on single layer graphene using steady-state near-field microscopy [Fei11, Che12, Fei12, Fei13, Ger14] has especially underlined the potential of graphene as an interface between optics and electronics [Bon10, Kop11, Gri12]. The key properties of these plasmons include high field confinement, exceptionally low damping and high tunability of their amplitude and wavelength using electrostatic gating. Field-resolved detection of the radiation scattered off a graphene sheet would enable the direct observation of the transient electric field of the propagating surface plasmons in space and time, providing insight into the plasmon dispersion, local defects and loss channels. In addition, by pump-induced heating of the electron gas, the high sensitivity of the surface plasmons on the conductivity of the carriers in the graphene sheet can be exploited to tune the plasmonic response on ultrafast timescales [Wag14a]. First pump-probe measurements performed on single-layer and multi-layer graphene[1] and tungsten diselenide[2] using our novel microscope are shown in Fig. 5.1a,b and Fig. 5.1c,d, respectively. These measurements are the starting point for novel ultrafast single-layer-based experiments investigating the dynamics of propagating surface plasmons on graphene or the spatio-temporal dependence of tightly-bound excitons in transition metal dichalcogenides [Che14] in unprecedented spatial and temporal detail.

The combination of ultrafast multi-terahertz spectroscopy with scattering-type near-field scanning optical microscopy, demonstrated here, paves the way towards a completely new class of nanoscale experiments with a three-dimensional spatial resolution far below the diffraction limit. Femtosecond dynamics of low-energy elementary excitations can in principle now be traced on a sub-cycle timescale in virtually any system suitable for time-resolved spectroscopy in the multi-terahertz range.

[1] The graphene samples have been provided by the group of Jonathan Eroms and Dieter Weiss, Department of Physics, University of Regensburg, 93040 Regensburg, Germany.

[2] The tungsten diselenide samples have been provided by the group of Tobias Korn and Christian Schüller, Department of Physics, University of Regensburg, 93040 Regensburg, Germany.

Appendix A

Data evaluation and drift correction

As already highlighted in Section 2.2.1, the multi-THz pulses generated by difference frequency mixing between the pulses from Amplifiers I and II are intrinsically carrier envelope phase (CEP) stable. However, fluctuations in the timing between the pulse trains can lead to a drift of the absolute carrier envelope phase Φ_{CE} in time as seen by

$$\Phi_{\mathrm{CE}} = 2\pi \cdot f_{\mathrm{THz}} \cdot t_{\mathrm{DFG}} \ . \tag{A.1}$$

Here, t_{DFG} is the relative delay between the pulses from Amplifiers I and II and f_{THz} the frequency of the generated multi-THz radiation. The expected change in the CEP can be estimated by a straightforward calculation. By using the thermal expansion coefficient of the optical table (steal, expansion coefficient $\alpha = 13 \cdot 10^{-6}\,1/\mathrm{K}$) and by approximating the independent beam path of the pulses from Amplifiers I and II by $L = 1\,\mathrm{m}$, the relative change in the optical path length between the two pulse trains is $\Delta L = \alpha \cdot \Delta T \cdot L = 1.3\,\mu\mathrm{m}$ at a temperature change of only $\Delta T = 0.1\,\mathrm{K}$. This corresponds to a change in the relative timing $t_{\mathrm{DFG}} \approx 4\,\mathrm{fs}$. By assuming a center frequency of $f_{\mathrm{THz}} = 30\,\mathrm{THz}$ the CEP changes by approximately $\pi/4$.

The drift of the CEP sets an upper limit to the measurement time of a complete multi-THz waveform and thus the lock-in integration time, making it impossible to directly measure the waveforms scattered off the AFM tip with a decent signal-to-noise ratio. In addition, the timing jitter between the multi-THz waveform and the gate pulses further complicates the problem. However, instead of measuring only a single waveform with a high lock-in integration time, which is subjected to thermal drift, many transients can be recorded with a low lock-in integration time on a timescale where thermal drifts can still be neglected. Subsequent correction of the thermally induced drifts followed by averaging of the corrected waveforms can then be employed to increase the signal-to-noise ratio.

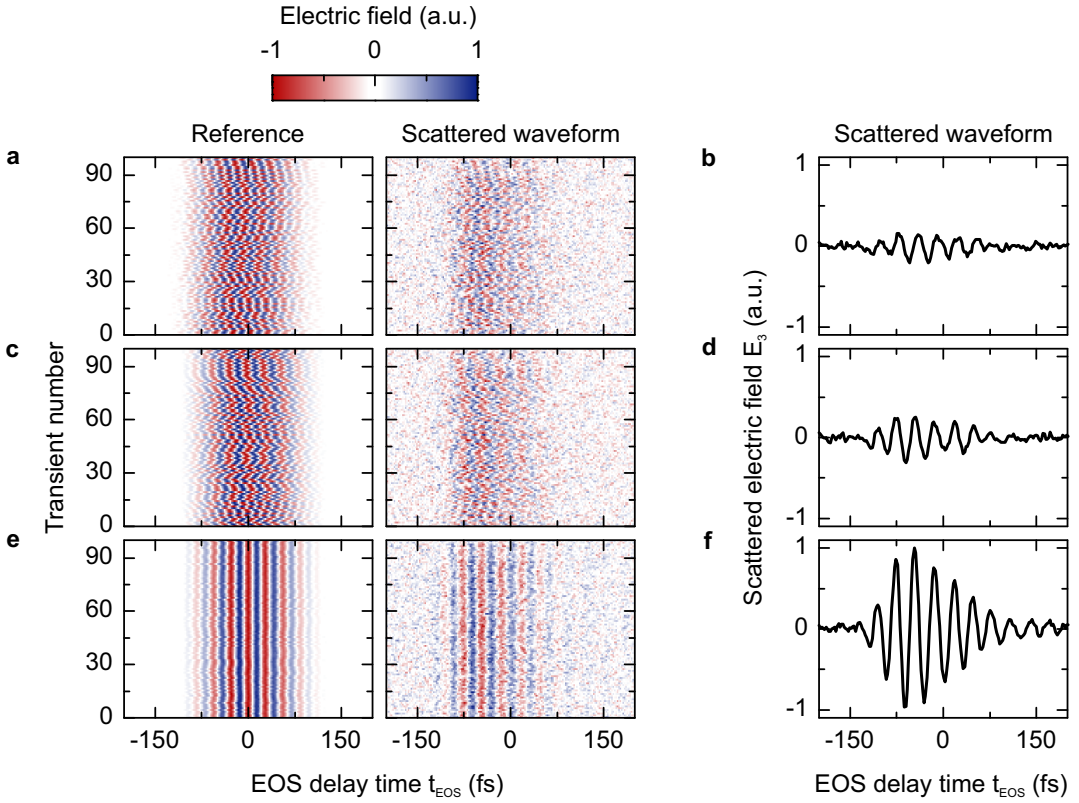

Figure A.1 | Drift corrections. **a**, Two-dimensional map of 100 multi-THz waveforms reflected off the reference arm of the Michaelson-type interferometer in the near-field microscope and detected at a lock-in frequency of 20 MHz (Reference). Simultaneously recorded waveforms scattered off the atomic force microscope tip of the near-field microscope, detected at a lock-in frequency of $20\,\mathrm{MHz} + 3 \cdot \Omega_{\mathrm{tip}}$ (scattered waveform). **b**, Averaged scattered waveform calculated from the two-dimensional map of the scattered waveforms in **a**. **c**, Reference and scattered waveforms after correction of the timing jitter between the multi-THz pulses and the gate pulses. **d**, Averaged scattered waveform calculated from the two-dimensional map in **c**. **e** Reference and scattered waveform after correction of the CEP drift. Now a oscillating pattern of the scattered signal can clearly be recognized. **f**, The averaged scattered waveform of the corrected signals shown in **e** features an increase of the peak electric field by more than a factor of 4 as compared to the uncorrected averaged waveform in **b**.

The intense multi-THz pulses reflected off the reference arm of the build-in Michaelson interferometer (see Section 2.4) serve here as reference and are recorded simultaneously to the scattered waveforms. Fig. A.1a displays a two-dimensional map of 100 multi-THz waveforms measured at a lock-in frequency of 20 MHz (Reference) and a lock-in frequency of $20\,\mathrm{MHz} + 3 \cdot \Omega_{\mathrm{tip}}$ (scattered waveform). Both maps feature a severe drift of the CEP in time. The averaged waveform calculated from the scattered waveforms can be seen in Fig. A.1b.

To correct for the timing jitter between the multi-THz pulses and the gate pulses, the field envelope of each multi-THz reference waveform is fitted by a Gaussian envelope and shifted in time to a defined zero-point. Importantly, this shift is also applied to the corresponding scattered waveform. The result can be seen in Fig. A.1c with the averaged scattered waveform in Fig. A.1d. Finally, the CEP of each reference waveform is determined and subtracted from both the reference and the corresponding scattered waveform (Fig. A.1e). The averaged, drift-corrected scattered waveform (Fig. A.1f) features an increase of the peak electric field of more than 4 as compared to the uncorrected averaged waveform.

Important remark: The technique of correcting the drift of the CEP of the scattered waveform with the help of a simultaneously recorded reference transient is only applicable in the case of linear optics, where the exact value of the CEP does not change the physical outcome of the experiment. As soon as nonlinear effects determine the near-field response of the sample a different approach has to be used to increase the signal-to-noise ratio. A possible alternative to correcting the CEP could be the sorting and binning of the scattered waveforms by their CEP value. The CEP value can here be determined with the help of the reference waveform. Subsequent averaging would also result in an increase of the signal-to-noise ratio. Ultimately, the drift of the CEP could be avoided by using optical rectification to generate the multi-THz waveforms. Unfortunately this approach could not be pursuit in this work, since the multi-THz power generated by optical rectification with the employed laser system did not suffice to perform near-field microscopy.

Appendix B

Nano Fourier transform infrared spectroscopy on the InAs nanowire

As an alternative to two-time THz spectroscopy (see Section 3.4), the carrier dynamics within the InAs nanowire can also be investigated by nano-FTIR. Since this technique is based on intensity-resolved detection of the scattered light pulses, the highest temporal resolution is, however, intrinsically limited to the duration of the multi-THz probe pulses at best ($\geq 60\,\mathrm{fs}$). The amplitude $\tilde{I}_3$ and relative phase $\Delta\Phi_3$ of the scattered multi-THz pulse measured by nano-FTIR in the center of the nanowire (Position 1 in Fig. 3.11a) as function pump-probe delay time t_{pp} are shown in Fig. B.2a and c, respectively. Upon photoexcitation the plasma resonance forms at the high frequency edge of the scattered spectrum, subsequently red-shifting through the frequency bandwidth (blue curve) with evolving pump-probe delay time. At the frequency of the resonance position, a distinct change in the relative phase of approximately 1.5 rad is observed. The scattered amplitude spectra and the relative phases are simulated using the point-dipole model (see Section 3.2) with a dielectric function given by the Drude model and are shown in Fig. B.2b and d, respectively. Using only the carrier density N_{c} and the Drude scattering rate γ as free fitting parameters, the experimental data is reproduced.

The resonance position ν_0 as a function of pump-probe delay time extracted from the scattered spectra are shown in Fig. B.2a. As already seen in the field-resolved measurements shown in Fig. 3.16, the carrier density decays, featuring two distinct time constants

$$\nu_0(t_{\mathrm{pp}}) = 11\,\mathrm{THz}\cdot \mathrm{e}^{-t_{\mathrm{pp}}/50\,\mathrm{fs}} + 28.6\,\mathrm{THz}\cdot \mathrm{e}^{-t_{\mathrm{pp}}/5\,\mathrm{ps}} + 7.5\,\mathrm{THz}\ . \tag{B.1}$$

The offset frequency of 7.5 THz corresponds to the plasma frequency of the extrinsic carrier

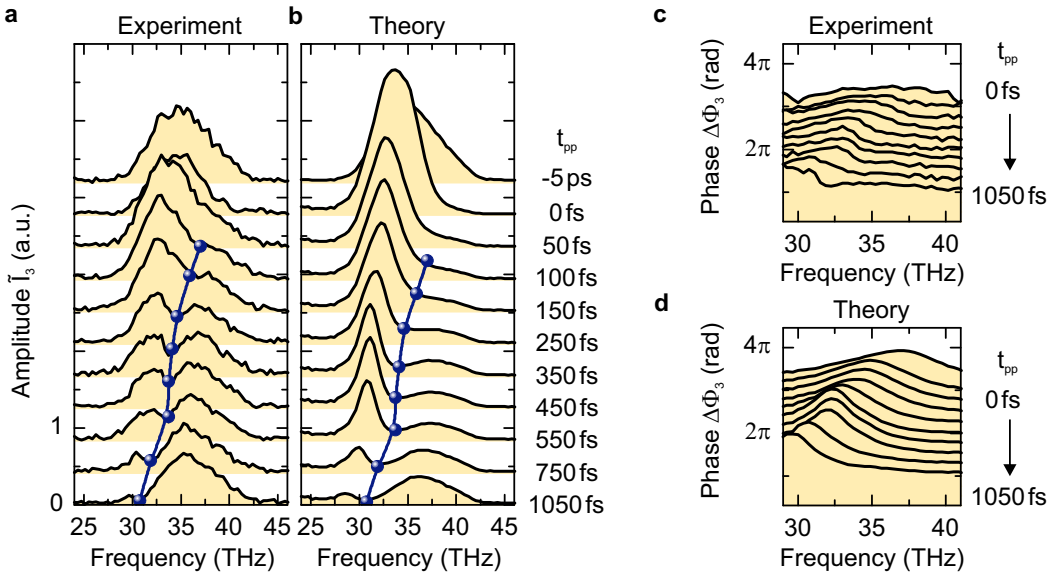

Figure B.1 | Nano Fourier transform infrared spectroscopy on a single indium arsenide nanowire. **a**, Amplitude spectra $\tilde{I}_3$ of the scattered multi-THz probe pulses measured by nano-FTIR, as a function of pump-probe delay time t_{pp}. The resonance position ν_0 is indicated by the blue dots. **b**, Simulated amplitude spectra using the point-dipole model and a nanowire dielectric function given by the Drude model. The simulations only depend on two parameters: The carrier density N_{c} and the Drude scattering rate γ. **c**, Relative phases $\Delta\Phi_3$ of the scattered pulses measured by nano-FTIR. A phase shift of approximately 1.5 rad is observed at the resonance position. **d**, Calculated phases extracted from the point-dipole model using the same parameters as in the corresponding amplitude spectra in **b**. For the experimental data, the pump fluence is 1.1 mJ/cm^2 and the tapping amplitude is 130 nm.

concentration of $2 \cdot 10^{17}\,1/\mathrm{cm}^3$. The fast initial decay has a time constant of 50 ± 40 fs (resolution limited) followed by a slower decay with a decay time of 5.0 ± 0.6 ps. The dynamics of the carrier density N_{c} calculated by the simulations are shown in Fig. B.2b, being consistent with a bi-exponential curve

$$N_{\mathrm{c}}(t_{\mathrm{pp}}) = 7.3 \cdot 10^{17}\,1/\mathrm{cm}^3 \cdot \mathrm{e}^{-t_{\mathrm{pp}}/25\,\mathrm{fs}} + 4.3 \cdot 10^{18}\,1/\mathrm{cm}^3 \cdot \mathrm{e}^{-t_{\mathrm{pp}}/2.9\,\mathrm{ps}} + 2 \cdot 10^{17}\,1/\mathrm{cm}^3\ . \quad \text{(B.2)}$$

The decay time $\tau_1 = 25$ fs is defined to be half the initial decay time of the resonance position as expected from the relation between the carrier density and the plasma frequency ($\nu_0 \approx \omega_{\mathrm{p}} \propto \sqrt{N_{\mathrm{c}}}$). The carrier densities weighting the exponentials and the second decay time are taken as free fitting parameters. The slower decay ($\tau_2 = 2.9 \pm 0.2$ ps) is comparable to the initial dynamics observed on bulk InAs and is therefore assigned to electron trapping into surface states.

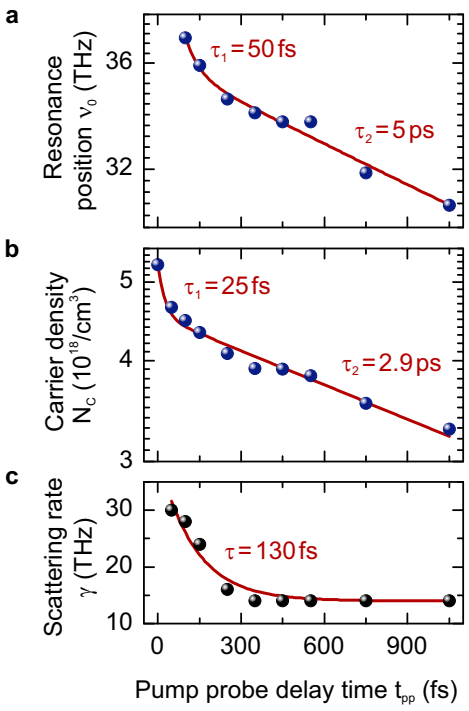

Figure B.2 | Carrier dynamics on a single indium arsenide nanowire measured by nano Fourier transform infrared spectroscopy. a, Resonance position ν_0 as a function of pump-probe delay time t_{pp}, extracted from the scattered amplitude spectra in Fig. B.1a. A bi-exponential decay of the resonance position on a semi-logarithmic scale is observed, featuring a fast decay time of $\tau_1 = 50\,\mathrm{fs}$, followed by a slower decay time of $\tau_2 = 5\,\mathrm{ps}$. **b**, Carrier density N_{c} as a function of t_{pp} extracted from the point-dipole model. Similar to **a**, a bi-exponential decay is retrieved. The fast decay time is defined to $\tau_1 = 25\,\mathrm{fs}$ followed by carrier trapping into surface states with a decay time of $\tau_2 = 2.9\,\mathrm{ps}$. **c**, Drude scattering rate γ extracted from the point-dipole model. The scattering rate of the hot electron gas decays within $\tau = 130\,\mathrm{fs}$ to $14\,\mathrm{THz}$.

The decay of the Drude scattering rate can be fitted by

$$\gamma(t_{\mathrm{pp}}) = 25\,\mathrm{THz} \cdot \mathrm{e}^{-t_{\mathrm{pp}}/130\,\mathrm{fs}} + 14\,\mathrm{THz}\ . \tag{B.3}$$

Following photoexcitation, a highly energetic electron gas is present, featuring a Drude scattering rate of $\gamma = 30\,\mathrm{THz}$ (at $t_{\mathrm{pp}} = 50\,\mathrm{fs}$). Within $\tau = 130 \pm 22\,\mathrm{fs}$, γ decays to $14\,\mathrm{THz}$, which agrees with reported scattering rates for electrons in InAs nanowires

Appendix C

Depletion layer formation at the nanowire end

Femtosecond tomography is employed to investigate the formation of the surface depletion layer at Position 3, which is indicated in Fig. 3.11a. In Fig. C.1a the scattered intensity I_3 as a function of pump-probe delay time t_{pp} is shown for tapping amplitudes of 55 nm (red curve) and 135 nm (black curve). The pump-probe dynamics are normalized to the unpumped baseline at negative delay times to account for changes to the scattered intensity with varying tapping amplitude. Upon photoexcitation I_3 is enhanced by a factor of approximately 1.8 at $t_{\mathrm{pp}} \approx 30$ fs. With evolving t_{pp}, the decay of both pump-probe traces is dominated by a sub-100-fs decay indicating the formation of a surface depletion layer even for larger tapping amplitudes. This can be seen even more prominently by extracting the dynamics of the resonance position ν_0, as can be seen in Fig. C.1b. At $t_{\mathrm{pp}} = 50$ fs the resonance positions coincide for low (red dots) and high (black dots) tapping amplitudes, which agrees with the tomographic observations at Position 1 (see Fig. 3.20b). In contrast to the measurements performed at Position 1, the resonance position shows a fast decay for both low (55 nm) and high (135 nm) tapping amplitudes. Hence, even for larger probing depths, the electrons are accelerated out of the near-field probing volume which may be attributed to a thicker depletion layer.

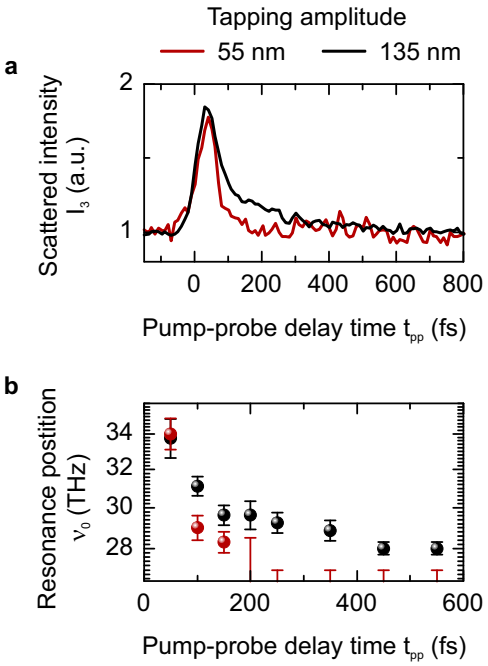

Figure C.1 | Femtosecond tomography at the nanowire end. **a**, Pump-probe dynamics of the scattered intensity I_3 for tapping amplitudes of 55 nm (red curve) and 135 nm (black curve). Scans are normalized to the unpumped baseline to account for changes to the scattering efficiency with tapping amplitude. **b**, Resonance position ν_0 plotted on a semi-logarithmic graph. ν_0 is extracted from the amplitude spectra measured by nano-FTIR as a function of time after photoexcitation for a tapping amplitude of 135 nm (black dots) and 55 nm (red dots). The carrier dynamics in both cases feature a fast initial decay indicating a significant reduction of the carrier density due to the formation of a surface depletion layer, even for larger probing depths. For all measurements the pump fluence is 0.75 mJ/cm^2.

Appendix D

Build-up of the near-field laboratory

The novel microscope introduced in this work was set up in a specially designed laboratory at the University of Regensburg. The main focus in designing a suitable environment for ultrafast near-field microscopy has been on long-term stability and low vibrational background. The near-field laboratory is therefore situated on the base plate of the physics department, which reduces acoustic vibrations to a minimum, while in addition providing a stable thermal environment. To minimize fluctuations in temperature and humidity, an air conditioning system is employed. The laser system as well as the near-field microscope are mounted on an optical table to isolate the experimental setup from the remaining vibrations from the laboratory floor.

With the installation of the optical table in May 2011, first tests of the laser system have been performed. Within the next months the multi-arm erbium-doped fiber-laser has been custom tailored to generate multi-THz radiation and first waveforms were detected by electro-optic sampling in December 2011 (see Fig. D.1a). With the microscope in place (January 2012), the optical setup has been completely rearranged to incorporate the microscope and to reduce the spatial footprint of the whole experimental setup. This way the influence of thermal drift and mechanical vibrations on the experiment have been minimized. First near-field waveforms scattered of the atomic force microscope tip were detected field-resolved by electro-optic sampling in March 2013. Fig. D.1b-d shows the current experimental setup which is used to perform ultrafast multi-terahertz nano-spectroscopy with a spatial resolution of 10 nm and a temporal resolution of 10 fs.

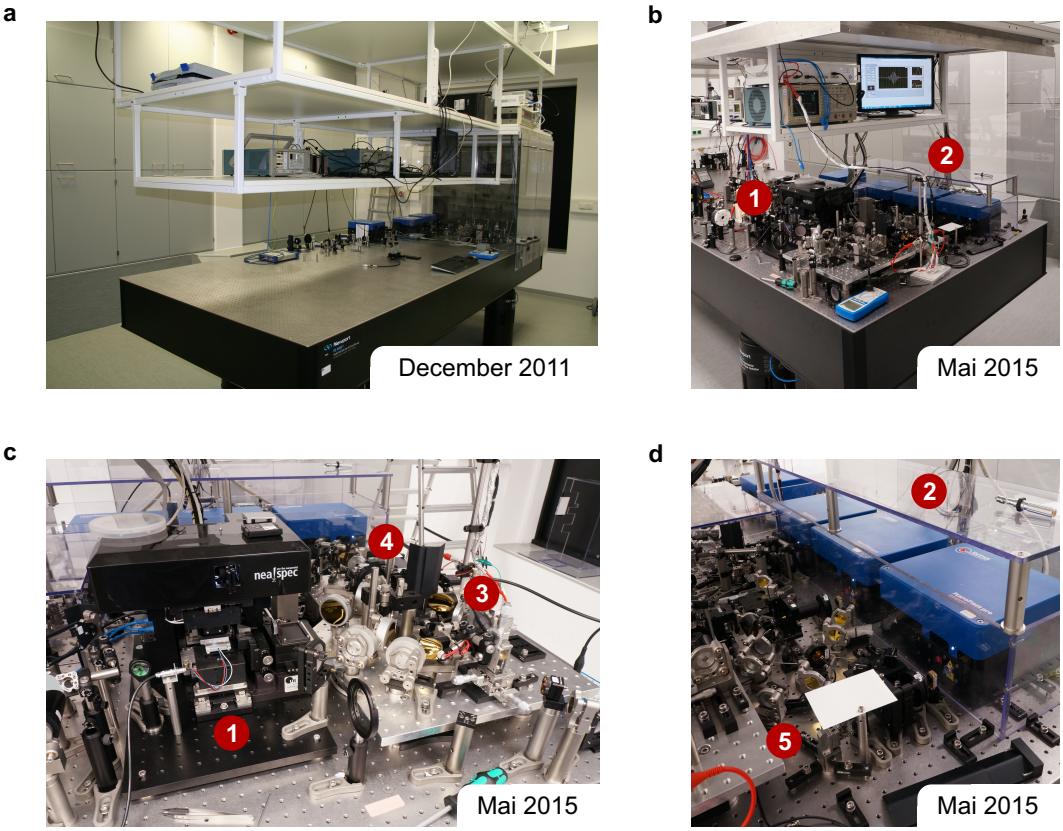

Figure D.1 | The near-field laboratory. **a**, First generation and detection of phase-stable multi-THz waveforms in the near-field laboratory at the University of Regensburg in December 2011. **b**, Current state (May 2015) of the experimental setup used to perform ultrafast multi-THz near-field microscopy. Note the extremely small footprint of the entire experimental system, incorporating the near-field microscope (1) and the four-arm erbium-doped fiber laser system (2, blue boxes). **c**, Close-up view of the near-field microscope (1), the difference frequency generation stage for multi-THz generation (3) and the detection of the scattered waveforms by electro-optic sampling (4). **d**, Close-up view of the multi-arm erbium-doped fiber laser system (2, blue boxes) and the optical setup for custom tailoring the pump and signal pulses for efficient multi-THz generation (5) by difference frequency mixing.

Appendix E

Publications

Publications in peer-reviewed journals

- D. Ehberger, J. Hammer, M. Eisele, M. Krüger, J. Noe, A. Högele, and P. Hommelhoff, *Highly coherent electron beam from a laser-triggered tungsten needle tip*, Physical Review Letters **114**, 227601 (2015).
- M. Eisele, T. L. Cocker, M. A. Huber, M. Plankl, L. Viti, D. Ercolani, L. Sorba, M. S. Vitiello, and R. Huber, *Ultrafast multi-terahertz nano-spectroscopy with sub-cycle temporal resolution*, Nature Photonics **8**, 841 (2014).
- O. Schubert, M. Eisele, V. Crozatier, N. Forget, D. Kaplan, and R. Huber, *Rapid-scan acousto-optical delay line with 34 kHz scan rate and 15 as precision*, Optics Letters **38**, 2907 (2013).
- M. Eisele, M. Krüger, M. Schenk, A. Ziegler, and P. Hommelhoff, *Note: Production of sharp gold tips with high surface quality*, Review of Scientific Instruments **82**, 026101 (2011).

Contributions at international conferences

- M. Eisele, T. L. Cocker, M. A. Huber, M. Plankl, L. Viti, D. Ercolani, L. Sorba, M. S. Vitiello, and R. Huber
  Field-resolved multi-terahertz nano-spectroscopy (invited talk)
  Nanotechnology Congress & Expo, Frankfurt, Germany, 11th August 2015.
- T. L. Cocker, M. Eisele, M. A. Huber, M. Plankl, L. Viti, D. Ercolani, L. Sorba, M. S. Vitiello, and R. Huber
  Ultrafast field-resolved multi-THz spectroscopy on the sub-nanoparticle scale (invited talk)
  SPIE Optics and Photonics 2015, San Diego, USA, 9th August 2015.
- T. L. Cocker, M. Eisele, M. A. Huber, M. Plankl, L. Viti, D. Ercolani, L. Sorba, M. S. Vitiello, and R. Huber
  Ultrafast infrared nanoscopy with sub-cycle temporal resolution (invited talk)
  M&M 2015 (Microscopy and Microanalysis), Portland, USA, 2nd August 2015.
- M. Eisele, T. L. Cocker, M. A. Huber, M. Plankl, L. Viti, D. Ercolani, L. Sorba, M. S. Vitiello, and R. Huber
  Field-resolved multi-terahertz nano-spectroscopy (invited talk)
  Optical Polarisation Conversion in the Near Field, Exeter, UK, 25th June 2015.
- M. A. Huber, M. Eisele, T. L. Cocker, M. Plankl, L. Viti, D. Ercolani, L. Sorba, M. S. Vitiello, and R. Huber
  Ultrafast field-resolved multi-terahertz nano-spectroscopy (contributed talk)
  CLEO/Europe 2015 (Conference on Lasers and Electro-Optics/Europe), Munich, Germany, 21th June 2015.
- T. L. Cocker, M. Eisele, M. A. Huber, M. Plankl, L. Viti, D. Ercolani, L. Sorba, M. S. Vitiello, and R. Huber
  Pump-probe multi-terahertz nano-spectroscopy with sub-cycle temporal resolution (invited talk)
  OTST 2015 (Optical Terahertz Science and Technology), San Diego, USA, 8th March 2015.
- M. Eisele, T. L. Cocker, M. A. Huber, M. Plankl, L. Viti, D. Ercolani, L. Sorba, M. S. Vitiello, and R. Huber
  Field-resolved multi-THz nano-spectroscopy with sub-cycle temporal resolution (contributed talk)
  NanoMeta 2015 (Nanophotonics and Metamaterials), Seefeld, Austria, 5th January 2015.

- M. Eisele, T. L. Cocker, O. Schubert, M. Hohenleutner, F. Langer, S. Baierl, M. Porer, U. Leierseder, M. A. Huber, C. Pöllmann, T. Maag, C. Lange, and R. Huber
  New frontiers of sub-cycle THz optics: the fast, the strong and the small (invited talk)
  TeraNano V 2014 (Terahertz Nanoscience), Martinique, France, 1st December 2014.
- M. Eisele, T. L. Cocker, M. A. Huber, L. Viti, L. Sorba, M. S. Vitiello, and R. Huber
  Ultrafast multi-terahertz nanoscopy with sub-cycle temporal resolution (contributed talk)
  CLEO 2014 (Conference on Lasers and Electro-Optics), San Jose, USA, 8th June 2014.
- T. L. Cocker, M. Eisele, M. A. Huber, L. Viti, D. Ercolani, L. Sorba, M. Plankl, M. S. Vitiello, and R. Huber
  Ultrafast terahertz microscopy with sub-cycle temporal resolution (contributed talk)
  TST 2014 (Terahertz Science and Technology), Camogli, Italy, 11th May 2014.

Bibliography

[Abb73] E. K. Abbe, *Beiträge zur Theorie des Mikroskops und der mikroskopischen Wahrnehmung*, Archiv für mikroskopische Anatomie **9**, 413 (1873).

[Adl07] F. Adler, A. Sell, F. Sotier, R. Huber, and A. Leitenstorfer, *Attosecond relative timing jitter and 13 fs tunable pulses from a two-branch Er:fiber laser*, Optics Letters **32**, 3504 (2007).

[Agr07] G. P. Agrawal, *Nonlinear fiber optics*, Academic Press, San Diego (2007).

[Aiz08] J. Aizpurua, T. Taubner, F. J. García de Abajo, M. Brehm, and R. Hillenbrand, *Substrate-enhanced infrared near-field spectroscopy*, Optics Express **16**, 1529 (2008).

[Ame13] I. Amenabar, S. Poly, W. Nuansing, E. H. Hubrich, A. A. Govyadinov, F. Huth, R. Krutokhvostov, L. Zhang, M. Knez, J. Heberle, A. M. Bittner, and R. Hillenbrand, *Structural analysis and mapping of individual protein complexes by infrared nanospectroscopy*, Nature Communications **4**, 2890 (2013).

[Arb97] M. A. Arbore, M. M. Fejer, M. E. Fermann, A. Hariharan, A. Galvanauskas, and D. Harter, *Frequency doubling of femtosecond erbium-fiber soliton lasers in periodically poled lithium niobate*, Optics Letters **22**, 13 (1997).

[Bal02] A. Baltuška, T. Fuji, and T. Kobayashi, *Controlling the carrier-envelope phase of ultrashort light pulses with optical parametric amplifiers*, Physical Review Letters **88**, 133901 (2002).

[Bas11] D. N. Basov, R. D. Averitt, D. van der Marel, M. Dressel, and K. Haule, *Electrodynamics of correlated electron materials*, Reviews of Modern Physics **83**, 471 (2011).

[Bec94] M. F. Becker, A. B. Buckman, R. M. Walser, T. Lépine, P. Georges, and A. Brun, *Femtosecond laser excitation of the semiconductor-metal phase transition in VO_2*, Applied Physics Letters **65**, 1507 (1994).

[Ber69] C. N. Berglund and H. J. Guggenheim, *Electronic properties of VO_2 near the semiconductor-metal transition*, Physical Review **185**, 1022 (1969).

[Bet91] E. Betzig, J. K. Trautman, T. D. Harris, J. S. Weiner, and R. L. Kostelak, *Breaking the diffraction barrier: optical microscopy on a nanometric scale*, Science **251**, 1468 (1991).

[Bie05] S. Biermann, A. Poteryaev, A. I. Lichtenstein, and A. Georges, *Dynamical singlets and correlation-assisted peierls transition in VO_2*, Physical Review Letters **94**, 026404 (2005).

[Bin83] G. Binnig and H. Rohrer, *Scanning tunneling microscopy*, Surface Science **126**, 236 (1983).

[Bin86] G. Binnig, C. F. Quate, and C. Gerber, *Atomic force microscope*, Physical Review Letters **56**, 930 (1986).

[Bir87] J. R. Birch, *Dispersive Fourier transform spectroscopy*, Mikrochimica Acta **3**, 105 (1987).

[Bon95] A. Bonvalet, M. Joffre, J. L. Martin, and A. Migus, *Generation of ultrabroadband femtosecond pulses in the mid-infrared by optical rectification of 15 fs light pulses at 100 MHz repetition rate*, Applied Physics Letters **67**, 2907 (1995).

[Bon10] F. Bonaccorso, Z. Sun, T. Hasan, and A. C. Ferrari, *Graphene photonics and optoelectronics*, Nature Photonics **4**, 611 (2010).

[Boy08] R. W. Boyd, *Nonlinear optics*, Academic Press, San Diego, third edition (2008).

[Bri10] D. Brida, C. Manzoni, G. Cirmi, M. Marangoni, S. Bonora, P. Villoresi, S. de Silvestri, and G. Cerullo, *Few-optical-cycle pulses tunable from the visible to the mid-infrared by optical parametric amplifiers*, Journal of Optics **12**, 013001 (2010).

[Bri14] D. Brida, G. Krauss, A. Sell, and A. Leitenstorfer, *Ultrabroadband Er:fiber lasers*, Laser Photonics Reviews **8**, 409 (2014).

[Cal15] B. T. O'Callahan, A. C. Jones, J. Hyung Park, D. H. Cobden, J. M. Atkin, and M. B. Raschke, *Inhomogeneity of the ultrafast insulator-to-metal transition dynamics of VO_2*, Nature Communications **6**, 6849 (2015).

[Can98] L. Canali, J. W. G. Wildöer, O. Kerkhof, and L. P. Kouwenhoven, *Low temperature STM on InAs (110) accumulation surfaces*, Applied Physics A **66**, 113 (1998).

[Cao09] J. Cao, E. Ertekin, V. Srinivasan, W. Fan, S. Huang, H. Zheng, J. W. L. Yim, D. R. Khanal, D. F. Ogletree, J. C. Grossman, and J. Wu, *Strain engineering and one-dimensional organization of metal-insulator domains in single-crystal vanadium dioxide beams*, Nature Nanotechnology **4**, 732 (2009).

[Cav01] A. Cavalleri, C. Tóth, C. W. Siders, J. A. Squier, F. Ráksi, P. Forget, and J. C. Kieffer, *Femtosecond structural dynamics in VO_2 during an ultrafast solid-solid phase transition*, Physical Review Letters **87**, 237401 (2001).

[Cav04] A. Cavalleri, T. Dekorsy, H. H. W. Chong, J. C. Kieffer, and R. W. Schoenlein, *Evidence for a structurally-driven insulator-to-metal transition in VO_2: a view from the ultrafast timescale*, Physical Review B **70**, 161102 (2004).

[Che03] H.-T. Chen, R. Kersting, and G. C. Cho, *Terahertz imaging with nanometer resolution*, Applied Physics Letters **83**, 3009 (2003).

[Che04] H.-T. Chen, S. Kraatz, G. C. Cho, and R. Kersting, *Identification of a resonant imaging process in apertureless near-field microscopy*, Physical Review Letters **93**, 267401 (2004).

[Che12] J. Chen, M. Badioli, P. Alonso-González, S. Thongrattanasiri, F. Huth, J. Osmond, M. Spasenović, A. Centeno, A. Pesquera, P. Godignon, A. Z. Elorza, N. Camara, F. J. García de Abajo, R. Hillenbrand, and F. H. L. Koppens, *Optical nano-imaging of gate-tunable graphene plasmons*, Nature **487**, 77 (2012).

[Che14] A. Chernikov, T. C. Berkelbach, H. M. Hill, A. Rigosi, Y. Li, O. Burak Aslan, D. R. Reichman, M. S. Hybertsen, and T. F. Heinz, *Exciton binding energy and nonhydrogenic Rydberg series in monolayer WS_2*, Physical Review Letters **113**, 076802 (2014).

[Coc12] T. L. Cocker, L. V. Titova, S. Fourmaux, G. Holloway, H.-C. Bandulet, D. Brassard, J.-C. Kieffer, M. A. El Khakani, and F. A. Hegmann, *Phase diagram of the ultrafast photoinduced insulator-metal transition in vanadium dioxide*, Physical Review B **85**, 155120 (2012).

[Coc13] T. L. Cocker, V. Jelic, M. Gupta, S. J. Molesky, J. A. J. Burgess, G. de los Reyes, L. V. Titova, Y. Y. Tsui, M. R. Freeman, and F. A. Hegmann, *An ultrafast terahertz scanning tunnelling microscope*, Nature Photonics **7**, 620 (2013).

[Cvi07] A. Cvitkovic, N. Ocelic, and R. Hillenbrand, *Analytical model for quantitative prediction of material contrasts in scattering-type near-field optical microscopy*, Optics Express **15**, 8550 (2007).

[Dai14] S. Dai, Z. Fei, Q. Ma, A. S. Rodin, M. Wagner, A. S. McLeod, M. K. Liu, W. Gannett, W. Regan, K. Watanabe, T. Taniguchi, M. Thiemens, G. Dominguez, A. H. Castro Neto, A. Zettl, F. Keilmann, P. Jarillo-Herrero, M. M. Fogler, and D. N. Basov, *Tunable phonon polaritons in atomically thin van der Waals crystals of boron nitride*, Science **343**, 1125 (2014).

[Dai15] S. Dai, Q. Ma, T. Andersen, A. S. Mcleod, Z. Fei, M. K. Liu, M. Wagner, K. Watanabe, T. Taniguchi, M. Thiemens, F. Keilmann, P. Jarillo-Herrero, M. M. Fogler, and D. N. Basov, *Subdiffractional focusing and guiding of polaritonic rays in a natural hyperbolic material*, Nature Communications **6**, 6963 (2015).

[Dek93] T. Dekorsy, T. Pfeifer, W. Kütt, and H. Kurz, *Subpicosecond carrier transport in GaAs surface-space-charge fields*, Physical Review B **47**, 3842 (1993).

[Doc14] C. J. Docherty, P. Parkinson, H. J. Joyce, M.-H. Chiu, C.-H. Chen, M.-Y. Lee, L.-J. Li, L. M. Herz, and M. B. Johnston, *Ultrafast transient terahertz conductivity of monolayer MoS_2 and WSe_2 grown by chemical vapor deposition*, ACS Nano **8**, 11147 (2014).

[Dre02] M. Dressel and G. Grüner, *Electrodynamics of solids: optical properties of electrons in matter*, Cambridge University Press, Cambridge (2002).

[Eis14] M. Eisele, T. L. Cocker, M. A. Huber, M. Plankl, L. Viti, D. Ercolani, L. Sorba, M. S. Vitiello, and R. Huber, *Ultrafast multi-terahertz nano-spectroscopy with sub-cycle temporal resolution*, Nature Photonics **8**, 841 (2014).

[Eng13] A. P. Engelhardt, B. Hauer, and T. Taubner, *Visibility of weak contrasts in subsurface scattering near-field microscopy*, Ultramicroscopy **126**, 40 (2013).

[Ern07] C. Erny, K. Moutzouris, J. Biegert, D. Kühlke, F. Adler, A. Leitenstorfer, and U. Keller, *Mid-infrared difference-frequency generation of ultrashort pulses tunable between 3.2 and 4.8 μm from a compact fiber source*, Optics Letters **32**, 1138 (2007).

[Eye02] V. Eyert, *The metal-insulator transitions of VO_2: a band theoretical approach*, Annalen der Physik (Leipzig) **11**, 650 (2002).

[Fei85] A. Feisst and P. Koidl, *Current induced periodic ferroelectric domain structures in $LiNbO_3$ applied for efficient nonlinear optical frequency mixing*, Applied Physics Letters **47**, 1125 (1985).

[Fei11] Z. Fei, G. O. Andreev, W. Bao, L. M. Zhang, A. S. Mcleod, C. Wang, M. K. Stewart, Z. Zhao, G. Dominguez, M. Thiemens, M. M. Fogler, M. J. Tauber, A. H. Castro-Neto, C. N. Lau, F. Keilmann, and D. N. Basov, *Infrared nanoscopy of Dirac plasmons at the graphene-SiO_2 interface*, Nano Letters **11**, 4701 (2011).

[Fei12] Z. Fei, A. S. Rodin, G. O. Andreev, W. Bao, A. S. McLeod, M. Wagner, L. M. Zhang, Z. Zhao, M. Thiemens, G. Dominguez, M. M. Fogler, A. H. Castro Neto, C. N. Lau, F. Keilmann, and D. N. Basov, *Gate-tuning of graphene plasmons revealed by infrared nano-imaging*, Nature **487**, 82 (2012).

[Fei13] Z. Fei, A. S. Rodin, W. Gannett, S. Dai, W. Regan, M. Wagner, M. K. Liu, A. S. McLeod, G. Dominguez, M. Thiemens, A. H. Castro Neto, F. Keilmann, A. Zettl, R. Hillenbrand, M. M. Fogler, and D. N. Basov, *Electronic and plasmonic phenomena at graphene grain boundaries*, Nature Nanotechnology **8**, 821 (2013).

[Fer02] B. Ferguson and X.-C. Zhang, *Materials for terahertz science and technology*, Nature Materials **1**, 26 (2002).

[Fre09] A. Frenzel, M. M. Qazilbash, M. Brehm, B.-G. Chae, B.-J. Kim, H.-T. Kim, A. V. Balatsky, F. Keilmann, and D. N. Basov, *Inhomogeneous electronic state near the insulator-to-metal transition in the correlated oxide VO_2*, Physical Review B **80**, 115115 (2009).

[Gal99] G. Gallot and D. Grischkowsky, *Electro-optic detection of terahertz radiation*, Journal of the Optical Society of America B **16**, 1204 (1999).

[Gam08] A. Gambetta, R. Ramponi, and M. Marangoni, *Mid-infrared optical combs from a compact amplified Er-doped fiber oscillator*, Optics Letters **33**, 2671 (2008).

[Gam13] A. Gambetta, N. Coluccelli, M. Cassinerio, D. Gatti, P. Laporta, G. Galzerano, and M. Marangoni, *Milliwatt-level frequency combs in the 8-14 μm range via difference frequency generation from an Er:fiber oscillator*, Optics Letters **38**, 1155 (2013).

[Gei07] A. K. Geim and K. S. Novoselov, *The rise of graphene*, Nature Materials **6**, 183 (2007).

[Gei13] A. K. Geim and I. V. Grigorieva, *Van der Waals heterostructures*, Nature **499**, 419 (2013).

[Gen75] L. Genzel, *Fourier-Transform-Spektroskopie im Infraroten*, Zeitschrift für analytische Chemie **273**, 391 (1975).

[Ger14] J. A. Gerber, S. Berweger, B. T. O'Callahan, and M. B. Raschke, *Phase-resolved surface plasmon interferometry of graphene*, Physical Review Letters **113**, 055502 (2014).

[Goo71] J. B. Goodenough, *The two components of the crystallographic transition in VO_2*, Journal of Solid State Chemistry **3**, 490 (1971).

[Gov13] A. A. Govyadinov, I. Amenabar, F. Huth, P. S. Carney, and R. Hillenbrand, *Quantitative measurement of local infrared absorption and dielectric function with tip-enhanced near-field microscopy*, The Journal of Physical Chemistry Letters **4**, 1526 (2013).

[Gov14] A. A. Govyadinov, S. Mastel, F. Golmar, A. Chuvilin, P. S. Carney, and R. Hillenbrand, *Recovery of permittivity and depth from near-field data as a step toward infrared nanotomography*, ACS Nano **8**, 6911 (2014).

[Grü88] G. Grüner, *The dynamics of charge-density waves*, Reviews of Modern Physics **60**, 1129 (1988).

[Gri12] A. N. Grigorenko, M. Polini, and K. S. Novoselov, *Graphene plasmonics*, Nature Photonics **6**, 749 (2012).

[Hal12] E. Halpern, G. Elias, A. V. Kretinin, H. Shtrikman, and Y. Rosenwaks, *Direct measurement of surface states density and energy distribution in individual InAs nanowires*, Applied Physics Letters **100**, 262105 (2012).

[Hil07] D. J. Hilton, R. P. Prasankumar, S. Fourmaux, A. Cavalleri, D. Brassard, M. A. El Khakani, J. C. Kieffer, A. J. Taylor, and R. D. Averitt, *Enhanced photosusceptibility near T_c for the light-induced insulator-to-metal phase transition in vanadium dioxide*, Physical Review Letters **99**, 226401 (2007).

[Hua12] Q. Hua Wang, K. Kalantar-Zadeh, A. Kis, J. N. Coleman, and M. S. Strano, *Electronics and optoelectronics of two-dimensional transition metal dichalcogenides*, Nature Nanotechnology **7**, 699 (2012).

[Hub00] R. Huber, A. Brodschelm, F. Tauser, and A. Leitenstorfer, *Generation and field-resolved detection of femtosecond electromagnetic pulses tunable up to 41 THz*, Applied Physics Letters **76**, 3191 (2000).

[Hub01] R. Huber, F. Tauser, A. Brodschelm, M. Bichler, G. Abstreiter, and A. Leitenstorfer, *How many-particle interactions develop after ultrafast excitation of an electron-hole plasma*, Nature **414**, 286 (2001).

[Hub08] A. J. Huber, F. Keilmann, J. Wittborn, J. Aizpurua, and R. Hillenbrand, *Terahertz near-field nanoscopy of mobile carriers in single semiconductor nanodevices*, Nano Letters **8**, 3766 (2008).

[Hun98] S. Hunsche, M. Koch, I. Brener, and M. C. Nuss, *THz near-field imaging*, Optics Communications **150**, 22 (1998).

[Hut11] F. Huth, M. Schnell, J. Wittborn, N. Ocelic, and R. Hillenbrand, *Infrared-spectroscopic nanoimaging with a thermal source*, Nature Materials **10**, 352 (2011).

[Hut13] F. Huth, A. Chuvilin, M. Schnell, I. Amenabar, R. Krutokhvostov, S. Lopatin, and R. Hillenbrand, *Resonant antenna probes for tip-enhanced infrared near-field microscopy*, Nano Letters **13**, 1065 (2013).

[Ino94] Y. Inouye and S. Kawata, *Near-field scanning optical microscope with a metallic probe tip*, Optics Letters **19**, 159 (1994).

[Jac12] R. Jacob, S. Winnerl, M. Fehrenbacher, J. Bhattacharyya, H. Schneider, M. T. Wenzel, H.-G. von Ribbeck, L. M. Eng, P. Atkinson, O. G. Schmidt, and M. Helm, *Intersublevel spectroscopy on single InAs-quantum dots by terahertz near-field microscopy*, Nano Letters **12**, 4336 (2012).

[Jep01] P. U. Jepsen, W. Schairer, I. H. Libon, U. Lemmer, N. E. Hecker, M. Birkholz, K. Lips, and M. Schall, *Ultrafast carrier trapping in microcrystalline silicon observed in optical pump-terahertz probe measurements*, Applied Physics Letters **79**, 1291 (2001).

[Jep06] P. U. Jepsen, B. M. Fischer, A. Thoman, H. Helm, J. Y. Suh, R. Lopez, and R. F. Haglund, *Metal-insulator phase transition in a VO_2 thin film observed with terahertz spectroscopy*, Physical Review B **74**, 205103 (2006).

[Jep10] P. U. Jepsen, D. G. Cooke, and M. Koch, *Terahertz spectroscopy and imaging - Modern techniques and applications*, Laser and Photonics Reviews **5**, 124 (2010).

[Jon10] A. C. Jones, S. Berweger, J. Wei, D. Cobden, and M. B. Raschke, *Nano-optical investigations of the metal-insulator phase behavior of individual VO_2 microcrystals*, Nano Letters **10**, 1574 (2010).

[Joy13] H. J. Joyce, C. J. Docherty, Q. Gao, H. H. Tan, C. Jagadish, J. Lloyd-Hughes, L. M. Herz, and M. B. Johnston, *Electronic properties of GaAs, InAs and InP nanowires studied by terahertz spectroscopy*, Nanotechnology **24**, 214006 (2013).

[Kai99] R. A. Kaindl, F. Eickemeyer, M. Woerner, and T. Elsaesser, *Broadband phase-matched difference frequency mixing of femtosecond pulses in GaSe: experiment and theory*, Applied Physics Letters **75**, 1060 (1999).

[Kam11] T. Kampfrath, A. Sell, G. Klatt, A. Pashkin, S. Mährlein, T. Dekorsy, M. Wolf, M. Fiebig, A. Leitenstorfer, and R. Huber, *Coherent terahertz control of antiferromagnetic spin waves*, Nature Photonics **5**, 31 (2011).

[Kam13] T. Kampfrath, K. Tanaka, and K. A. Nelson, *Resonant and nonresonant control over matter and light by intense terahertz transients*, Nature Photonics **7**, 680 (2013).

[Kan00] M. J. Kane, G. Braithwaite, M. T. Emeny, D. Lee, T. Martin, and D. R. Wright, *Bulk and surface recombination in InAs/AlAs$_{0.16}$Sb$_{0.84}$ 3.45 μm light emitting diodes*, Applied Physics Letters **76**, 943 (2000).

[Kaw95] S. Kawata and Y. Inouye, *Scanning probe optical microscopy using a metallic probe tip*, Ultramicroscopy **57**, 313 (1995).

[Kei04] F. Keilmann and R. Hillenbrand, *Near-field microscopy by elastic light scattering from a tip*, Philosophical Transactions of the Royal Society A **362**, 787 (2004).

[Kei12] F. Keilmann and S. Amarie, *Mid-infrared frequency comb spanning an octave based on an Er:fiber laser and difference-frequency generation*, Journal of Infrared, Millimeter and Terahertz Waves **33**, 479 (2012).

[Kin99] J. T. Kindt and C. A. Schmuttenmaer, *Theory for determination of the low-frequency time-dependent response function in liquids using time-resolved terahertz pulse spectroscopy*, Journal of Chemical Physics **110**, 8589 (1999).

[Kno99] B. Knoll and F. Keilmann, *Near-field probing of vibrational absorption for chemical microscopy*, Nature **399**, 134 (1999).

[Kno00] B. Knoll and F. Keilmann, *Enhanced dielectric contrast in scattering-type scanning near-field optical microscopy*, Optics Communications **182**, 321 (2000).

[Koe06] T. C. Koethe, Z. Hu, M. W. Haverkort, C. Schüßler-Langeheine, F. Venturini, N. B. Brookes, O. Tjernberg, W. Reichelt, H. H. Hsieh, H.-J. Lin, C. T. Chen, and L. H. Tjeng, *Transfer of spectral weight and symmetry across the metal-insulator transition in VO_2*, Physical Review Letters **97**, 116402 (2006).

[Kop11] F. H. L. Koppens, D. E. Chang, and F. J. García de Abajo, *Graphene plasmonics: a platform for strong light-matter interactions*, Nano Letters **11**, 3370 (2011).

[Kra10] G. Krauss, S. Lohss, T. Hanke, A. Sell, S. Eggert, R. Huber, and A. Leitenstorfer, *Synthesis of a single cycle of light with compact erbium-doped fibre technology*, Nature Photonics **4**, 33 (2010).

[Kra11] G. Krauss, D. Fehrenbacher, D. Brida, C. Riek, A. Sell, R. Huber, and A. Leitenstorfer, *All-passive phase locking of a compact Er:fiber laser system*, Optics Letters **36**, 540 (2011).

[Kra14] F. Krausz and M. I. Stockman, *Attosecond metrology: from electron capture to future signal processing*, Nature Photonics **8**, 205 (2014).

[Kru12] R. Krutokhvostov, A. A. Govyadinov, J. M. Stiegler, F. Huth, A. Chuvilin, P. S. Carney, and R. Hillenbrand, *Enhanced resolution in subsurface near-field optical microscopy*, Optics Express **20**, 593 (2012).

[Küb04] C. Kübler, R. Huber, S. Tübel, and A. Leitenstorfer, *Ultrabroadband detection of multi-terahertz field transients with GaSe electro-optic sensors: approaching the near infrared*, Applied Physics Letters **85**, 3360 (2004).

[Küb07] C. Kübler, H. Ehrke, R. Huber, R. Lopez, A. Halabica, R. F. Haglund, and A. Leitenstorfer, *Coherent structural dynamics and electronic correlations during an ultrafast insulator-to-metal phase transition in VO_2*, Physical Review Letters **99**, 116401 (2007).

[Lab00] M. Labardi, S. Patanè, and M. Allegrini, *Artifact-free near-field optical imaging by apertureless microscopy*, Applied Physics Letters **77**, 621 (2000).

[Liu04] K. Liu, J. Xu, and X.-C. Zhang, *GaSe crystals for broadband terahertz wave detection*, Applied Physics Letters **85**, 863 (2004).

[Liu13] M. K. Liu, M. Wagner, E. Abreu, S. Kittiwatanakul, A. McLeod, Z. Fei, M. Goldflam, S. Dai, M. M. Fogler, J. Lu, S. A. Wolf, R. D. Averitt, and D. N. Basov, *Anisotropic electronic state via spontaneous phase separation in strained vanadium dioxide films*, Physical Review Letters **111**, 096602 (2013).

[Liu14] M. K. Liu, M. Wagner, J. Zhang, A. McLeod, S. Kittiwatanakul, Z. Fei, E. Abreu, M. Goldflam, A. J. Sternbach, S. Dai, K. G. West, J. Lu, S. A. Wolf, R. D. Averitt, and D. N. Basov, *Symmetry breaking and geometric confinement in VO_2: results from a three-dimensional infrared nano-imaging*, Applied Physics Letters **104**, 121905 (2014).

[Mad04] O. Madelung, *Semiconductors: data handbook*, Springer, Berlin Heidelberg (2004).

[Mai60] T. H. Maiman, *Stimulated optical radiation in ruby*, Nature **187**, 493 (1960).

[May13] B. Mayer, D. Rudolph, J. Schnell, S. Morkötter, J. Winnerl, J. Treu, K. Müller, G. Bracher, G. Abstreiter, G. Koblmüller, and J. J. Finley, *Lasing from individual GaAs-AlGaAs core-shell nanowires up to room temperature*, Nature Communications **4**, 2931 (2013).

[Moo12] K. Moon, Y. Do, M. Lim, G. Lee, H. Kang, K.-S. Park, and H. Han, *Quantitative coherent scattering spectra in apertureless terahertz pulse near-field microscopes*, Applied Physics Letters **101**, 011109 (2012).

[Mor59] F. J. Morin, *Oxides which show a metal-to-insulator transition at the neel temperature*, Physical Review Letters **3**, 34 (1959).

[Mor12] E. Morosan, D. Natelson, A. H. Nevidomskyy, and Q. Si, *Strongly correlated materials*, Advanced Materials **24**, 4896 (2012).

[Nak08] M. Nakajima, N. Takubo, Z. Hiroi, Y. Ueda, and T. Suemoto, *Photoinduced metallic state in VO_2 proved by the terahertz pump-probe spectroscopy*, Applied Physics Letters **92**, 011907 (2008).

[Něm02] H. Němec, F. Kadlec, and P. Kužel, *Methodology of an optical pump-terahertz probe experiment: an analytical frequency-domain approach*, Journal of Chemical Physics **117**, 8454 (2002).

[Něm05] H. Němec, F. Kadlec, C. Kadlec, P. Kužel, and P. Jungwirth, *Ultrafast far-infrared dynamics probed by terahertz pulses: a frequency-domain approach. II. Applications*, The Journal of Chemical Physics **122**, 104504 (2005).

[Nog91] M. Noguchi, K. Hirakawa, and T. Ikoma, *Intrinsic electron accumulation layers on reconstructed clean InAs(100) surfaces*, Physical Review Letters **66**, 2243 (1991).

[Nov98] L. Novotny, E. J. Sánchez, and X. S. Xie, *Near-field optical imaging using metal tips illuminated by higher-order Hermite-Gaussian beams*, Ultramicroscopy **71**, 21 (1998).

[Nov04] K. S. Novoselov, A. K. Geim, S. V. Morozov, D. Jiang, Y. Zhang, S. V. Dubonos, I. V. Grigorieva, and A. A. Firsov, *Electric field effect in atomically thin carbon films*, Science **306**, 666 (2004).

[Nov12] K. S. Novoselov, V. I. Fal'ko, L. Colombo, P. R. Gellert, M. G. Schwab, and K. Kim, *A roadmap for graphene*, Nature **490**, 192 (2012).

[Onn11] H. K. Onnes, *The resistance of pure mercury at helium temperatures*, Communications from the Physical Laboratory at the University of Leiden **12**, 120 (1911).

[Par07] P. Parkinson, J. Lloyd-Hughes, Q. Gao, H. H. Tan, C. Jagadish, M. B. Johnston, and L. M. Herz, *Transient terahertz conductivity of GaAs nanowires*, Nano Letters **7**, 2162 (2007).

[Pas10] A. Pashkin, M. Porer, M. Beyer, K. W. Kim, A. Dubroka, C. Bernhard, X. Yao, Y. Dagan, R. Hackl, A. Erb, J. Demsar, R. Huber, and A. Leitenstorfer, *Femtosecond response of quasiparticles and phonons in superconducting $YBa_2Cu_3O_{7-d}$ studied by wideband terahertz spectroscopy*, Physical Review Letters **105**, 067001 (2010).

[Pas11] A. Pashkin, C. Kübler, H. Ehrke, R. Lopez, A. Halabica, R. F. Haglund, R. Huber, and A. Leitenstorfer, *Ultrafast insulator-metal phase transition in VO_2 studied by multiterahertz spectroscopy*, Physical Review B **83**, 195120 (2011).

[Pet01] V. Petrov, F. Rotermund, and F. Noack, *Generation of high-power femtosecond light pulses at 1 kHz in the mid-infrared spectral range between 3 and 12 μm by second-order nonlinear processes in optical crystals*, Journal of Optics A: Pure and Applied Optics **3**, R1 (2001).

[Pip06] L. F. J. Piper, T. D. Veal, M. J. Lowe, and C. F. McConville, *Electron depletion at InAs free surfaces: doping-induced acceptorlike gap states*, Physical Review B **73**, 195321 (2006).

[Poh84] D. W. Pohl, W. Denk, and M. Lanz, *Optical stethoscopy: image recording with resolution λ/20*, Applied Physics Letters **44**, 651 (1984).

[Por14a] M. Porer, U. Leierseder, J.-M. Ménard, H. Dachraoui, L. Mouchliadis, I. E. Perakis, U. Heinzmann, J. Demsar, K. Rossnagel, and R. Huber, *Non-thermal separation of electronic and structural orders in a persisting charge density wave*, Nature Materials **13**, 857 (2014).

[Por14b] M. Porer, J.-M. Ménard, and R. Huber, *Shot noise reduced terahertz detection via spectrally postfiltered electro-optic sampling*, Optics Letters **39**, 2435 (2014).

[Qaz07] M. M. Qazilbash, M. Brehm, B.-G. Chae, P.-C. Ho, G. O. Andreev, B.-J. Kim, S. J. Yun, A. V. Balatsky, M. B. Maple, F. Keilmann, H.-T. Kim, and D. N. Basov, *Mott transition in VO_2 revealed by infrared spectroscopy and nano-imaging*, Science **318**, 1750 (2007).

[Qaz11] M. M. Qazilbash, A. Tripathi, A. A. Schafgans, B.-J. Kim, H.-T. Kim, Z. Cai, M. V. Holt, J. M. Maser, F. Keilmann, O. G. Shpyrko, and D. N. Basov, *Nanoscale imaging of the electronic and structural transitions in vanadium dioxide*, Physical Review B **83**, 165108 (2011).

[Rak98] A. D. Rakić, A. B. Djurišić, J. M. Elazar, and M. L. Majewski, *Optical properties of metallic films for vertical-cavity optoelectronic devices*, Applied Optics **37**, 5271 (1998).

[Ras03] M. B. Raschke and C. Lienau, *Apertureless near-field optical microscopy: tip–sample coupling in elastic light scattering*, Applied Physics Letters **83**, 5089 (2003).

[Ren05] J. Renger, S. Grafström, L. M. Eng, and R. Hillenbrand, *Resonant light scattering by near-field-induced phonon polaritons*, Physical Review B **71**, 075410 (2005).

[Rib08] H.-G. von Ribbeck, M. Brehm, D. W. van der Weide, S. Winnerl, O. Drachenko, M. Helm, and F. Keilmann, *Spectroscopic THz near-field microscope*, Optics Express **16**, 3430 (2008).

[Ric94] A. Rice, Y. Jin, X. F. Ma, X.-C. Zhang, D. Bliss, J. Larkin, and M. Alexander, *Terahertz optical rectification from (110) zinc blende crystals*, Applied Physics Letters **64**, 1324 (1994).

[Rot14] N. Rotenberg and L. Kuipers, *Mapping nanoscale light fields*, Nature Photonics **8**, 919 (2014).

[Saï08] I. Saïdi, S. Ben Radhia, and K. Boujdaria, *Band structures of GaAs, InAs, and InP: A 34 kp model*, Journal of Applied Physics **104**, 023706 (2008).

[Sax13] D. Saxena, S. Mokkapati, P. Parkinson, N. Jiang, Q. Gao, H. H. Tan, and C. Jagadish, *Optically pumped room-temperature GaAs nanowire lasers*, Nature Photonics **7**, 963 (2013).

[Sch14] O. Schubert, M. Hohenleutner, F. Langer, B. Urbanek, C. Lange, U. Huttner, D. Golde, T. Meier, M. Kira, S. W. Koch, and R. Huber, *Sub-cycle control of terahertz high-harmonic generation by dynamical Bloch oscillations*, Nature Photonics **8**, 119 (2014).

[Sel08] A. Sell, R. Scheu, A. Leitenstorfer, and R. Huber, *Field-resolved detection of phase-locked infrared transients from a compact Er:fiber system tunable between 55 and 107 THz*, Applied Physics Letters **93**, 251107 (2008).

[Sel09] A. Sell, G. Krauss, R. Scheu, R. Huber, and A. Leitenstorfer, *8-fs pulses from a compact Er:fiber system: quantitative modeling and experimental implementation*, Optics Express **17**, 1070 (2009).

[Sel11] D. V. Seletskiy, M. P. Hasselbeck, J. G. Cederberg, A. Katzenmeyer, M. E. Toimil-Molares, F. Léonard, A. A. Talin, and M. Sheik-Bahae, *Efficient terahertz emission from InAs nanowires*, Physical Review B **84**, 115421 (2011).

[Shi90] S. Shin, S. Suga, M. Taniguchi, M. Fujisawa, H. Kanzaki, A. Fujimori, H. Daimon, Y. Ueda, K. Kosuge, and S. Kachi, *Vacuum-ultraviolet reflectance and photoemission study of the metal-insulator phase transitions in VO_2, V_6O_{13}, and V_2O_3*, Physical Review B **41**, 4993 (1990).

[Sti10] J. M. Stiegler, A. J. Huber, S. L. Diedenhofen, J. Gómez Rivas, R. E. Algra, E. P. A. M. Bakkers, and R. Hillenbrand, *Nanoscale free-carrier profiling of individual semiconductor nanowires by infrared near-field nanoscopy*, Nano Letters **10**, 1387 (2010).

[Sto89] R. H. Stolen, J. P. Gordon, W. J. Tomlinson, and H. A. Haus, *Raman response function of silica-core fibers*, Journal of the Optical Society of America B **6**, 1159 (1989).

[Syn28] E. H. Synge, *A suggested method for extending microscopic resolution into the ultra-microscopic region*, Philosophical Magazine **6**, 356 (1928).

[Tau03a] T. Taubner, R. Hillenbrand, and F. Keilmann, *Performance of visible and mid-infrared scattering-type near-field optical microscopes*, Journal of Microscopy **210**, 311 (2003).

[Tau03b] F. Tauser, A. Leitenstorfer, and W. Zinth, *Amplified femtosecond pulses from an Er:fiber system: nonlinear pulse shortening and self-referencing detection of the carrier-envelope phase evolution*, Optics Express **11**, 594 (2003).

[Tau04] F. Tauser, F. Adler, and A. Leitenstorfer, *Widely tunable sub-30-fs pulses from a compact erbium-doped fiber source*, Optics Letters **29**, 516 (2004).

[Tau05] T. Taubner, F. Keilmann, and R. Hillenbrand, *Nanoscale-resolved subsurface imaging by scattering-type near-field optical microscopy*, Optics Express **13**, 8893 (2005).

[Ton07] M. Tonouchi, *Cutting-edge terahertz technology*, Nature Photonics **1**, 97 (2007).

[Ulb11] R. Ulbricht, E. Hendry, J. Shan, T. F. Heinz, and M. Bonn, *Carrier dynamics in semiconductors studied with time-resolved terahertz spectroscopy*, Reviews of Modern Physics **83**, 543 (2011).

[Van14] L. R. Vanderhoef, A. K. Azad, C. C. Bomberger, D. R. Chowdhury, D. B. Chase, A. J. Taylor, J. M. O. Zide, and M. F. Doty, *Charge carrier relaxation processes in TbAs nanoinclusions in GaAs measured by optical-pump THz-probe transient absorption spectroscopy*, Physical Review B **89**, 045418 (2014).

[Vee13] M. van Veenendaal, *Ultrafast photoinduced insulator-to-metal transitions in vanadium dioxide*, Physical Review B **87**, 235118 (2013).

[Vit12] M. S. Vitiello, D. Coquillat, L. Viti, D. Ercolani, F. Teppe, A. Pitanti, F. Beltram, L. Sorba, W. Knap, and A. Tredicucci, *Room temperature terahertz detectors based on semiconductor nanowire field effect transistors*, Nano Letters **12**, 96 (2012).

[Vod92] K. L. Vodopyanov, H. Graener, C. C. Phillips, and T. J. Tate, *Picosecond carrier dynamics and studies of Auger recombination processes in indium arsenide at room temperature*, Physical Review B **46**, 13194 (1992).

[Wag14a] M. Wagner, Z. Fei, A. S. McLeod, A. S. Rodin, W. Bao, E. G. Iwinski, Z. Zhao, M. Goldflam, M. Liu, G. Dominguez, M. Thiemens, M. M. Fogler, A. H. Castro Neto, C. Ning Lau, S. Amarie, F. Keilmann, and D. N. Basov, *Ultrafast and nanoscale plasmonic phenomena in exfoliated graphene revealed by infrared pump-probe nanoscopy*, Nano Letters **14**, 894 (2014).

[Wag14b] M. Wagner, A. S. McLeod, S. J. Maddox, Z. Fei, M. Liu, R. D. Averitt, M. M. Fogler, S. R. Bank, F. Keilmann, and D. N. Basov, *Ultrafast dynamics of surface plasmons in InAs by time-resolved infrared nanospectroscopy*, Nano Letters **14**, 4529 (2014).

[Weg14] D. Wegkamp, M. Herzog, L. Xian, M. Gatti, P. Cudazzo, C. L. McGahan, R. E. Marvel, R. F. Haglund, A. Rubio, M. Wolf, and J. Stähler, *Instantaneous band gap collapse in photoexcited monoclinic VO_2 due to photocarrier doping*, Physical Review Letters **113**, 216401 (2014).

[Wen94] R. M. Wentzcovitch, W. W. Schulz, and P. B. Allen, *VO_2: Peierls or Mott-Hubbard? A view from band theory*, Physical Review Letters **72**, 3389 (1994).

[Wes14] C. Westermeier, A. Cernescu, S. Amarie, C. Liewald, F. Keilmann, and B. Nickel, *Sub-micron phase coexistence in small-molecule organic thin films revealed by infrared nano-imaging*, Nature Communications **5**, 4101 (2014).

[Wim14] L. Wimmer, G. Herink, D. R. Solli, S. V. Yalunin, K. E. Echternkamp, and C. Ropers, *Terahertz control of nanotip photoemission*, Nature Physics **10**, 432 (2014).

[Woe15] A. Woessner, M. B. Lundeberg, Y. Gao, A. Principi, P. Alonso-González, M. Carrega, K. Watanabe, T. Taniguchi, G. Vignale, M. Polini, J. Hone, R. Hillenbrand, and F. H. L. Koppens, *Highly confined low-loss plasmons in graphene-boron nitride heterostructures*, Nature Materials **14**, 421 (2015).

[Wu95] Q. Wu and X.-C. Zhang, *Free-space electro-optic sampling of terahertz beams*, Applied Physics Letters **67**, 3523 (1995).

[Wu06] J. Wu, Q. Gu, B. S. Guiton, N. P. de Leon, L. Ouyang, and H. Park, *Strain-induced self organization of metal-insulator domains in single-crystalline VO_2 nanobeams*, Nano Letters **6**, 2313 (2006).

[Xia14] F. Xia, H. Wang, D. Xiao, M. Dubey, and A. Ramasubramaniam, *Two-dimensional material nanophotonics*, Nature Photonics **8**, 899 (2014).

[Yan09] R. Yan, D. Gargas, and P. Yang, *Nanowire Photonics*, Nature Photonics **3**, 569 (2009).

[Yu05] P. Y. Yu and M. Cardona, *Fundamentals of semiconductors*, Springer, Berlin Heidelberg, third edition (2005).

[Zen94] F. Zenhausern, M. P. O'Boyle, and H. K. Wickramasinghe, *Apertureless near-field optical microscope*, Applied Physics Letters **65**, 1623 (1994).

[Zen95] F. Zenhausern, Y. Martin, and H. K. Wickramasinghe, *Scanning interferometric apertureless microscopy: optical imaging at 10 angstrom resolution*, Science **269**, 1083 (1995).

[Zha92] X.-C. Zhang and D. H. Auston, *Optoelectronic measurement of semiconductor surfaces and interfaces with femtosecond optics*, Journal of Applied Physics **71**, 326 (1992).

[Zha07] H. Zhan, V. Astley, M. Hvasta, J. A. Deibel, D. M. Mittleman, and Y.-S. Lim, *The metal-insulator transition in VO_2 studied using terahertz apertureless near-field microscopy*, Applied Physics Letters **91**, 162110 (2007).

[Zim04] M. Zimmermann, C. Gohle, R. Holzwarth, T. Udem, and T. W. Hänsch, *Optical clockwork with an offset-free difference-frequency comb: accuracy of sum- and difference-frequency generation*, Optics Letters **29**, 310 (2004).

[Zyl75] A. Zylbersztejn and N. F. Mott, *Metal-insulator transition in vanadium dioxide*, Physical Review B **11**, 4383 (1975).

Acknowledgments

This work and the wonderful academic and private time in Regensburg would not have been possible without the help and the care of many people. I gratefully acknowledge everyone who has contributed to the success of this work, in particular I would like to thank:

- **Prof. Dr. Rupert Huber** for his believe in my capabilities to develop the world's-first ultrafast, field-resolved near-field microscope, his truly infectious enthusiasm for physics accompanied with many inspiring ideas and the possibility to discuss physical problems of any kind at any time.
- **Dr. Miriam S. Vitiello**, **Dr. Leonardo Viti**, **Dr. Daniele Ercolani** and **Dr. Lucia Sorba** for their collaboration on the experiments performed on the indium arsenide nanowires and for providing the samples.
- **Prof. Dr. Richard Haglund** for providing the vanadium dioxide nanowires and for his collaboration on strongly correlated materials.
- **Dr. Jonathan Eroms** and **Prof. Dr. Dieter Weiss** for providing the graphene samples and for the discussions of the first experimental results.
- **PD Dr. Tobias Korn** and **Prof. Dr. Christian Schüller** for their collaboration on the first tungsten diselenide experiments.
- **Prof. Dr. Jascha Repp** for taking the time to examine this work.
- **Prof. Dr. Vladimir M. Braun** and **Prof. Dr. Christoph Strunk** for assessing this work.
- **Dr. Tyler L. Cocker** for the joint effort to build up the microscope, conducting the ultrafast near-field experiments and for the fun time in the laboratory. Special thanks for proof-reading the entire thesis.

- **Markus Huber** and **Markus Plankl** for their work on the indium arsenide near-field experiments, proof-reading this thesis and for taking over the near-field laboratory.
- **Bernhard Surrer** for his help on performing first multi-THz experiments and for many insightful discussions regarding ultrafast terahertz spectroscopy.
- **Dr. Olaf Schubert** for many interesting and especially fruitful discussions on physical topics.
- **Sebastian Baierl**, **Matthias Hohenleutner**, **Fabian Langer**, **Thomas Maag**, **Christoph Pöllmann** and **Dr. Michael Porer** for their great support during the entire thesis, the proof-reading of this work, the interesting discussions and the numerous leisure activities besides the university.
- **Martin Furthmeier**, **Imke Gronwald** and **Peter Müller** for their great commitment to build up the near-field laboratory and for characterizing and providing nano-structured samples.
- **Ulla Franzke** for her patient support in all administrative tasks.
- **All other** current and former members of the chair of Prof. Huber for their support and the great working atmosphere.
- **My parents**, my sisters **Eva**, **Heidi**, **Lilly** and **Olga** and my brother **Tom** for their loving support during the time in Regensburg, their constant encouragement and their unshakable believe in the success of my work.
- **Hans**, **Maria** and **Lisa** for their wide-open door, their wholehearted support and all the food.
- **Ursula** for making each day so much more beautiful.